Journal of Rock Mechanics and Geotechnical Engineering 15 (2023) 66–101

Contents lists available at ScienceDirect

Journal of Rock Mechanics and Geotechnical Engineering

journal homepage: www.jrmge.cn

Qian Lecture

Geostructures, dynamics and risk mitigation of high-altitude and long-runout rockslides

Yueping Yin [a,b,*], Bin Li [b,c,**], Yang Gao [b,c], Wenpei Wang [a], Shilin Zhang [d], Nan Zhang [a]

[a] China Institute of Geological Environment Monitoring, China Geological Survey, Beijing, 100081, China
[b] Key Laboratory of Active Tectonics and Geological Safety, Ministry of Natural Resources, Beijing, 100081, China
[c] Institute of Geomechanics, Chinese Academy of Geological Sciences, China Geological Survey, Beijing, 100081, China
[d] Department of Geological Engineering, Southwest Jiaotong University, Chengdu, 610031, China

ARTICLE INFO

Article history:
Received 7 November 2022
Received in revised form
12 November 2022
Accepted 14 November 2022
Available online 25 November 2022

Keywords:
Rockslide
High-altitude and long-runout
Sliding-prone geostructure
Large-scale experimental apparatus
Risk mitigation strategy
Structural prevention technique

ABSTRACT

Long-runout rockslides at high altitude could cause disaster chain in river basins and destroy towns and major infrasturctures. This paper firstly explores the initiation mechanism of high-altitude and long-runout rockslides. Two types of sliding-prone geostructure models, i.e. the fault control type in orogenic belt and the fold control type in platform area, are proposed. Then, large-scale experimental apparatus and associated numerical simulations are conducted to understanding the chain-style dynamics of rockslide-debris avalanche-debris flow. The results reveal the fragmentation effects, the rheological behaviors and the boundary layer effect of long-runout avalanche-debris flow. The dynamic characteristics of quasi-static-transition-inertia state and solid-liquid coupling in rapid movement of rockslide-debris avalanche-debris flow are investigated. Finally, the risk mitigation strategy of the non-structure and structure for resilient energy dissipation are illustrated for initiation, transition and deposition zones. The structural prevention and mitigation methods have been successfully applied to the high-altitude and long-runout rockslides in Zhouqu and Maoxian of the Wenchuan earthquake zone, as well as the other major geohazards in Qinghai-Tibet Plateau and its adjacent areas.

1. Introduction

The long-runout rockslide at high altitude is defined, as the large-scale rockslides initiated at high altitude mountains and then transformed into dry/wet debris flow with flow-like characteristics (Yin et al., 2021a). Generally, long-runout rockslides at high altitude are complex geohazards composed of two or more landslide types (Hungr et al., 2014). They have the characteristics of slip initiating at a high altitude, significant dynamic conversion from potential energy to kinetic energy, and thereby is able to induce catastrophic disaster chains. (Yin et al., 2017a). Thus, it is a challenge to understand the rockslide instability mechanism, disaster mode, and risk control of this type of complex geohazard. In particular, the high-altitude initiation mechanism and long-runout dynamics under the effects of strong earthquakes, climate changes, extreme rainfall/snowfall, and mining activities are hot scientific topics (Huang, 2009; Sassa et al., 2010; Yue, 2013; Iverson and Ouyang, 2015; Crosta et al., 2017; Yin et al., 2017b; Shugar et al., 2021).

Long-runout rockslides at high altitude are characterized by a gigantic scale, possibly reaching hundreds of millions of cubic meters. The height differences may reach several kilometers, so enormous kinetic energy would generated and possibly cause a runout distance of over 10 km. Therefore, disaster chains could be formed in the river basin covering hundreds of kilometers. These complex geohazards are challenging as they significantly threaten the major engineering projects such as hydropower facilities, railways, highways, and mountain towns (Cui et al., 2017; Peng et al., 2020; Yin et al., 2021a). For example, the Qinghai-Tibet Plateau and its surroundings are the most severely

* Corresponding author. China Institute of Geological Environment Monitoring, China Geological Survey, Beijing, 100081, China.
** Corresponding author. Key Laboratory of Active Tectonics and Geological Safety, Ministry of Natural Resources, Beijing, 100081, China.
E-mail addresses: yinypcgs@hotmail.com (Y. Yin), libin1102@163.com (B. Li).
Peer review under responsibility of Institute of Rock and Soil Mechanics, Chinese Academy of Sciences.

https://doi.org/10.1016/j.jrmge.2022.11.001

affected areas by the high-altitude and long-runout rockslides. On April 9, 2000, a massive disaster chain of rockslide-debris avalanche-landslide dam occurred in Yigong, Tibet, China, with a height difference of 3330 m and a runout distance of 10,000 m. The Yigong Zangbo River was dammed by a deposit with a volume 3×10^8 m^3, and the subsequent outburst flood hazards affected tens of thousands of people living downstream (Yin, 2000; Yin and Xing, 2012). On October 10 and November 3, 2018, two high-altitude and long-runout rockslides occurred in eastern Tibet, China. The rockslides blocked the mainstream of the Jinsha River twice and caused economic losses of several billion Chinese Yuan (CNY) due to the outburst flood (Xu et al., 2018; Deng et al., 2019; Wang et al., 2020a; Zhang et al., 2020a). On February 7, 2021, a complex rock-ice avalanche occurred at Nanda Devi in Chamoli, Uttarakhand, India. The landslide dam and subsequent outburst flood destroyed two downstream hydropower stations which were under construction, and the estimated deaths exceeded 200 (Shugar et al., 2021; Yin et al., 2021b; Fan et al., 2022; Zhang et al., 2022). Because the long-runout rockslides at high altitude can cause catastrophic events, it is urgent to address the following critical scientific issues.

(1) Sliding-prone geostructure and initiation mechanism

The high-altitude and long-runout rockslides are generally controlled by the tectonic belt or fold zone, and the triggers mainly include earthquakes, heavy rainfall, snow and ice, and mining. It is essential to understand the geological characteristics of the rockslide that occurs and the mechanism for disaster prevention and mitigation.

(2) Dynamics of high-altitude and long-runout disaster chains

The high-altitude and long-runout rockslides usually have a disaster chain of ice/rock slide/avalanche and debris flow, and can lead to the secondary disasters consisting of landslide dams, outburst floods, and secondary landslides. Three issues should be ffocused on: (i) multiscale and multi-media transformation of the geomaterials (i.e. block, granular material, and liquid-solid two-phase flow), (ii) mechanisms of mass changing, momentum transferring, and energy conversing, and (iii) the micro-topography and the effect of the boundary layer in dynamic processes.

(3) Risk assessment and mitigation technology

Advanced identification-monitoring-warning methods, risk avoidance strategies, and disaster prevention and control technologies (especially the rigid and ductile structures when developing energy dissipation technologies) for the high-altitude and long-runout rockslides are urgently needed. It is critical to come up with a new design theory and technical methodology for disaster prevention and control on the basis of the transformation mechanism of the whole disaster chain.

This paper takes the high-altitude and long-runout rockslides in the Qinghai-Tibet Plateau and its surrounding areas as examples to analyze the initiation mechanism, chain-style dynamics, and risk mitigation method. These include: (i) classifying the sliding-prone geostructures in mountains and understanding the failure mechanisms using geological survey, remote sensing analysis, geophysical exploration, and mechanical analysis, (ii) analyzing the dynamic process of the disaster chain by a series of large-scale physical

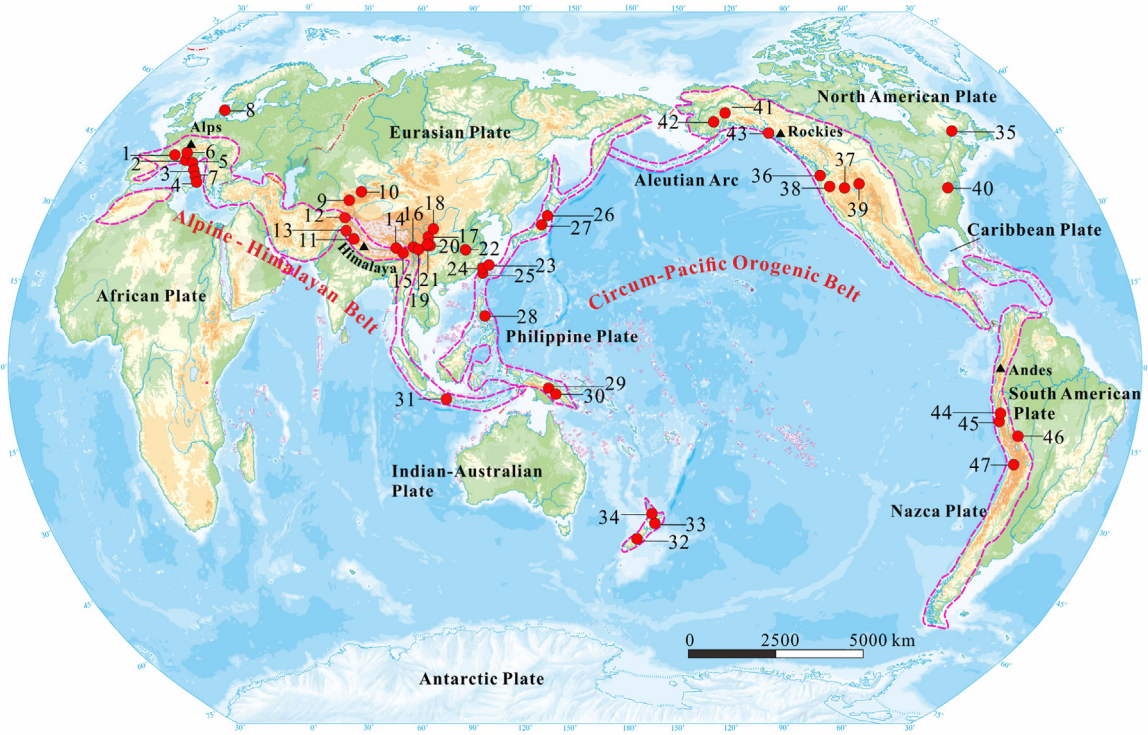

Fig. 1. Global orogenic belts and typical high-altitude and long-runout rockslides (Pink broken line zone refers to as the major orogenic belts. Red dots refer to catastrophic geohazard events: 1-Elm, 2-Randa, 3-Brenva Gl., 4-Vajont, 5-Costantino, 6-Valtellina, 7-Val Pola Rock, 8-Paatuut, 9-Usoi, 10-Khait, 11-Chamoli, 12-Hunza River, 13-Hattian Bala, 14-Yigong, 15-Sedongpu, 16-Baige, 17-Daguangbao, 18-Wenjiagou, 19-Xiejiadianzi, 20-Donghekou, 21-Xinmo, 22-Xintan, 23-Tsao-Ling4, 24-Chiu-Fen-Erh-Shan, 25-Hsiaolin, 26-Mount Ontake, 27-Kuridaira, 28-Leyte, 29-Bairaman, 30-Ok Tedi Mine, 31-Merapi Volcano, 32-Falling Mt., 33-Mangapoike, 34-Mt. Fletcher, 35-Frank, 36-Hope, 37-Mt. Munday, 38-Mount Meager, 39-Gros Ventre, 40-Madison Canyon, 41-Sherman Glacier, 42-Allen, 43- Lituya Bay, 44-Huascarán[1],45-Huascarán[2], 46-Mayunmarca, 47-Glacier Pucajirca).

experiments and a self-developed numerical simulation software, Landslide Post-failure in Three Dimensions (LPF^{3D}), (iii) developing the risk evaluation technologies, and (iv) proposing risk management strategy for practical engineering disaster mitigation.

2. Distribution and classification of the high-altitude and long-runout rockslides

2.1. Distribution of the high-altitude and long-runout rockslides in the world

The global high-altitude and long-runout rockslides are mainly distributed in the Alpine–Himalayan orogenic belt and the mountains of the Circum-Pacific belt (see Fig. 1 and Table 1). These mountain belts are generally characterized by active crustal movements, frequent earthquakes and volcanic eruptions, huge topographic relief, and intensive human activity (Hewitt et al., 2008; Pánek, 2019; Broeckx et al., 2019).

The Alpine–Himalayan orogenic belt, nearly having a length of 10,000 km, stretches across North Africa, Europe, and Asia, and deflects southward over the Tibetan Plateau, in which the Elm rockslide (Heim, 1932), Vajont rockslide (Ibañez and Hatzor, 2018), Yigong rockslide (Yin and Xing, 2012), Chamoli rockslide (Shugar et al., 2021; Yin et al., 2021a; Zhang et al., 2022), and many other catastrophic long-runout rockslides are distributed. Sequent continent merging, ocean closing, and plate collision events happen

Table 1
Typical high-altitude and long-runout rockslides in the world.

No.	Name	Country	Year	Material	Trigger	V (10^6 m^3)	H (m)	L (m)	u (H/L)	Reference
1	Elm	Switzerland	1881	Slate	Mining	10	610	2450	0.25	Heim (1932); Hsü and Voight (1978)
2	Randa	Switzerland	1991	Gneiss	Weather	10	945	1300	0.73	Noverraz and Bonnard (1992)
3	Brenva Gl.	Italy	1920	Ice/Granite	Climate change	10	2640	5621	0.47	Deline (2001,2009)
4	Vajont	Italy	1963	Limestone, Mudstone	Reservoir storage	270	600	1400	0.43	Chowdhury (1987)
5	Costantino	Italy	1973	Gneiss	Rainfall	20	1384	2000	0.69	Cencetti et al. (2017)
6	Valtellina	Italy	1987	Diorite, gneiss	Rainfall	35	1050	2000	0.53	Cambiaghi and Schuster (1989)
7	Val Pola Rock	Italy	1987	Diorite, Gabbro	Rainfall	40	700	2700	0.26	Crosta et al. (2011)
8	Paatuut	Denmark	2000	Shales	Earthquake	90	400	1500	0.27	Pedersen et al. (2002)
9	Usoi	Tajikistan	1911	Dolomite, Limestone	Earthquake	2000	1480	6170	0.24	Alford and Schuster (2000)
10	Khait	Tajikistan	1949	Gneiss	Earthquake	75	1500	11000	0.14	Evans et al. (2009)
11	Chamoli	India	2021	Ice, Gneiss	Climate change	50	2700	15000	0.18	Shugar et al. (2021)
12	Hunza River	Pakistan	2010	Gneiss	Earthquake	45	1060	1700	0.62	Delaney and Evans (2017)
13	Hattian Bala	Pakistan	2005	Mudstone	Earthquake	85	800	2609	0.31	Dunning et al. (2007)
14	Yigong	China	2000	Granite	Earthquake, Snowfall	300	3330	10000	0.33	Yin et al. (2000)
15	Sedongpu	China	2018	Gneiss, Schist, Marble	Earthquake, Snowfall	35	4548	8000	0.57	Liu et al. (2019)
16	Baige	China	2018	Ophiolitic mélange	Creep	31.65	840	1600	0.53	Zhang et al. (2020b)
17	Daguangba	China	2008	Limestone	Earthquake	1159	1502	4500	0.33	Huang et al. (2009)
18	Wenjiagou	China	2008	Limestone	Earthquake	50	1360	4170	0.33	Zhang et al. (2016)
19	Xiejiadianzi	China	2008	Granite, Sandstone	Earthquake	4	800	1800	0.44	Dai et al. (2011)
20	Donghekou	China	2008	Carbonaceous slate	Earthquake	20	700	2387	0.29	Yin et al. (2009)
21	Xinmo	China	2017	Metamorphic quartz sandstone, slate	Earthquake, Snowfall	16.37	1120	2500	0.45	Yin et al. (2017b)
22	Xintan	China	1985	Limestone, Sandstone	Rainfall	30	700	2000	0.35	Liu (1988)
23	Tsao-Ling4	Taiwan, China	1942	Sandstone, Shale	Earthquake, Rainfall	1	600	2300	0.26	Yang et al. (2004)
24	Chiu-Fen-Erh-Shan	Taiwan, China	1999	Sandstone, Shale	Earthquake	0.5	550	2000	0.28	Wang et al. (2003)
25	Hsiaolin	Taiwan, China	2009	Sandstone/Shale	Rainfall	23.97	980	3100	0.32	Kuo et al. (2013)
26	Mount Ontake	Japan	1984	Pyroclastic rock	Earthquake	34	1600	13000	0.12	Smith and Hungr (1992)
27	Kuridaira	Japan	2011	Sandstone/Shale	Rainfall	23	800	1350	0.6	Van Tien et al. (2018)
28	Leyte	Philippines	2006	Sandstone/Breccia	Earthquake, Rainfall	9.2	840	3800	0.22	Evans et al. (2007); Sassa et al. (2010)
29	Bairaman	Papua New Guinea	1985	Limestone	Earthquake	180	600	3000	0.2	King et al. (1989)
30	Ok Tedi Mine	Papua New Guinea	1989	Siltstone/Limestone	Mining	50	500	2000	0.25	Hearn (1995)
31	Merapi Volcano	Indonesia	1998	Pyroclasts	Rainfall	2.4	2100	6000	0.35	Schwarzkopf et al. (2005)
32	Falling Mt.	New Zealand	1929	Sandstone/Mudstone	Earthquake	55	1201	4500	0.27	McSaveney et al. (2000)
33	Mangapoike	New Zealand	2018	Sandstones/Mudstones	Rainfall	8	200	1200	0.17	McGovern et al. (2021)
34	Mt. Fletcher	New Zealand	1992	Sandstone/Siltstone	Rainfall	10	1370	3806	0.36	McSaveney (2002)
35	Frank	Canada	1903	Limestone	Mining, Rainfall	11	250	1805	0.14	Cruden and Hungr (1986)
36	Hope	Canada	1965	Greenstone/Serpentine	Earthquake	47	800	1600	0.5	Bruce and Cruden (1977)
37	Mt. Munday	Canada	1997	Ice/Gneiss	Freeze-thaw cycle	5	909	4545	0.2	Delaney and Evans (2014)
38	Mt. Meager	Canada	2010	Granite/Gneiss	Weather	40	2100	11000	0.19	Guthrie et al. (2012)
39	Gros Ventre	USA	1925	Sandstone/Shale	Earthquake	40	640	3370	0.19	Voight (1978)
40	Madison Canyon	USA	1959	Schist/Gneiss	Earthquake	20	400	1480	0.27	Hadley (1978)
41	Sherman Glacier	USA	1964	Metasandstone/Metasiltstone	Earthquake	12	1100	6000	0.18	McSaveney (1978)
42	Allen	USA	1964	Ice/Gneiss	Earthquake, Rainfall	23	1149	7600	0.15	Post (1967)
43	Lituya Bay	USA	1958	Schist	Earthquake	30.6	915	1350	0.36	Tocher and Miller (1958)
44	Huascarán[1]	Peru	1962	Granodiorite	Volcanic	16	3880	16880	0.23	Plafker and Ericksen (1978)
45	Huascarán[2]	Peru	1970	Granodiorite	Volcanic	58	3880	16880	0.23	
46	Mayunmarca	Peru	1974	Sandstone/Siltstone	Rainfall	1000	1600	8000	0.2	Hutchinson and Kojan (1975)
47	Glaciar Pucajirca	Peru	2002	Granodiorite/Ice	Weather	15	540	1250	0.43	Hubbard et al. (2005)

in this region, accompanied by the intense orogeny during the Cenozoic Era. This produces a series of EW young fold mountains in the Eurasian Plate, such as the Atlas, Alps, Caucasus, and Himalaya. These young fold mountains have an average elevation of 3000–6000 m and are strongly affected by active tectonic deformation, frequent seismic events, and strong glacial action.

The Circum-Pacific orogenic belt is the boundary between the continents and the Pacific Ocean, where the most frequent earthquakes and the most active volcanoes occur. Its length is approximately 40,000 km. Due to the continuous expansion of the mid-ocean ridge, the oceanic Pacific plate is subducted under the continental plates on both the east and west sides. This tectonic process created the longest S–N mountain ranges along the western coast of the American continent (i.e. the Cordilleras with mean elevations of 2000–4000 m). For the same reason, the central mountain range (Taiwan, China) and some island arcs, including the Philippine Islands, the Ryukyu Islands, and the Japan Islands, are formed in East and Southeast Asia with mean elevation of 1000–3000 m. The Frank rockslide (Cruden and Varnes, 1996), Mayunmarca rockslide (Hutchinson and Kojan, 1975), Leyte rockslide (Evans et al., 2007), and some other catastrophic events occur in this belt.

2.2. Classification of high-altitude and long-runout rockslides in the Qinghai-Tibet Plateau and surrounding areas

As presented in Fig. 1 and Table 1, the catastrophic rockslides are widely distributed in the Qinghai-Tibet Plateau and surrounding mountainous areas, China. For achieving risk control and mitigation of the high-altitude and long-runout rockslides in these areas, it is necessary to understand the dynamics of its high-speed movement, identify the potential initiation zone of rockslides accurately, and effectively assess its moving range as well as the secondary disaster. Thus, this section mainly discusses the hazard processes and the characteristics of velocity and distance in the study areas, and proposes associated classifications based on the long-runout rockslides parameters.

(1) Characteristics of the high-altitude and long-runout rockslide

Statistical results show that the disaster chains in the Qinghai-Tibet Plateau and surrounding mountainous areas can be divided into two categories, i.e. special and general disaster chains (Yin et al., 2021a). The special disaster chain is defined as the chain that is released from a high altitude and accumulates downstream after a high-speed movement, such as a process of rockslide-debris avalanche-debris flow. In contrast, the general disaster chain encompasses both the special disaster chain and the secondary chains it provokes, such as the process of dam-outburst and flood landslides due to lateral erosion downstream.

According to the characteristics of the disaster chain, the high-altitude and long-runout rockslides in the study areas can be generally divided into three zones: initiation zone at high altitude, transition zone with significant erosion and entrainment, and

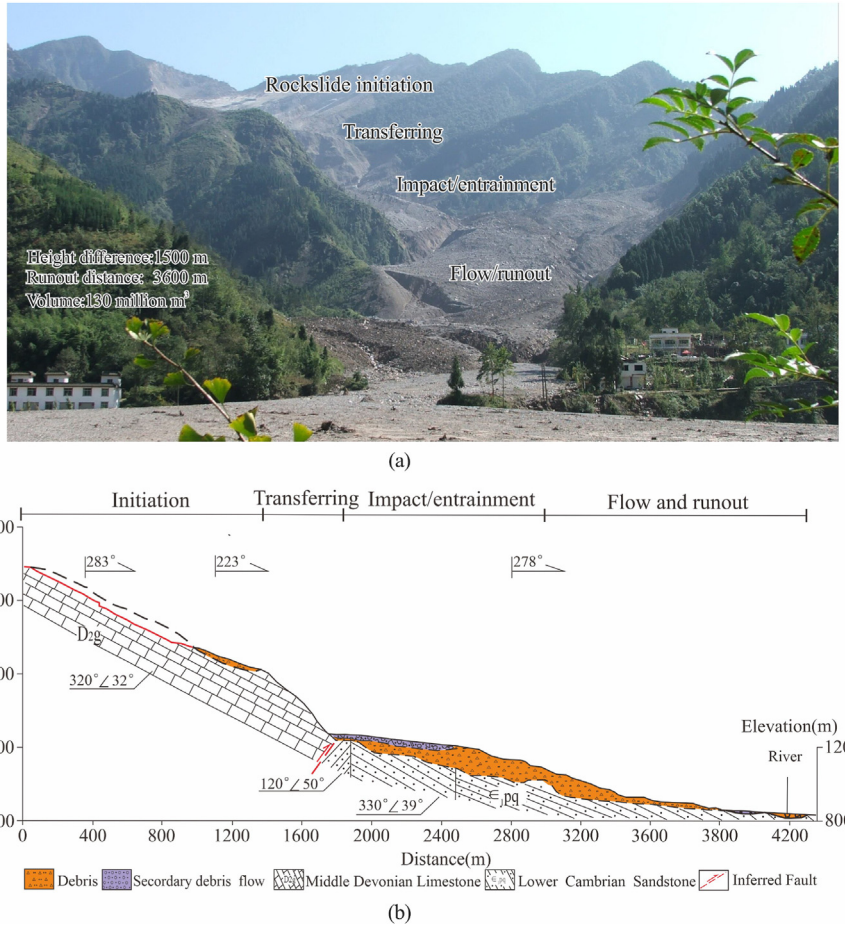

Fig. 2. Dynamic zoning of high-altitude and long-runout rockslides and debris at Wenjiagou, Wenchuan, China: (a) Overview of the rockslide-avalanche-debris flow; and (b) Profile of the rockslide avalanche and dynamic zoning.

deposition zone with material-flow characteristic (see Table 2, Fig. 2).

(2) Classification of the high-altitude and long-runout rockslides

Based on the analysis of height difference, runout distance, and runout velocity, the classification of the high-altitude and long-runout rockslide in the Qinghai-Tibet Plateau and surrounding areas can be made (Table 3). Four classes are proposed according to the height difference between the shear outlet and the mountain: extremely high (>1000 m), high (1000–100 m), moderate (100–50 m), and low (<50 m). In addition, four classes are classified according to the runout distance: extremely long (>5000 m), long (5000–1000 m), moderate (1000–100 m), and short (<100 m).

The moving velocity is divided into seven scales, and then updated by International Union of Geological Sciences Working Group on Landslides (1995) and Cruden and Varnes (1996). However, the scale "Extremely rapid (5 m/s)" in their classification is not suitable for the actual velocity of rapid rockslides in the Qinghai-Tibet Plateau and surrounding areas. Therefore, according to many disastrous events in study areas, the velocity of the high-speed rockslides should be greater than 20 m/s. Thus, a new classification based on runout velocity is proposed: extremely rapid, rapid, moderate, and slow (Table 3).

Next, the emergency response time (human response) for rockslides at different velocities is analyzed (Table 4). The emergency response time is divided into three categories: nil, nil-evacuation, and evacuation. When rockslide reaches a hypervelocity with a speed of over 70 m/s, the possibility of evacuation within 10 s is extremely low. If the lateral escape velocity of downstream personnel is 0.5–5 m/s, the survival possibility would be increased significantly if there is 90 s to response. For example, the total runout distance of the Yigong rockslide is 10 km. Assuming that the average moving speed is 82 m/s, the sliding mass could reach 7.4 km from the starting point in 90 s. Correspondingly, right at the position of 7.4 km downstream, if a person's actual running speed is 0.5–5 m/s, one could then be 45–450 m from the sliding path. Since the gully is flat and the lateral width of the sliding body is less than 1000 m, the possibility of evacuation is high with the 90 s responding time (Yin et al., 2011).

Table 2
Dynamic zoning and characteristics of high-altitude and long-runout rockslide.

Zone		Geologic feature	Dynamic feature	Basic criterion
Initiation zone		Unstable faulted and folded mountain at high altitude under the long-term gravity creeping, especially the one is triggered by heavy rainfall, earthquake, snow thawing, or even mining	Initializing rock mass has a high gravitational potential energy	Limit equilibrium
Transition zone	Transferring zone	After rockslide at high altitude, the potential energy will transfer to kinetic energy, and the accelerating movement at the steep slope occurs. An extra runout distance will be increased over trap topography	The potential energy of rockslide avalanche transfers to kinetic energy. The accelerating effect of flowing is obvious, and causes the successive impact	Energy conservation; Conservation of momentum; Impact theory, etc.
	Impact/ entrainment zone	The debris rockslide/ avalanche impacts and entrains the ground, then transfers into rapid fragment flow; the volume of debris mass is increasing, and the effect of damming-outburst occurs	The volume is significantly increasing due to the damming-outburst and the entrainment. The sliding mass transfers into debris mass	Conservation of mass; Conservation of momentum; Friction model; Coulomb model, etc.
Deposition zone		The debris rockslide/ avalanche transfers into flow with the effect of liquefaction or fluidization, then deposit at the wide and gentle topographic zone	The water-content of debris mass increases. Lon-runout distance is increasing due to liquefaction or fluidization, but the wide and gentle topography will reduce the distance and velocity	Conservation of mass; Conservation of momentum; Voellmy model; Particle flow model, etc.

Table 3
Recommended classification on high-altitude and long-runout rockslides.

Released height		Runout distance		Estimated velocity	
Height difference (m)	Class	Distance (m)	Class	Velocity (m/s)	Class
≥1000	Extremely high	≥5000	Extremely long	≥70	Extremely rapid
1000–100	High	5000–1000	Long	70–20	Rapid
100–50	Moderate	1000–100	Moderate	20–1	Moderate
<50	Low	<100	Short	<1	Slow

3. Sliding-prone geostructures and initiation mechanisms

3.1. Typical high-altitude and long-runout rockslides at faulted mountains

The most frequent high-altitude and long-runout rockslides occur in the Qinghai-Tibet Plateau are affected by tectonic activities, such as nappe, strike-slip, and extension. The geological conditions, including mélange strata, fault activities, and mountain structure, control the occurrence of geohazards. Meanwhile, the sliding-prone geostructures of high-altitude and long-runout rockslides include the ophiolitic soft-rock mountain, the layered structure mountain, and wedge-shaped structure mountain.

(1) The sliding-prone geostructure of the soft-ophiolitic rock belt

These rockslides mainly occur in complex soft-rock tectonic belt where the initiation zone is composed of weak mylonitized and pulverized ophiolite. The Baige rockslide, for example, occurred in the Jinsha River, in 2018 (Fig. 3a and b). The stratum of initiation zone is serpentinite of the Late Devonian and Middle Permian, including serpentinized peridotite, layered gabbro, diabase, pillow basalt, etc. and the rock mass is fragmented with intensive mylonitization. The stratum in the lower part of the Baige rockslide is hard Proterozoic gneiss, which thus forms an "upper soft and lower hard" structure (Zhang et al., 2020a). Furthermore, the rockslide failure is the result of the long-term creeping deformation and damage of soft ophiolitic-rock mass. The schistosity inside the metamorphic rocks such as ophiolite, gneiss, and phyllite is often

Table 4
Estimated velocity and emergency response time of high-altitude and long-runout rockslides.

Scale	Class	Estimated velocity (m/s)	Typical case	Runout distance and response times (s)		
				10 s	60 s	90 s
4	Extremely rapid	≥70	Yigong rockslide Yin and Xing (2012)	>700 m Nil	>4200 m Nil-evacuation	>6300 m Evacuation
3	Rapid	20–70	Zhaotong debris (Tang, 1991)	200–700 m Nil	1200–4200 m Evacuation	1800–6300 m Evacuation
2	Moderate	1–20	Qianjiangping rockslide Yin and Peng (2007)	10–200 m Evacuation	60–120 m Evacuation	90–1800 m Evacuation
1	Low	<1	Kamenziwan rockslide Yin et al. (2020)	>10 m Evacuation	>60 m Evacuation	>90 m Evacuation

acting as the weak surface with the lamellae oblique to outside slope, tending to be conducive to creeping deformation and shear failure.

(2) Predominant layered sliding-prone geostructures

These rockslides usually occur in layered sedimentary and metamorphic rocks of tectonic belt. The strata cut by faults in the initiation zone mainly include layered slate, sandstone, carbonate rock, and clastic rock. The lower strata consisting of gneiss, schist, and marble are hard. The Yigong rockslide, for example, located on the Jiali fault, consists of multiple near-parallel faults, which results in fragment of flysch and metamorphic rock mass. Meanwhile, there are many discontinuities in the layered slate of Carboniferous Laigu group in the initiation zone (Fig. 3c and d). The sliding body is prone to sliding along the weak-layered surface, as a result of gravity, earthquake, and snowmelt (Yin et al., 2000). The shear outlet where the fault extends lies at the contact zone between the Carboniferous Laigu and Luocuo groups. Besides, more than 70 moderate-strong earthquakes ($4.5 \leq Ms \leq 5.5$) have been reported in the past 50 years. Therefore, the amplification effect of earthquake on ground motion has also been accelerated in terms of the mountain deformation of Yigong source zone, due to strong fault activities since the Late Cenozoic.

(3) Wedged-shape sliding-prone geostructures

These rockslides occur in ancient strata of tectonic belt, which consist of gneiss, schist, quartzite. Examples are of the high-altitude rock-ice rockslides/avalanches in Sedongpu of Tibetan, China, and Chamoli of Uttarakhand, Indian (Fig. 3e and f), both of which occur in gneiss of the Himalaya orogenic belt. The strata in initiation zone consist of gneiss accompanied by a thick layer of glaciers, forming a rock-ice structure. Many discontinuities appear in Chamoli rock-ice mass, and the sliding body is wedge-shape under the cutting of three sets of discontinuities. The volume of initial failure is approximately 29.1×10^6 m^3. This rock-ice mass slid from 4500–6500 m with the height difference of 2000 m, and then transformed into wet-debris avalanche. The debris blocked the main stream after travelling 12 km. With the outburst of landslide dam, the flash flood damaged two hydroelectric plants downstream and killed 200 people (Shugar et al., 2021; Yin et al., 2021b; Zhang et al., 2022). It is likely that this disaster event experienced wedge-shape sliding of rock-ice, debris avalanche, barrier dam outburst, debris-flood, and flash flood.

The tectonic mélange belt and its adjacent metamorphic rocks, such as gneiss, slate, constitute the typical stratigraphic combination in the Qinghai-Tibet Plateau. The strata of rockslides include mélange belts, flysch strata, gneiss metamorphic rock bodies (layers), basalt eruptive rock bodies (layers), clastic rock strata, and carbonate strata. The outcropping location of fault and earthquakes also control the distribution and evolution of rockslides. As shown in Fig. 4, three mechanisms of high-altitude and long-runout rockslides controlled by fault are described. One is the creeping deformation of soft rock in the tectonic zone. The fragmented soft rock is prone to deforming and shearing out along the rock interface with strong horizontal compressive stress (Zhang et al., 2020b) (Fig. 4a). The second type is the middle and upper part of the mountain exposed by the fault. The ridge is affected by unloading stress or earthquake, and the overall geological structure is relatively fragmented. The lower part of the mountain is of good integrity, and a key locked section is formed at the fault. Huang et al. (2009) regraded the sudden brittle failure of "locked section" as "the retaining wall failure" effect. The locked section suffers sudden shear failure due to stress accumulation, forming a rockslide with initial velocity. This mode is common in earthquake mountainous areas in western China, under the action of long-term gravity and rainfall (Fig. 4b) (Yin et al., 2017b). The third type is the mountain located in the fault zone of the strong earthquake area. The rock mass is extremely fragmented due to the long-term tectonic action. Furthermore, the vertical seismic acceleration is greater than the horizontal acceleration. Thereby, the rock mass may be vibrated and thrown by strong earthquake (Fig. 4c), and the upper mountain also is sheared out at high altitude and then transforms into debris avalanche (Yin et al., 2009, 2011).

3.2. Typical high-altitude and long-runout rockslides at folded mountain

The upper Yangtze Platform of China is characterized by the folded mountains mainly composed of carbonate rocks, clastic rocks, metamorphic rocks, and basalt. A large number of high-altitude and long-runout rockslides occurred in this area, especially in the Qinli-Bashan Mountain folded belt, the Chuandong-Eyuqian folded belt, and the Qianzhong folded belt. The fold mountains in the upper Yangtze Platform are composed of a series of paralleled tight anticlines and open synclines with few exceptions (Fig. 5a). In the limb or core of the folds, the rockslides have different failure patterns due to the substantial differences in the topographic feature and rock mass structure (Fig. 5).

In the clastic rock mountain area, the most common high-altitude and long-runout rockslides formed in the broad synclinal valleys consisting of red beds are triggered by heavy rains (Yin et al., 2016; Li et al., 2022). The failure mode is bedding sliding (Fig. 5b). In the carbonate mountain area, many high-altitude and long-runout rockslides formed in the folded mountain, due to the shoe-shape landform (upper-thick-limestone cliff and lower-thin-mudstone/shale gentle slope) and the influence of underground coal/bauxite mining. In the core of the fold, there are two types of failure modes of the rockslides: (1) toppling in the anticlinal mountain (Fig. 5c), represented by the Jiguanling rockslide (Li et al., 2016) which is similar to the famous Frank rockslide in Canada; and (2) buckling in the synclinal mountain (Fig. 5d), represented by the Zengziyan rockslide (He et al., 2019). In the limb, the failure mode of the

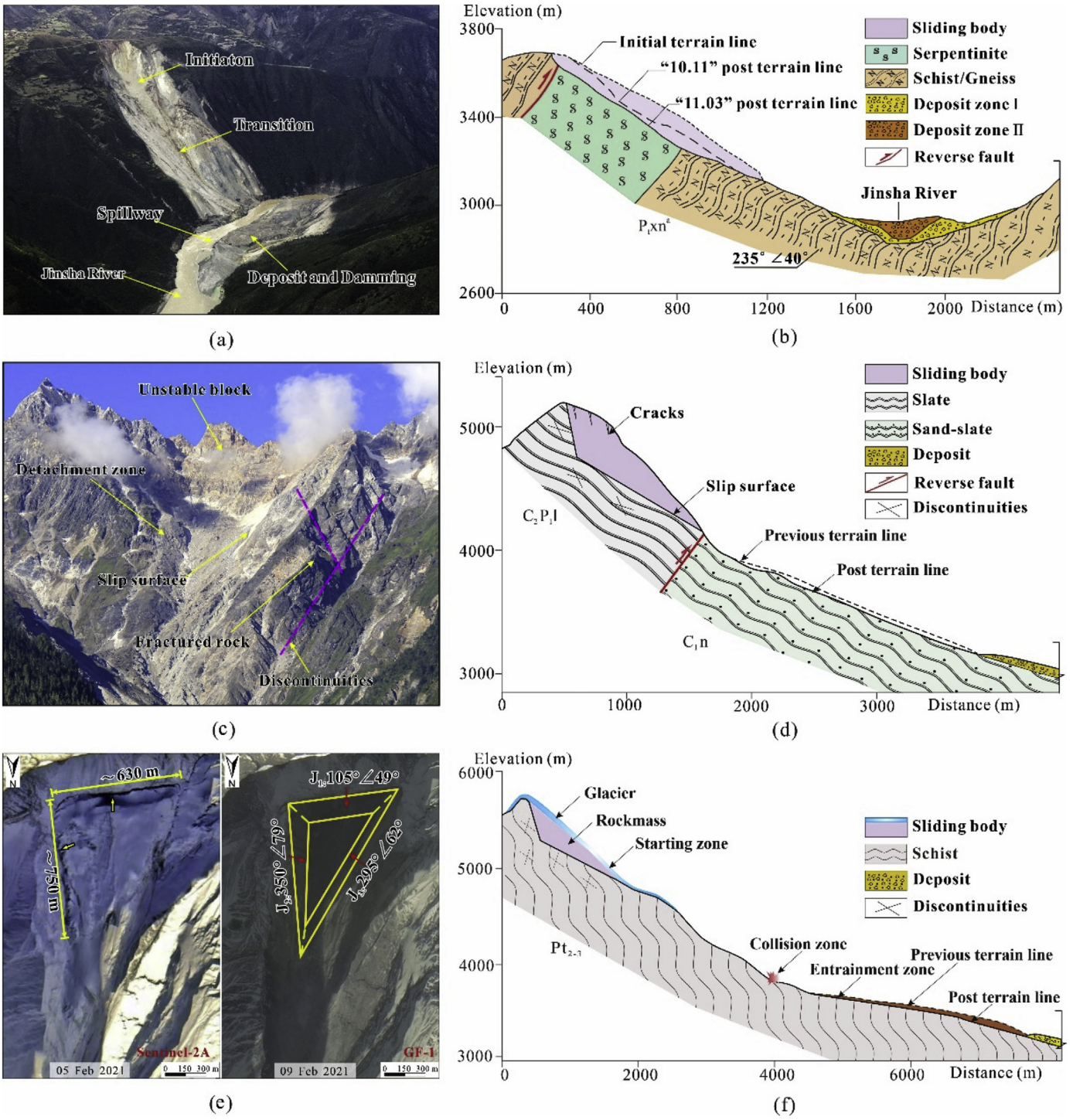

Fig. 3. Three typical sliding-prone geostructures and associated patterns in the Qinghai-Tibet Plateau tectonic belt: (a) and (b) Soft ophiolite geostructure controlling the Baige rockslide in the Jinshajiang tectonic belt; (c) and (d) Slate geostructure controlling the Yigong rockslide in the Jiali tectonic belt; (e) The mul-titemporal high-resolution remote sensing images of initiation zone; and (f) The wedged-shaped geostructure of rock and ice controlling initial failure in initiation zone and subsequently movement progress including collision and entrainment in Chamoli rock-ice avalanche. J_1, J_2, and J_3 represent the large discontinuity planes and the dip direction/dip angles is given in Chamoli rock-ice avalanche.

rockslides is bedding sliding or oblique-inclined bedding (Fig. 5e), which is represented by the Jiweishan rockslide (Yin et al., 2011). Additionally, many catastrophic high-altitude and long-runout rockslides in the upper Yangtze Platform formed in the flysch formations and basalts, which are represented by the Xinmo rockslide (Yin et al., 2017b) and the Touzhai rockslide (Gao et al., 2020).

(1) Geostructures of the rockslides in the carbonate rocks

The inclined limb and horizontal core layers of the carbonate folded mountains are easily to form large-scale high-altitude and long-runout rockslides. These mountains are composed of upper thick (greater than 200 m) carbonate rocks interbedded with 4–6

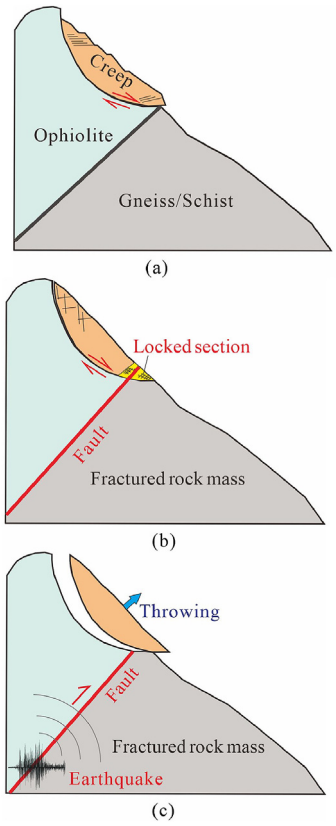

Fig. 4. Three typical rockslide modes in the Qinghai-Tibet Plateau tectonic belt: (a) Creeping and shear failure in the ophiolite belt; (b) Shear failure along the locked section; and (c) Throwing of the fractured rock mass triggered by the earthquake.

layers of soft thin bedding shales and lower gentle clastic rock slopes (Fig. 6a and b). This landform is beneficial for potential energy transformed to kinetic energy after failure, and thus, the rock avalanche or the long-runout debris flow forms and causes more serious damages (Yin et al., 2011; Gao et al., 2018).

Influenced by the long-term tectonic actions, joints, fractures, and weak interlayers are well-developed in the carbonate rock mass. These discontinuities control the rock mass strength and susceptibility to the occurrence of rockslide. Moreover, many pipes, caves, sinkholes, and other karst landscapes have been formed in this carbonate mountain area. Thus, the karst groundwater table rises and falls abruptly during the heavy summer rains, not only erodes intensely the karst mountains, but also causes substantial changes in the gas pressure in the karst pipes, resulting in final failure of the mountains (Fig. 6a and b). In the mountains where the top of the slope is composed of carbonate rocks and the slope waist is clastic rocks or basalts, large amounts of groundwater flows to the lithological contact zone during the rainy seasons, significantly affecting the stability of the slope (Fig. 6a). In addition, the carbonate mountain areas are rich in coal, bauxite, and irons. Long-term and large-scale underground mining accelerates the deformation and stress adjustment of the mountain. Finally, tensile-shear and compressive-shear failures occur in the key hard rocks covering the mining layer. After that, long-runout debris flows (distance is larger than 1000 m) are formed subsequently due to the special geomorphological condition represented by the upper thick steep carbonate rocks and lower gentle clastic rocks.

(2) Geostructures of the rockslides in the clastic rocks

The mountain areas in Eastern Sichuan fold belt, China are susceptible to high-altitude and long-runout rockslides. Large amounts of catastrophic rockslide events triggered by the heavy

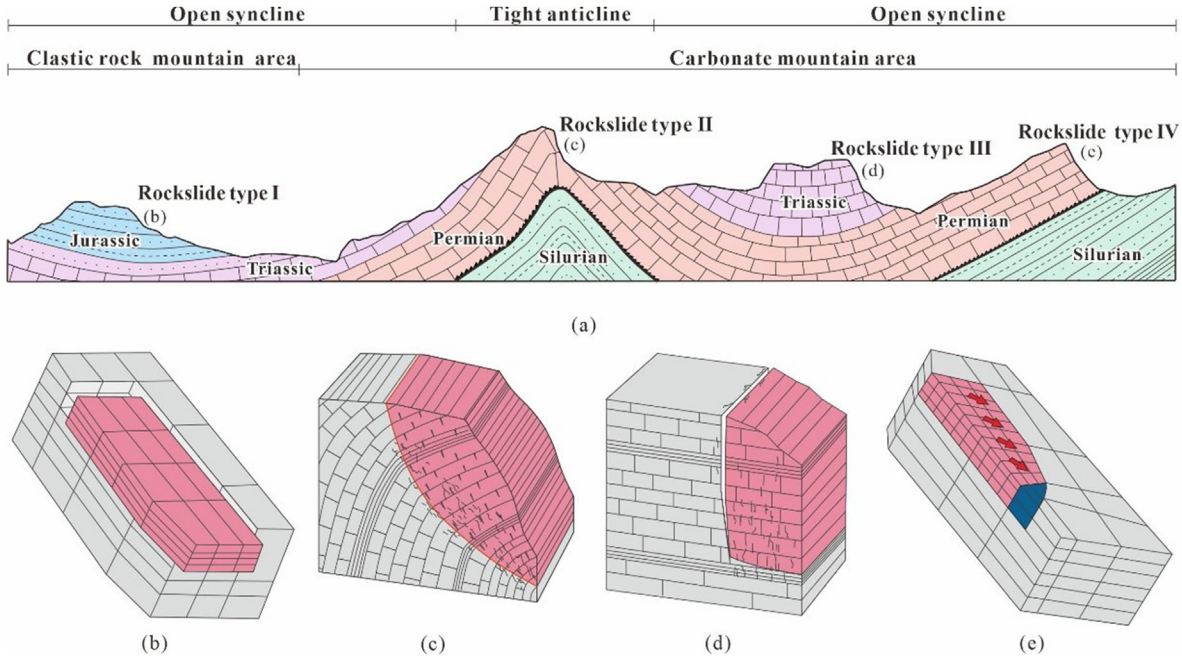

Fig. 5. Typical fold styles and rockslide modes in the upper Yangtze Platform: (a) Different rockslide sections of the folded mountains; (b) Bedding sliding rockslide; (c) Toppling rockslide; (d) Bottom-crashing rockslide; and (e) Apparent dip sliding of oblique inclined bedding rockslide.

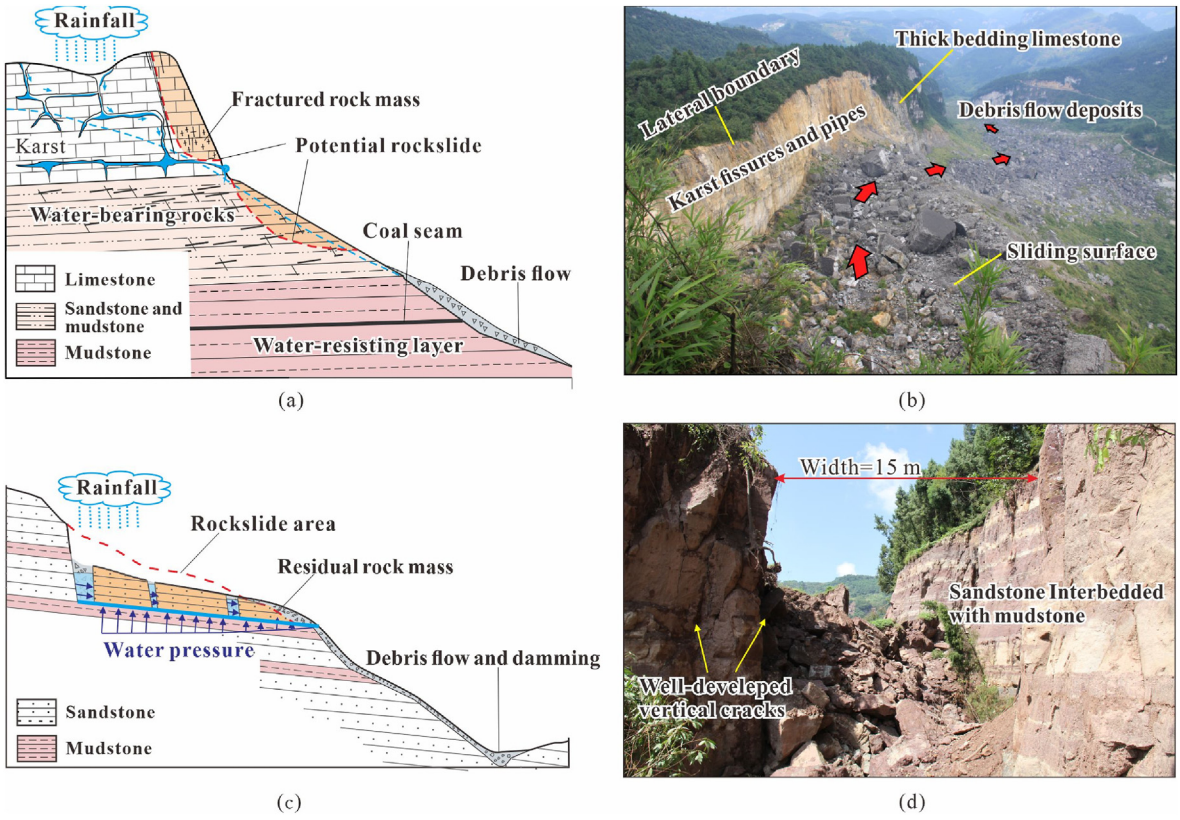

Fig. 6. Geostructure and geomorphology controlling the rockslide in carbonate and clastic rock layers in the upper Yangtze Platform: (a) and (b) Typical rockslide modes and characteristics in the carbonate mountain; (c) and (d) Typical rockslide modes and sliding cracks in the clastic rock mountain.

rain due to influence of the West China autumn rain occurred in these areas (Li et al., 2022). These rockslides mainly occur in Jurassic and Middle-Upper Triassic clastic strata containing weak surfaces or interlayers. The slip zones are low-strength mudstones, shales, lithological contact zone, and coal-bearing layers. In terms of hydrogeology, the high-altitude and long-runout rockslides in this area generally have good permeable (water-containing) geological units, and the groundwater is dominated by fissure water and karst water. Groundwater infiltrates rapidly during the heavy rain, weakening the interlayer and producing high water pressures. Therefore, the sliding force increases and sliding resistance is reduces due to rainfall infiltration. This is the cause of the rockslide (Fig. 6c and d).

(3) Geostructures of the rockslides in the flysch formation mountain

The flysch formation uniquely forms in the active tectonic belt. It has complex composites and rock heterogeneity. During the long-term tectonic action, the flysch formation mountain is prone to forming different scales of folds. Obvious bedding dislocation and dissipation occur in certain parts of the mountain, resulting in decrease of the integrity of rock mass. The flysch formation is widespread in the Qinling and Longmenshan areas of China. They mainly consist of metamorphic sandstone, slate, quartz schist, and phyllite. In 2017, a high-altitude and long-runout rockslide characterized by bedding sliding occurred in Diexi Town, Sichuan Province, China (Fig. 7a and b). The rockslide is located on the west wing of the forearc of the arcuate tectonic belt where the active fault is well developed. The rockslide is composed of Middle-Upper Triassic Zagunao flysch formation (metamorphic quartz sandstone interbedded with phyllite and slate) cut by multiple groups of joints. Under the tectonic compression and gravity, the flysch formation was flexed and dislocated, leading to the bedding rockslides (Yin et al., 2017b).

(4) Geostructures of the rockslides in the basalt

The Emeishan basalt formation is widely distributed in the southwestern margin of the Upper Yangtze Platform, China, such as the Touzhai rockslide and the Shuicheng rockslide (Fig. 7c and d) (Gao et al., 2020). This basalt formation is produced by multi-stage magmatic eruptions. Affected by the long-term tectonic action, the zone between different-stage basalts often has the dislocation surface or belt, which is a weak part of the basalt rock mass. The limb of the basalt fold mountain often forms a stepped landform. Rockslides frequently occur in this area under the effects of groundwater infiltration, water evaporation, and rock weathering. Columnar joints are well-developed in the basalt rock masses. Coupled with the tectonic fractures and weathered fissures, the basalt rock masses are fractured or even fragmented. Small-diameters (5–20 cm) basalt blocks are widely shown in the rockslide deposits (Xu et al., 2007).

3.3. Initiation mechanisms and patterns of high-altitude and long-runout rockslides

Based on the analysis above, the high-altitude and long-runout rockslides in the Qinghai-Tibet Plateau and adjacent areas have various failure modes and initiation mechanisms due to the influences of various tectonic setting, strata, landform, and other geological structures.

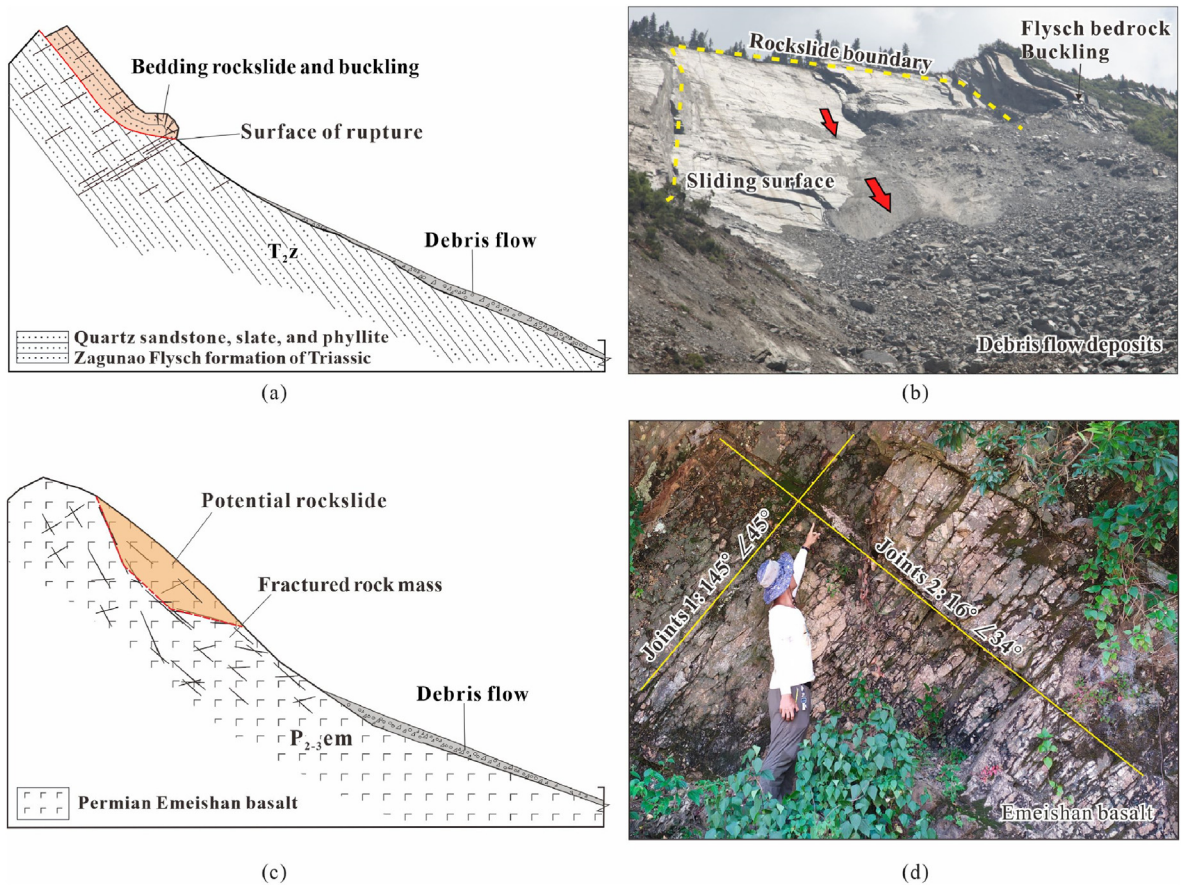

Fig 7. Geostructure and geomorphology controlling the rockslide in flysite and basalt layers in the upper Yangtze Platform: (a) and (b) Typical rockslide modes and characteristics in the flysite mountain; (c) and (d) Typical rockslide modes and geostructures in the basalt mountain.

Table 5
Geomorphology of typical high-altitude and long-runout rockslides in the Western China.

Geomorphologic division	Topographic features	Geomorphic features			Disaster chain features	Dynamic effects
		Initiation zone	Transition zone	Deposition zone		
Deep canyon of Qinghai-Tibet (high and extra-high mountains)	Bending, Long and narrow, Deep-cutting valleys, Height difference (>3000 m)	Extra high-altitude rock-ice avalanche mountains	Glacier, Glacial till	Gigantic damming deposit	Extra high-altitude rock-ice avalanche-river blocking-outburst flood, Runout distance (>10 km)	Air cushion, Dynamic fragment, Pound entrainment,
Middle mountain canyon of Qinghai-Tibet margin orogenic belt	Deep-cutting valleys, Height difference (500 −2000 m)	High-altitude mountains with seismic cracking	Valleys, loose seismic deposit	Large damming deposit	High-altitude and long-runout rockslide-debris avalanche-river blocking, Runout distance (<5 km)	Valley damming, Flowing deposit, River blocking and outburst flood
The upper Yangtze Platform	Step-like cliffs, Flat valley, Height difference (<1000 m)	Folded mountains with cliffs	Gentle slopes with cliffs, rock debris deposit	Loose deposit	High-altitude and long-runout rockslide-debris avalanche, Runout distance (<2 km)	Dynamic fragment, Pound entrainment, Valley damming, Flowing deposit,

The high-altitude and long-runout rockslides occurring in the Qinghai-Tibet Plateau are mainly distributed in the orogenic belts, such as the Himalayan orogenic belt and the Longmenshan nappe tectonic belt. The location and current activity of the mega tectonic belts determine the mountain structure, internal and external triggers, and the topographic features. Three types of initiation mechanisms of the high-altitude and long-runout rockslides are summarized in this area (Fig. 4): (1) failure of the soft ophiolitic

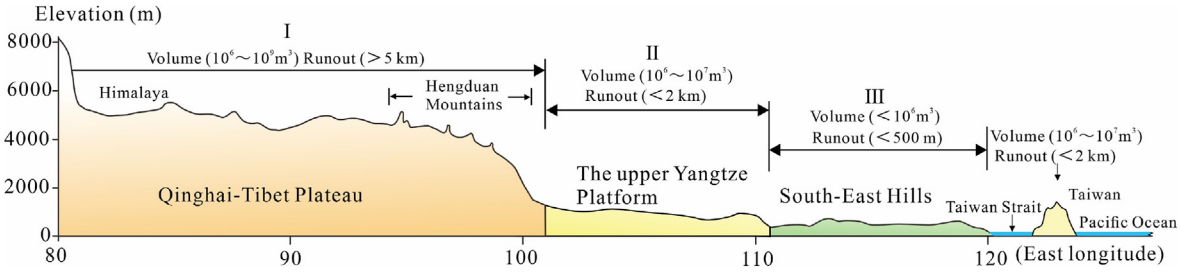

Fig. 8. Characteristics of high-altitude and long-runout rockslides in the three different topographic step regions of the Chinese mainland (I-first topographic step, II-second topographic step, III-third topographic step).

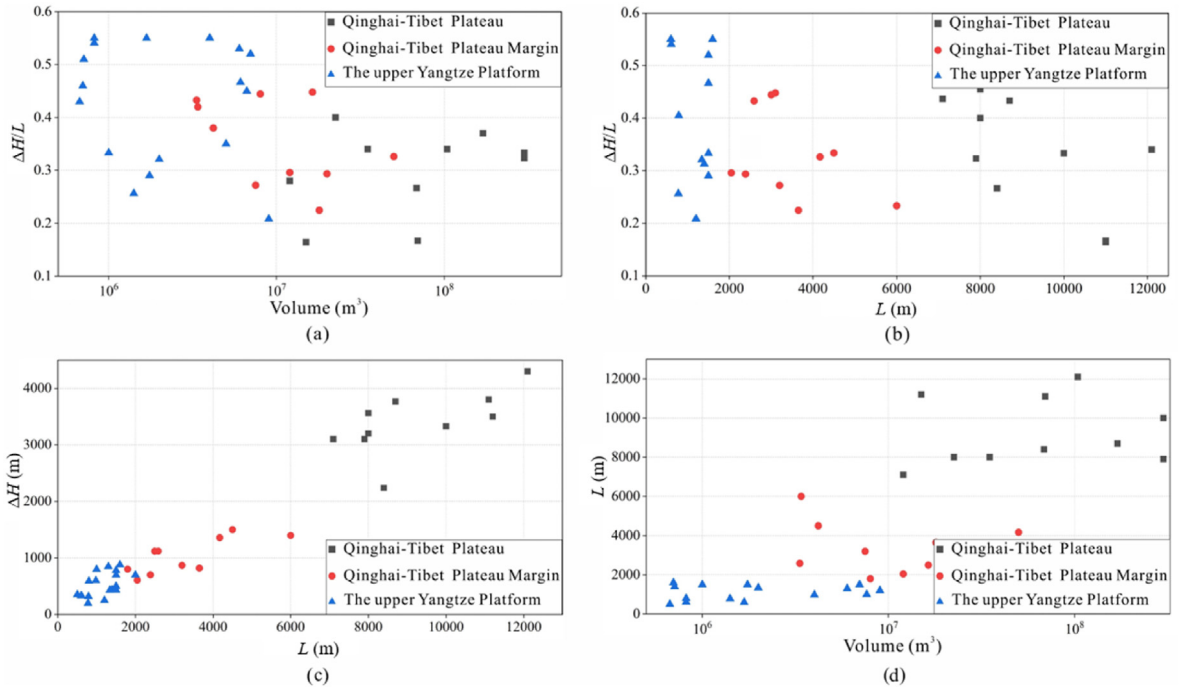

Fig. 9. Geomorphic parameter relationships of typical rockslides: (a) Apparent coefficient of friction ($\Delta H/L$) versus volume of rockslide-debris avalanche; (b) Apparent coefficient of friction versus runout distance (L); (c) Height difference (ΔH) versus runout distance (L); and (d) Runout distance (L) versus volume of rockslide-debris avalanche.

mélanges in the tectonic belt undergoes creeping deformation under long-term gravity and rainfall; (2) sudden failure of the fractured mountain in the structural belt controlled by the dominant structural planes, after the actions of frequent seismic events and freeze-thaw cycle; and (3) failure of the faulted mountain triggered by a strong earthquake, in which the seismic acceleration causes the hanging wall to swell and throw.

The upper Yangtze Platform of China almost experiences heavy rainfalls yearly. On the carbonate mountains, the groundwater is dominated by the karst pipe flow. Water level and water pressure in the karst pipeline surging during the rainy season induce the failure of the pipe wall and rock mass in the karst mountain. During the heavy rain season, high hydrostatic and hydrodynamic pressures are produced in the saturated/unsaturated clastic rock mountain cracks, and the weak interlayers are softened. Additionally, continuous underground coal mining triggers many large-scale rockslides in mountains consisting of the coal-bearing stratum in southwestern China. Underground mining can cause the bending, separation, and fracturing of the overburden rocks, and can increase substantially the height of the water-conducting fractured zone (Li et al., 2022). After a certain period, a chain reaction would be triggered. The chain includes uneven settlement of the overburden rocks, damage and crushing of the mountain base as well as cracking of the mountain top, buckling failure of the mountain (Li et al., 2016, 2022).

3.4. Geomorphic characterization of long-runout disaster chain

The occurrence of high-altitude and long-runout rockslides has a close relationship with the regional geomorphological units. The scales, kinematics and dynamic characteristics of rockslides are also closely connected with micro-geomorphology. The zonal characteristics in China can be classified into three topographic steps: the Qinghai-Tibet Plateau, upper Yangtze Platform, and South-East Hills (Guo and Cui, 2013), as shown in Table 5 and Fig. 8. Many scholars often take apparent coefficient of friction ($\Delta H/L$; where ΔH is the total height difference and L is total horizontal distance (Hsü, 1975)) as an important parameter to describe the runout characteristics of long-runout rockslide (Storm et al., 2019; Dufresne et al., 2019; Melo et al., 2022). Thirty-two catastrophic rockslides over the past 100 years occurred in China are analyzed well. The relationship between apparent coefficient of friction and volume, runout distance, fall height and runout distance is studied. It can be seen from Fig. 9a that the ratio $\Delta H/L$ shows a large scatter with volume, but the overall decreasing tendency matches with increasing volume. It

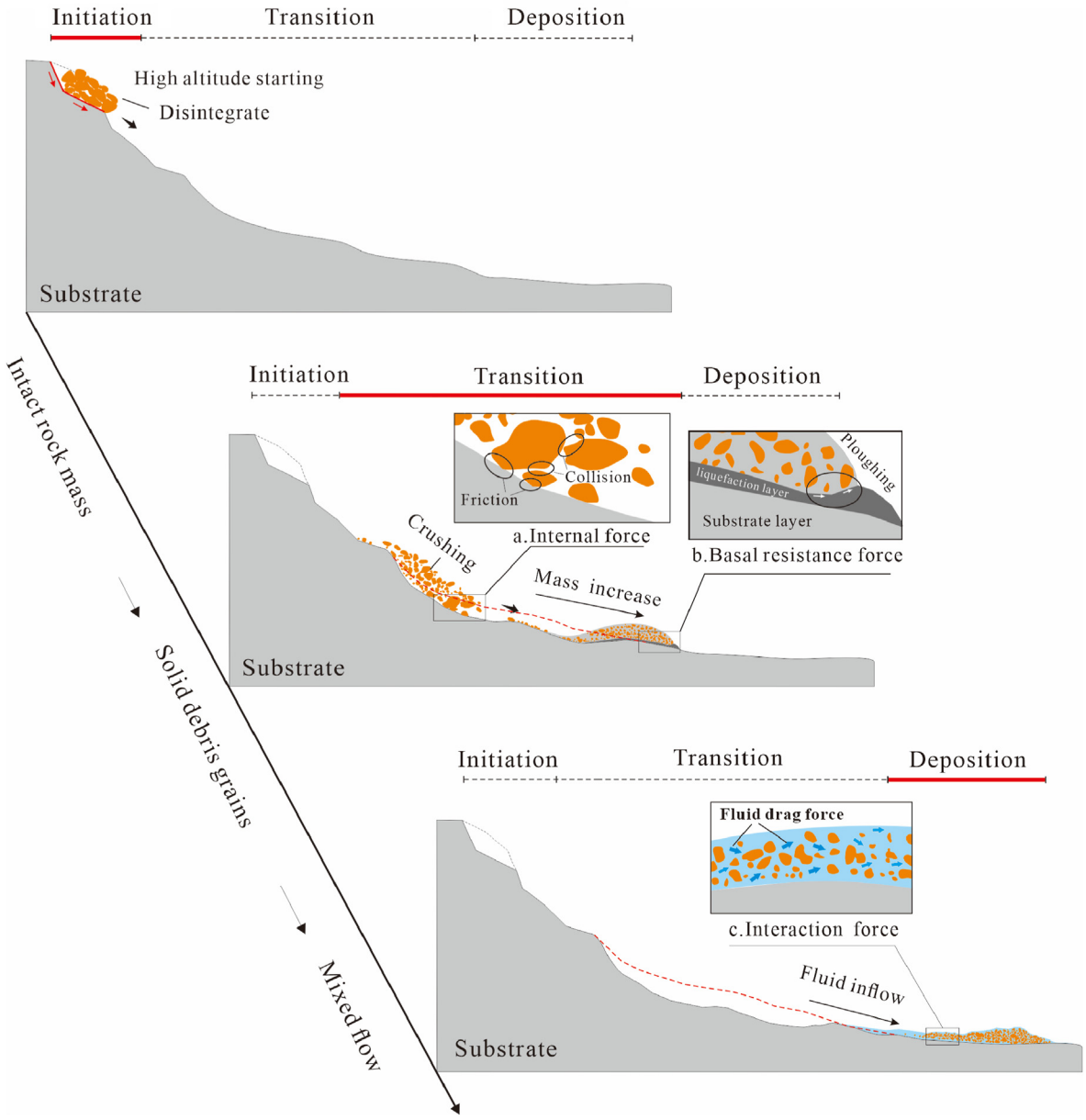

Fig. 10. Movement zoning and dynamic process of high-altitude and long-runout rockslide.

also clearly shows that the volume generally exceeds 10×10^6 m^3 in the Qinghai-Tibet Plateau regions, however, less than 10×10^6 m^3 in upper Yangtze platform. In addition, the runout distances of rockslides exceed 2 km in the Qinghai-Tibet Plateau Margins, even surpassing 10 km in the Qinghai-Tibet Plateau (Fig. 9b). Nevertheless, the rockslide travels less than 2 km in the upper Yangtze platform. It is referred that the travelling distance (>10 km) may be related to micro-topography, such as the lubrication of glaciers, snow, and glacial till, which are common in the Qinghai-Tibet Plateau regions (Table 5). As can be seen from Fig. 9c and d, the height difference and volume seem to be a positively linear with increasing runout distance. The greater the height difference and volume, the greater the potential energy. This suggests that the sliding body would obtain a greater runout velocity due to momentum conversion.

According to above analysis, it is likely that micro-topography plays an important role in high mobility. The height difference of valleys is usually larger than 3000 m, and glacier, moraine, and snow that are conducive to debris avalanche travelling lie at the valley floor in the Qinghai-Tibet Plateau areas. Conversely, there are relatively few lubricating substances in the upper Yangtze Platform accompanied by the height difference (lower than 1000 m). Thereby, the rockslides travel less than 2000 m, far less than that of the Qinghai-Tibet Plateau areas.

4. Dynamics of high-altitude and long-runout rockslides

4.1. Dynamic process and behavior of high-altitude and long-runout rockslides

4.1.1. Movement zone and dynamic process

High-altitude and long-runout rockslides have a complex dynamic process. According to the evolutional characteristics, this

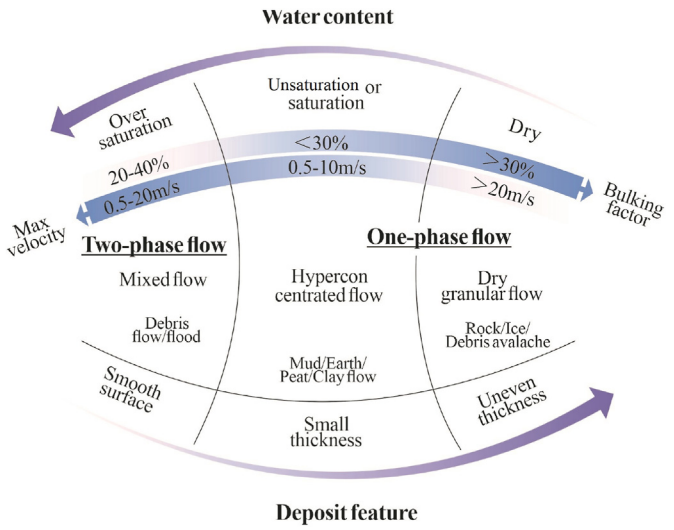

Fig. 11. Classification of high-altitude and long-runout rockslide as a function of material composition.

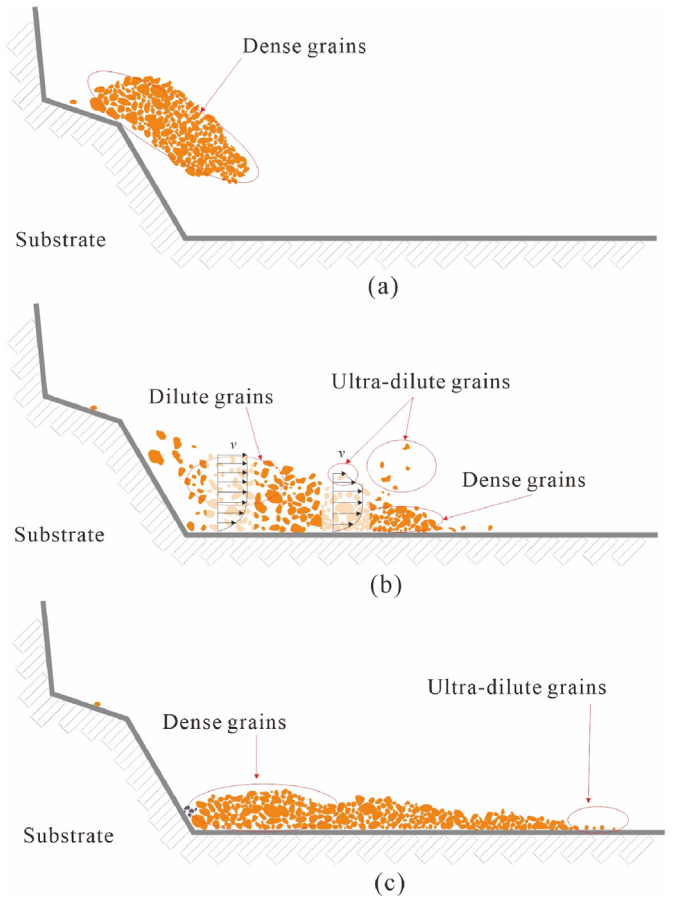

Fig. 12. Various states of sliding main body at three movement stages of high-altitude and long-runout landslide: (a) Sliding body separates from initiation zone, and the granular flow is dominated by dense granular states; (b) Sliding body gradually fragments and the granular flow reflects three states of dense, dilute, and ultra-dilute; and (c) Sliding body stops and the granular flow returns to a dense state.

process can be divided into three movement zones (i.e. initiation zone, transition zone, and deposition zone) (Fig. 10).

(1) Initiation zone. Rockslide or rockfall with large volume initiates under various adverse exogenic and endogenic factors. The rock mass slides or collapses and maintains a relatively intact structure in this dynamic process. After leaving the starting position, the rock mass obtains a large amount of kinematic energy, and differential movement occurs in small-scale rock blocks cut by discontinuities (e.g. joints), thereby resulting in disintegration (Pollet and Schneider, 2004; Yin and Xing, 2012; Gao et al., 2022a).
(2) Transition zone. With the continuous acceleration of rockslides, further disintegration and crushing resultant from collision and differential shear make the relatively intact rock mass break into numerous fragments and transform into rapid granular flow (Pollet, 2004; Locat et al., 2006; Knapp and Krautblatter, 2020). A series of dynamic effects in granular scale, such as segregation, mixing and dilate controlled by collision and friction, determine the flow regimes of landslide. In addition, during the rapid movement of granular flow, a considerable amount of loose substrate is likely to erode and entrain into the granular flow, which enlarges the volume greatly. The liquefaction effect may occur if low-friction or water-bearing substrate is entrained into the bottom of the granular flow (Heim, 1932; Takahashi, 1978, 2007; Yin et al., 2009; Wang et al., 2014; Iverson and Ouyang, 2015; Gao et al., 2020; Yin and Wang, 2020). Furthermore, the entrainment of enough water-bearing units and surface water can convert a dry granular flow into debris flow with more mobility, leading to increased assessment difficulty (Takarada et al., 1999; Dufresne, 2012; Gao et al., 2022b).
(3) Deposition zone. With the gradual consumption of kinetic energy, the velocity of granular flow decreases and the grains are bulldozed to halt. In the flat terrain in this zone, where the local people settle, the deposition zone can seriously threaten the safety of human life and property.

4.1.2. Dynamic behavior of high-altitude and long-runout rockslides

Currently, the classifications of landslides by Varnes (1978) and then updated by Hungr et al. (2014) are accepted widely. Long-runout rockslides are composed of many discrete solid grains, and the interstitial of these grains are filled with fluids (water or air). So, considering the material composition of the moving mass as a crucial factor, this study presents the various dynamic behaviors as follows (Fig. 11):

(1) Dry granular flow. The granular flow with intensive fragmentation is usually filled with air. Study of the dynamic behaviors of dry granular flow makes it possible to understand the landslide travel without the need of water or slurry (Melosh, 1979; Davies, 1982; Campbell et al., 1995; Straub, 1996, 1997) (e.g. Jiweishan rockslide and Zhangjiawan rockslide).
(2) Hyper-concentrated flow. The moving mass is composed of small-size grains with the characteristics of lower bulking factor and high-water content. The deposition shape is relatively smooth, with small thickness (e.g. Zhenxiong rockslide and Yili rockslide).
(3) Mixed flow. This type of flow mostly occurs under heavy rainfall and glacier-melt conditions. The characteristics of runout and deposition are intermediate between dry granular flow and hyper-concentrated flow (e.g. Shuicheng rockslide and Sanxicun rockslide).

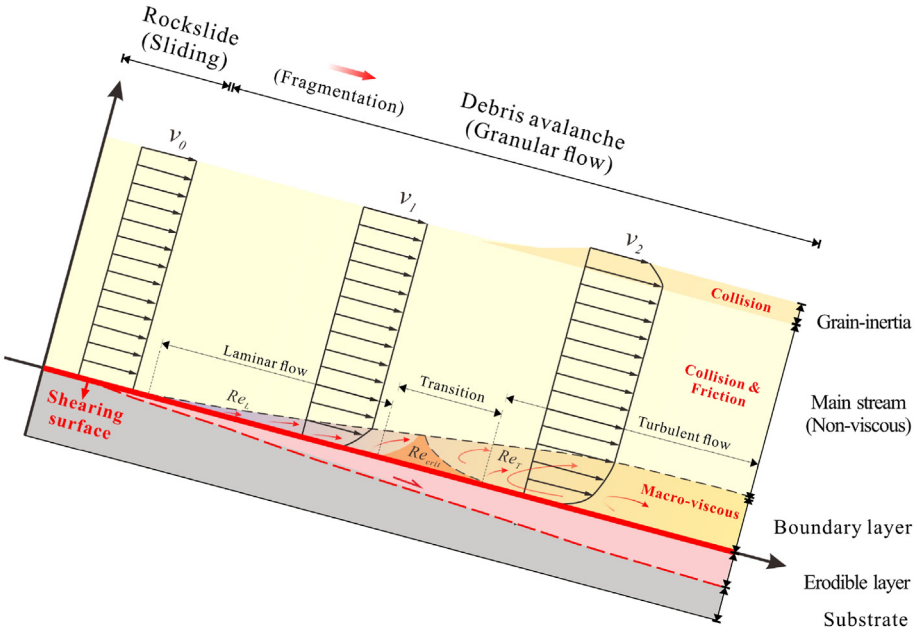

Fig. 13. Material stratification, velocity and mechanical action during the movement of the high-altitude and long-runout rockslide. That is mainly affected by the internal force, the basal resistance, and the interphase force.

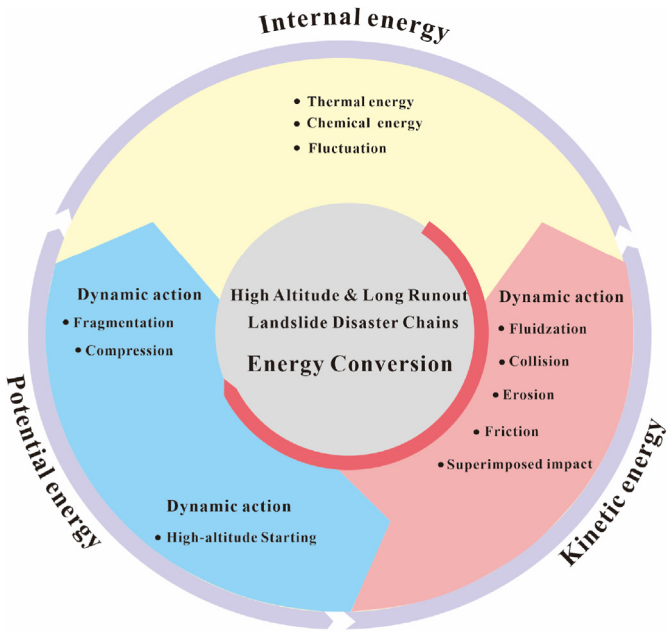

Fig. 14. Energy conversion during the movement of high-altitude and long-runout rockslides.

4.2. Movement process and dynamics of high-altitude and long-runout rockslides

4.2.1. Mass conservation and phase transition

The runout process of long-runout rockslides follows the mass conservation. The eroded material and fluid confluence are considered as the source term S_m. The mass conservation equation is written as

$$\frac{\partial \rho}{\partial t} + \nabla \cdot (\rho \boldsymbol{v}) = S_m \tag{1}$$

where ρ is the density (kg/m^3), t is the time (s), and ∇ is the divergence of the vector. S_m is calculated by

$$S_m = S_l + S_s \tag{2}$$

where S_l and S_s are the mass changes in liquid and solid, respectively.

The solid mass of the landslide changes all the time. The solid mass change S_s is mainly determined by mass gain and mass loss related to dynamic erosion (S_e) and deposition (S_d), respectively, and thus can be assessed by

$$S_s = S_e - S_d \tag{3}$$

Bedrock and loose materials in the substrate layer are entrained after dynamic erosion, which can enlarge the mass by several orders of magnitude (Abele, 1997; Egashira et al., 2001; Bouchut et al., 2008; Mangeney et al., 2010). However, a decrease in mass occurs when the landslide commences to deposit due to larger basal resistance. Liquid is very important to the fluidization of landslide and also is an important part of mass changes for landslide. The liquid mass change (S_l) is determined by the mass gain by rainfall (S_r) and surface runoff inflow or tributary inflow (S_i) and the mass loss by outflow (S_o):

$$S_l = S_r + S_i - S_o \tag{4}$$

where S_r is affected by rainfall intensity, rainfall duration, and catchment area. As for landslides with ultra-long runout distance, the mass change of the surface runoff or the inflowing liquid (S_i) is a non-negligible part (Keefer et al., 1987; Vessia et al., 2014; Melillo et al., 2015), which depends on the surface runoff and the number of tributaries. The fluid mass S_o decreases in the whole runout process, most of which loses in the form of infiltration into the ground.

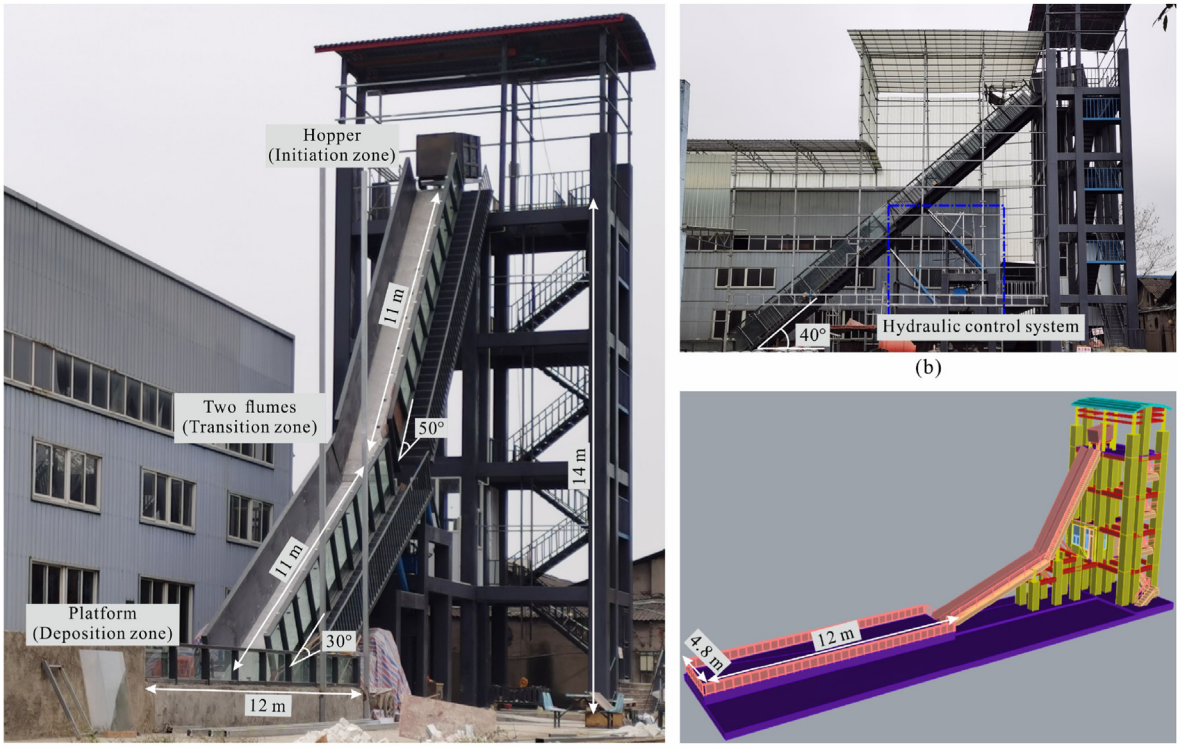

Fig. 15. Schematic diagram of large-scale physical model (experimental apparatus) for dynamic rockslide: (a) Photograph of experimental apparatus when the slopes of two flumes are 50° and 30°, respectively; (b) Photograph of apparatus when the slopes of both flumes are 40°; and (c) 3D model of this large-scale experiment apparatus. The hydraulic system consists of four hydraulic shafts, and the maximum axial force of each shaft is 16 tons (160 kN). Using this system, the slope of the two flumes can be changed freely.

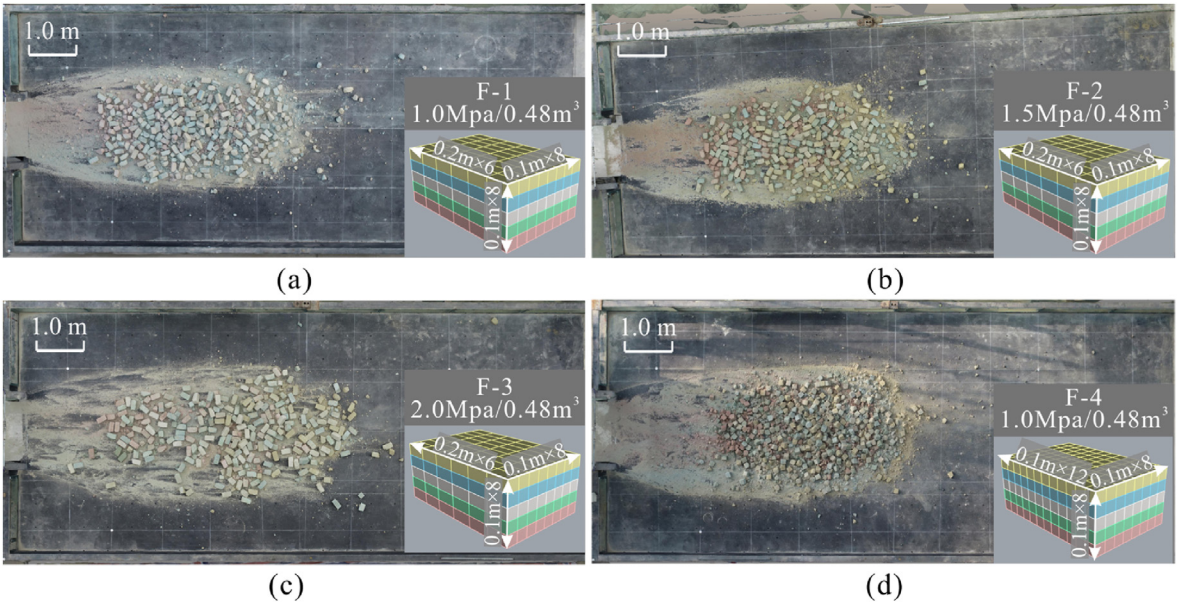

Fig. 16. Deposition images of jointed blocks with different structures after fragmentation. The jointed blocks are closely packed by an assembly of subblocks with different uniaxial compressive strengths of intact subblock: (a) 1 MPa; (b) 1.5 MPa; (c) 2 MPa, and (d) 1 MPa; and joint spacing reflected by the size of single subblock: 0.2 m × 0.1 m × 0.1 m and 0.1 m × 0.1 m × 0.1 m. The subblock is created by cementing together sand, barite, and gypsum cement with different ratios. The discontinuity settings are rough and completely penetrated without tensile strength. The slopes of two flumes during these experiments are adjusted as 50° and 30°, respectively.

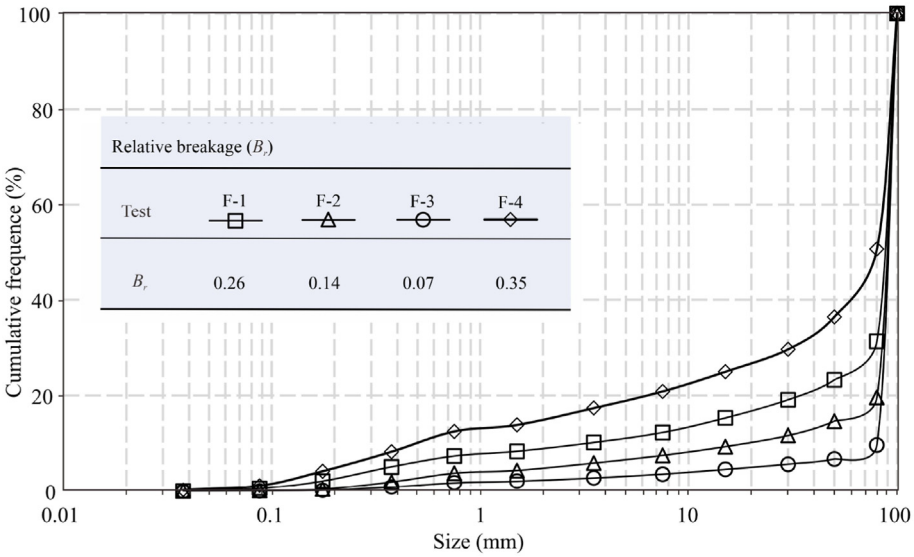

Fig. 17. Fragment size distribution curves obtained by sieve analysis tests of F-1 to F-4. The relative breakage ratio (B_r) has a position correlation with fragmentation degree, which is defined as the ratio to total breakage to potential breakage (Hardin, 1985).

4.2.2. Momentum conservation and dynamic action

The momentum equation is the expression between the macroscopic force and velocity of the landslide. The velocity is mainly affected by three forces: internal force, basal shear resistance and interphase force. The momentum equation is as follows:

$$\rho\left[\frac{\partial \boldsymbol{v}}{\partial t}+(\boldsymbol{v}\cdot\nabla)\boldsymbol{v}\right] = -\nabla \boldsymbol{p}+\mu\cdot\Delta \boldsymbol{v}+\rho g+f+R \tag{5}$$

where v is the velocity (m/s), ∇p is the pressure gradient, $(\boldsymbol{v}\cdot\nabla)$ is the scalar product of the velocity and Nabla operator, $\Delta \boldsymbol{v}$ is the Laplace operator for velocity, f is the resistance force of shear layer (N), R is the interphase force (N), g is the gravitational acceleration (m/s^2), and μ is the dynamic viscosity coefficient.

(1) Internal force. In the dynamic process, the flow regime is changeable, and mainly expresses as dense, dilute and ultra-dilute state (Fig. 12). The bottom of and the middle of the flow are dense, the surface is dilute grains, and the individual grains are ultra-dilute (Fig. 12). Three types of granular flow regimes can respectively be classified to inertial flow (collision force), shearing flow (shear force) and transition flow (collision force and shear force) (Bagnold, 1954; Jaeger et al., 1996; Pouliquen and Chevoir, 2002; Roux and Combe, 2002; MiDi, 2004).

(2) Basal resistance. In the beginning, the rock mass is in a relatively intact state. The basal shear resistance can be described by the Coulomb friction model, which mainly depends on the basal friction coefficient. When the moving

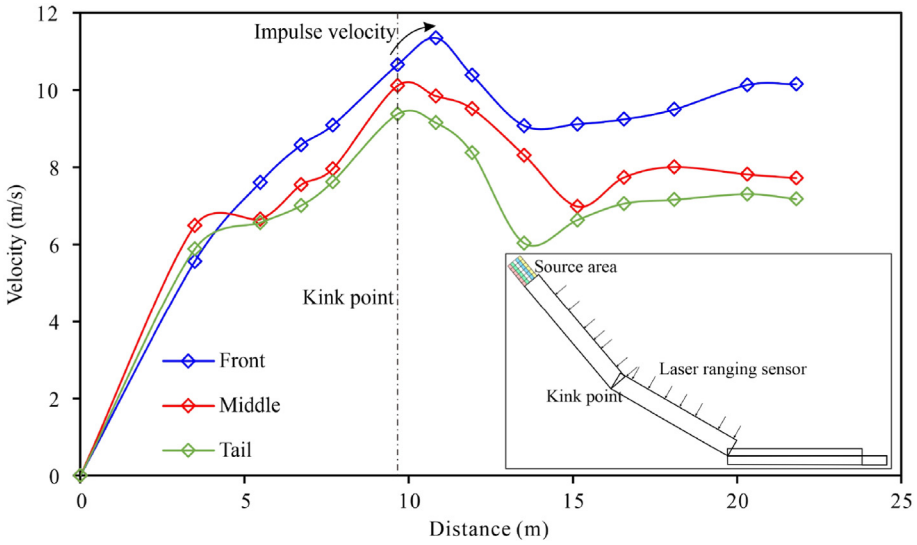

Fig. 18. Representative evolution processes of velocity. All of the experiments introduced in Fig. 16 have the same velocity trends verse distance. Taken F-1 as an example, the momentum transfer from the tail to the front leads to a strong impulse velocity in the front, while it decreases the velocity in the middle and tail when impacted at the kink point. Fourteen laser ranging sensors with certain interval (ΔL) are installed on the flume along the central line. The purpose of applying these sensors is to determine the block positions of the front, middle and tail, and to measure the differential travel time (Δt) between two successive sensors. In this way, the mean front, middle and tail velocities can then be calculated by $v = \Delta L/\Delta t$.

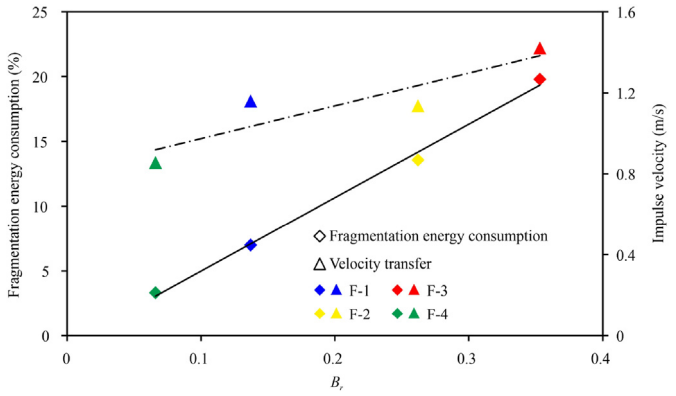

Fig. 19. Influences of fragmentation degree (B_r) with different structures on energy sink and velocity transfer. The fragmentation energy is assessed based on the comminution theory (Locat et al., 2006). The velocity transfer is determined as the impulse velocity as a result of momentum transfer as shown in Fig. 18.

mass enters the transition zone, the fragmentation breaks strongly the relatively intact rock mass into granular flow. The flow characteristics are shown in Fig. 13 in terms of Reynolds' number. Herein, the basal shear resistance seems to be controlled by the properties of the boundary layer. Using the Reynolds' number, the boundary layer can be regarded to be a laminar state or a turbulent state (Fig. 13), and the flow velocity is crucial to obtain the basal shear resistance. The undulating runout path and the covered erodible material on the runout path may cause separation of the boundary layer, and then the basal shear resistance disappears. The granular self-lubrication effect proposed by Campbell (1989) can be regarded as a special case for the separation of the boundary layer.

(3) Interphase force. The moving mass is composed of discrete solid grains, and the interstitial space of these grains is filled with air or water. In extreme conditions, such as heavy rainfall, glacial lake outburst, and ice/snow melting, the volume fraction of liquid is large enough to form a multiphase mixed flow. The interaction of liquids and solids could affect the movement and deposition (Stokes, 1851; Khan and Richardson, 1987; Iverson, 1997; Pudasaini, 2012; Lee and Huang, 2018; Gao et al., 2022a).

4.2.3. *Energy conservation and kinetic energy dissipation*

The energy conversion, transformation and dissipation of the high-altitude and long-runout rockslide are very complicated

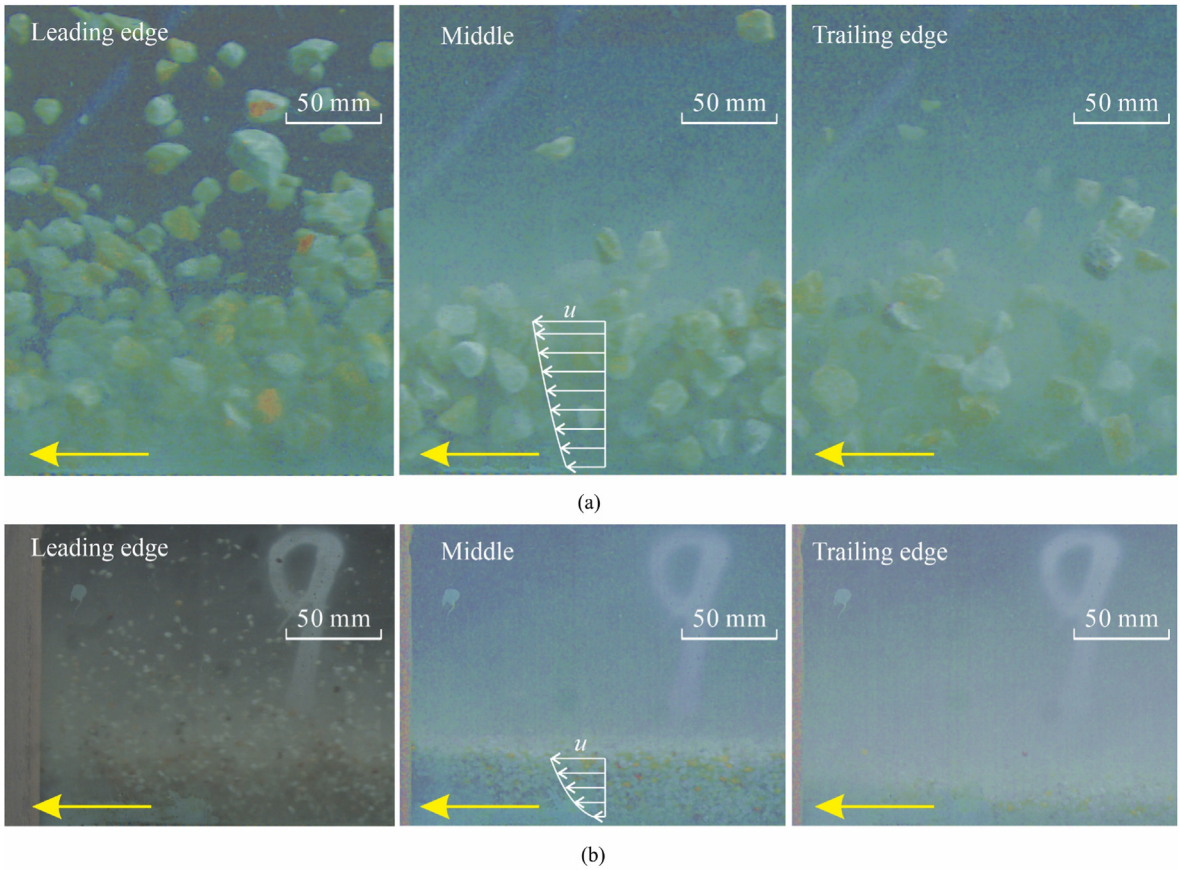

Fig. 20. Multiple images digitally generated showing position of granular flow over three images at leading edge, middle and trailing edge by high-speed camera with a frame rate of 2000 fps at a resolution of 1280 × 1024 pixel. In these experiments, the slopes of both flumes are adjusted as 40°. Angular quartz sands with different grain size: (a) 16–32 mm and (b) 2–4 mm are selected as granular materials, and each group contains a single grains size (monodisperse) with the quality of 1000 kg.

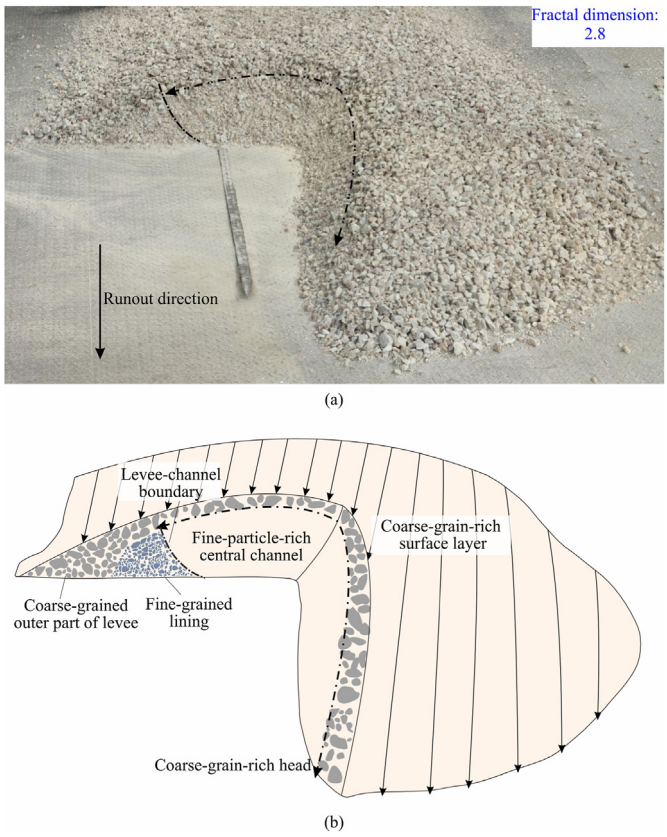

Fig. 21. Cutaway sketch showing deposit structure of polydisperse granular flow with the fractal dimension (D) of 2.8: (a) Deposition characteristics from experiment; and (b) Sketch diagram explaining deposition characteristics. The right front side of the deposits is removed by trowel carefully in order to understand their internal granular structures. In this experiment, the slopes of both flumes are adjusted as 40°. Angular quartz sands with four grains size ranges (2–4 mm, 4–8 mm, 8–16 mm, and 16–32 mm) are selected as granular materials, and each group contains aforementioned four grains sizes (polydisperse) controlled by $D = 2.8$ with a total mass of 1000 kg.

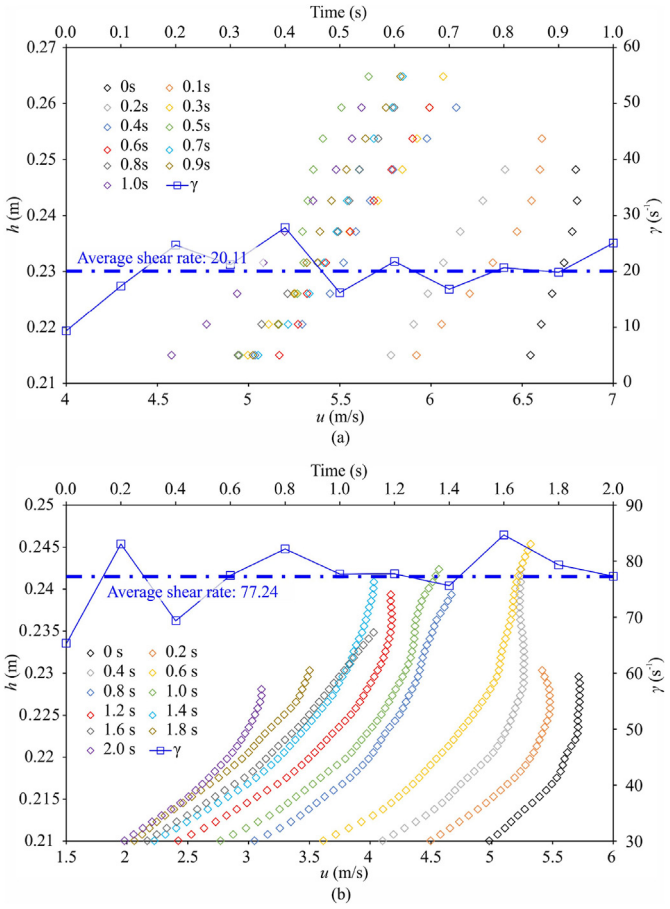

Fig. 22. Velocity profiles (u–h) and corresponding depth-averaged shear rates (γ-t) for different granular sizes: (a) 2–4 mm and (b) 16–32 mm. The velocity profiles of the granular flows are initially extracted every 0.0005 s by particle image velocimetry (PIV) analysis, and then averaged over 40 successive steps. The experimental conditions and visual flow characteristics of these analyses are illustrated in Fig. 20. PIV analysis ignores the dilute particulars at the leading and trailing edges and the surface of the flow at the middle. Time-averaged velocity profiles of the granular flows are plotted every 0.1 s (2–4 mm) and 0.2 s (16–32 mm) time interval from the leading edge to trailing edge, respectively. Time at 0 s represents the stating time of PIV analysis.

(Ellen and Fleming, 1987; Anderson and Sitar, 1995; Evans and DeGraff, 2002; Yang et al., 2018; Luo et al., 2019). The conservation theory based on the classical physics framework has been widely used in energy analysis (Locat et al., 2006; Pudasaini and Domnik, 2009).

The energy in the moving mass is mainly divided into three types: kinetic energy, potential energy and internal energy. The three types of energies transform each other, and finally dissipate in a form of internal energy (Bartelt et al., 2006; Pudasaini and Miller, 2013). The initial potential energy determines the total energy, and depends on the relative height difference: the larger the relative height difference, the greater the potential energy. The energy relationship and associated physical phenomenon in the moving mass is shown in Fig. 14, and can be described by

$$E_t = E_p + E_k + E_i \tag{6}$$

where E_t is the total energy, E_p is the potential energy, E_k is the kinetic energy, and E_i is the internal energy.

4.3. Large-scale physical experiments on high-altitude rockslides

4.3.1 Large-scale physical experiment apparatus

The dynamic process of high-altitude and long-runout rockslide is very complex. The physical experiments can be used to understand the influencing parameters and the development of real-time runout (Dufresne, 2012). Thereby, the physical

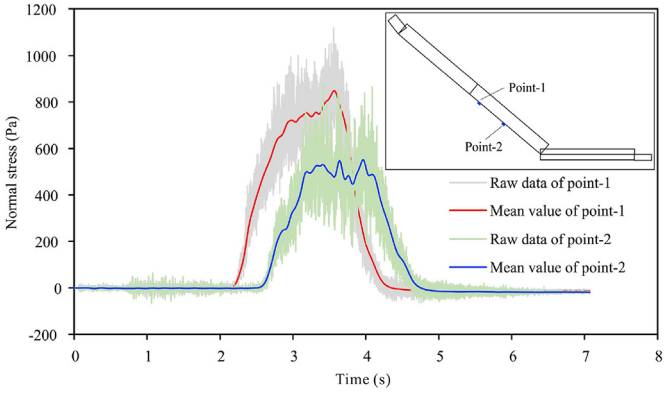

Fig. 23. Time evolution curves of the measured basal normal stress for the granular size of 2–4 mm. The experimental conditions in shown in Fig. 20. The raw normal forces are measured by self-made force plate, similar to Iverson (1997). The mean values are determined by applying a moving window average filter, and the window size is set as 0.04 s time interval.

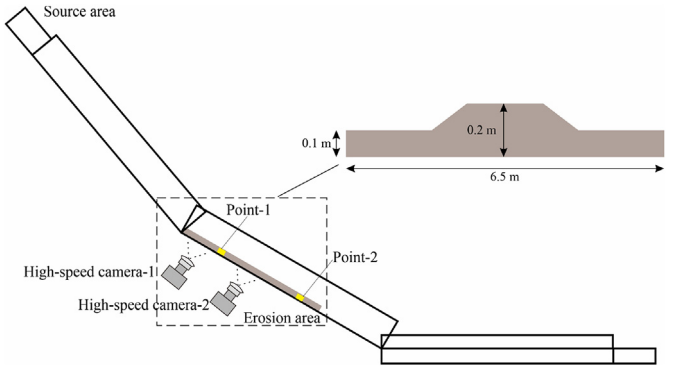

Fig. 24. Schematic diagram of experimental setup for researching the dynamic behaviors of substrate in the processes of erosion and entrainment. The slopes of two flumes during these experiments are adjusted as 50° and 30°, respectively. The high-speed camera has a frame rate of 2000 fps at a resolution of 1280 × 1024 pixel. There are two experimental situations: (1) dry substrate: angular quartz sands with size of 16–32 mm and 2–4 mm are selected as granular material in initiation zone and erosion area, respectively; (2) wet substrate: angular quartz sands with size of 16–32 mm are selected as granular material in initiation zone. As for erosion area, the granular material with three size ranges (0–2 mm, 2–4 mm, and 4–8 mm) are mixed with the fractal dimension of 3.3 and volumetric water content of 20%. Two pore-pressure sensors are arranged at point-1 and point-2 respectively for measuring basal pore-fluid pressure under experimental situation (2).

experiment has become one of the most effective means for studying the rockslide dynamics (Bowman et al., 2012; Dufresne, 2012; Manzella and Labiouse, 2013; Farin et al., 2014; Bartali et al., 2015; Sanvitale and Bowman, 2017; Li et al., 2021). However, the data obtained from physical experiment may not accurately describe field-scale behaviors due to scaling issue (Iverson et al., 2004; Bryant et al., 2015). Until now, the largest experiment apparatus for studying rockslide dynamics is a flume measuring of 90 m long and 2 m wide, which was developed in United States Geological Survey (USGS) (Iverson, 1997). This flume is excavated on the mountain with a constant slope of 30°. The opaque side edge of this flume does not capture the micro grain-scale flow.

In this study, considering the representative three-stage dynamic processes, i.e. initiation, transition, and deposition, we designed a large-scale experimental apparatus with transparent side flume walls, allowing observations of internal grain-scale phenomena. As shown in Fig. 15, this apparatus is mainly composed of a hopper (maximum value of about 5 m^3), two flumes (length × width × height = 11 m × 1.2 m × 1.5 m), and a platform (length × width = 12 m × 4.8 m). The side walls of these two flumes are transparent tempered glass, and the slope of these flumes is controlled by the hydraulic control system within the ranges of 30°–40° and 40°–50°, respectively (Fig. 15b).

4.3.2. Fragmentation effect on dynamic behaviors of rockslides

Fragmentation is a very common phenomenon in the dynamic process of high-altitude and long-runout rockslides, which makes the original block structure transform into granular structure. In the fragmentation process of rockslides, the relatively intact rock mass in the initiation zone is broken into numerous fragments with different sizes, which is associated with the energy conversion and the runout fluidization (Davies et al., 1999; Hungr and Evans, 2004). The fragmentation effect on the rockslides with different block structures is a challenging issue, especially the effect on velocity, energy and momentum (Haug et al., 2016; Gao et al., 2022a).

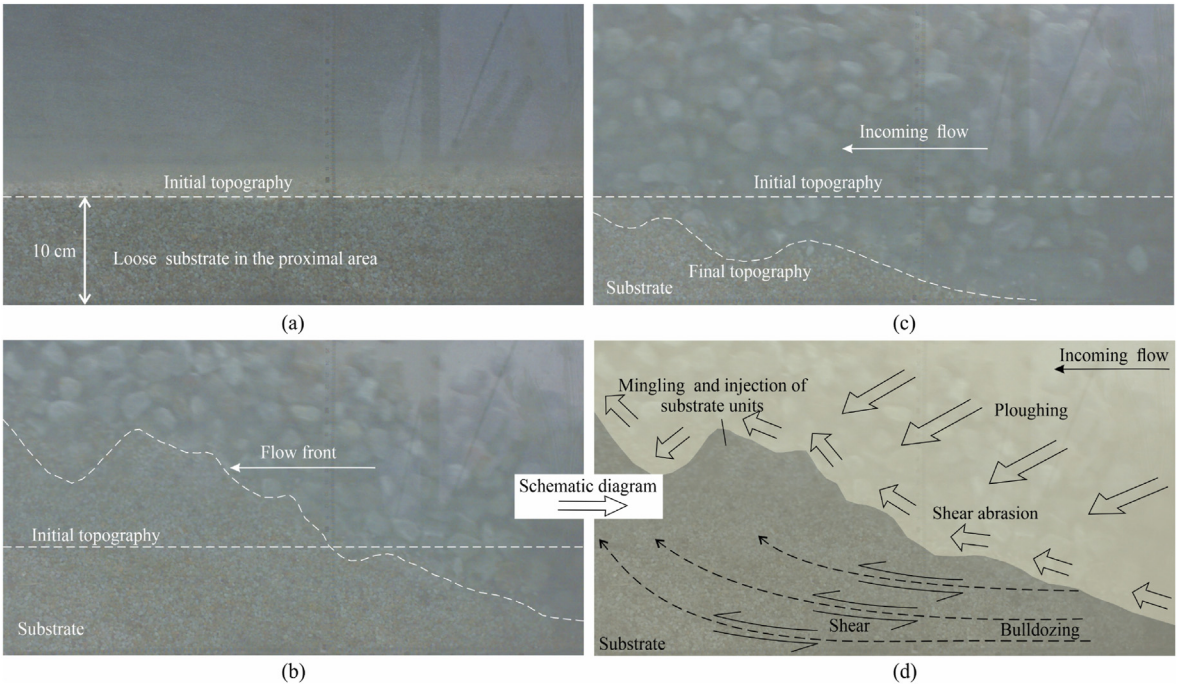

Fig. 25. Dynamic evolution sequence of loose substrate in the proximal captured by high-speed camera-1 under experimental situation (1): (a) Initial state; (b) Interaction process between the granular flow and substrate; (c) Final state; and (d) The interaction process between granular flow and substrate.

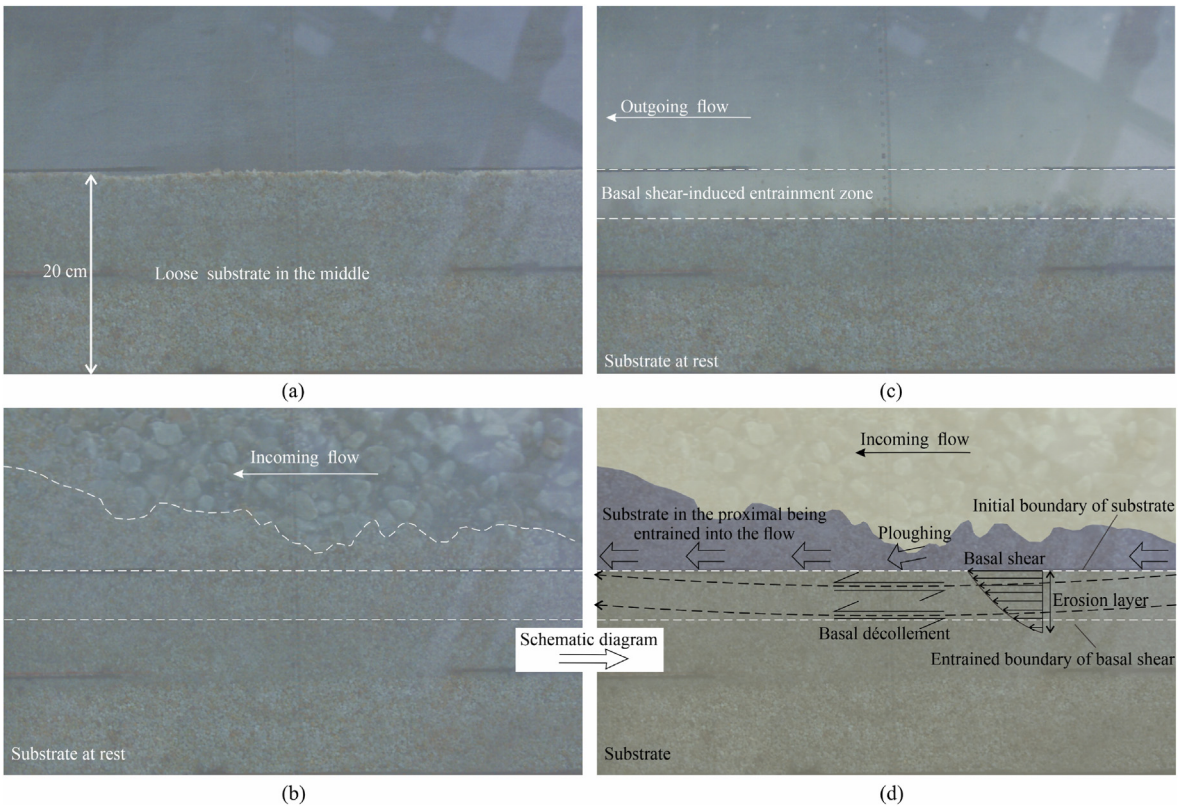

Fig. 26. Dynamic evolution sequence of loose substrate in the distal captured by high-speed camera-2 under experimental situation (1): (a) Initial state; (b) Mobilized process; (c) final state; and (d) The mobilized process of substrate.

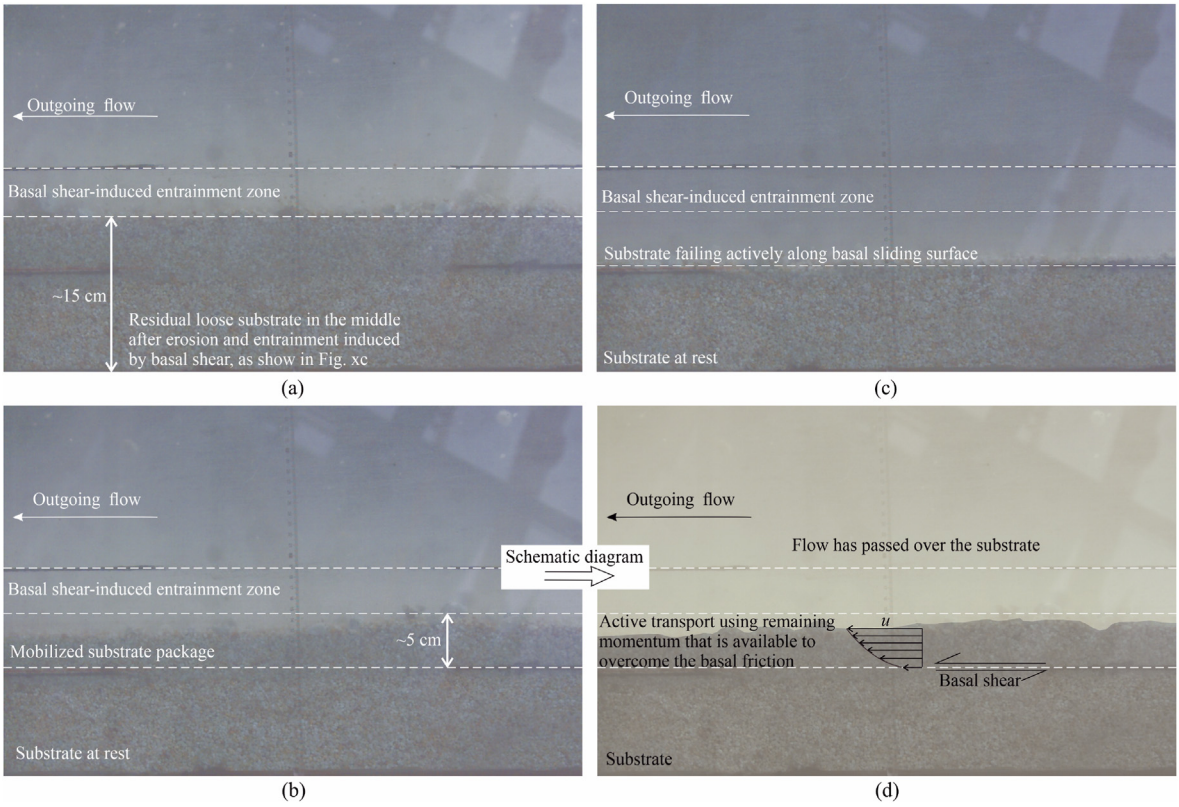

Fig. 27. Dynamic evolution sequence of shear-induced mobilized loose substrate package after the erosion process in Fig. 26 captured by high-speed camera-2 under experimental situation (1): (a) Initial state; (b) Mobilized process; (c) Final state; and (d) The mobilized process of substrate.

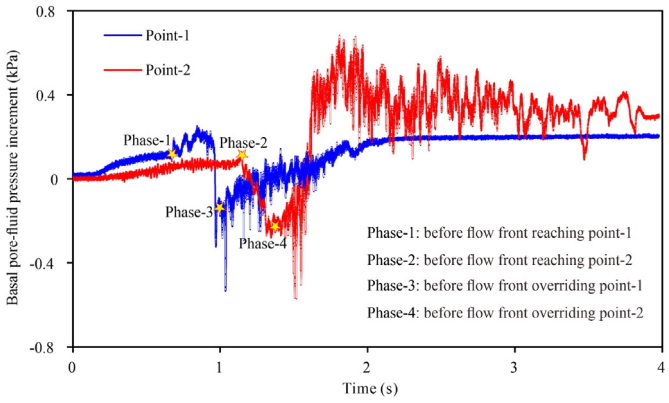

Fig. 28. Dynamic evolution processes of basal pore-fluid pressures at different measuring points under experimental situation (2).

Fig. 16 presents the deposition characteristics for different block structures after fragmentation. In general, extremely crushed fine grains are concentrated at the rear of the horizontal plane and the bottom of the deposits, which are formed by the intensive friction of fragments on the horizontal plane. In addition to these fine grains, the main bodies in the upper part show more marked fragmentations in the distal, which is closely associated with the intensive fragmentation coming from the impact at the front and bottom parts (Zhao et al., 2018). The fragmentation characteristics are closely associated with the blocking structures in initiation zone. With decrease of subblock strength, more fine fragments can be observed, implying a more significant fragmentation degree (Figs. 16 and 17). As shown in Fig. 16c, there is almost no crushing for higher strength subblocks, and only the disintegration between the joint surfaces is observed. In addition, with increase of joint density, the fragmentation degree is gradually increased, and many crushed fine clastic grains are formed (Figs. 16d and 17).

The disintegration of joints and fracture of subblocks can lead to transformation and redistribution of the momentum. As shown in Fig. 18, since the momentum transfer enables to force the front part to gain momentum when impacted at the kink point, the boosting impulse velocity in the front and the decreasing velocity in the middle and tail are observed. Fig. 19 presents the relationship between the fragmentation degree described by relative breakage ratio (B_r) and impulse velocity. The fragmentation degree is positively correlated with the impulse velocity, suggesting that the fragmentation enhances the momentum transfer efficiency. On the other hand, in view of energy, we can assess the dissipation of energy associated with fragmentation. As shown in Fig. 19, fragmentation energy consumption accounts for 3%–20% of the total energy, which is consistent with the field investigations (Locat et al., 2006). This energy sink is caused by the generation of new fragment surfaces, and it is more significant when the fragmentation degree increases. These results further prove that the fragmentation can cause energy consumption, which is conductive to the momentum transfer of blocks and thus increase the runout of the front part.

4.3.3 Dynamic behaviors of dry granular flow

The long-runout rockslides commonly transform into a rapid granular flow of debris with intensive fragmentation (Davies and McSaveney, 2009), and thereby understanding the rheological

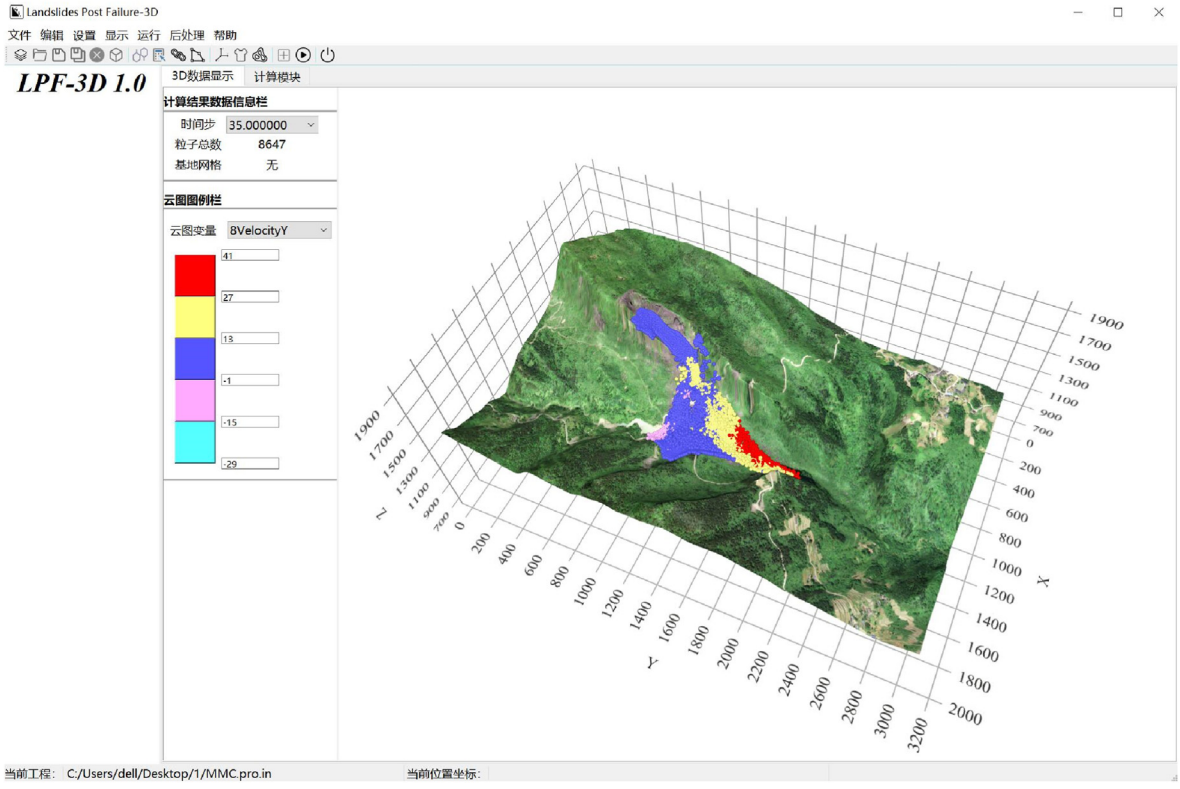

Fig. 29. LPF^{3D} interface.

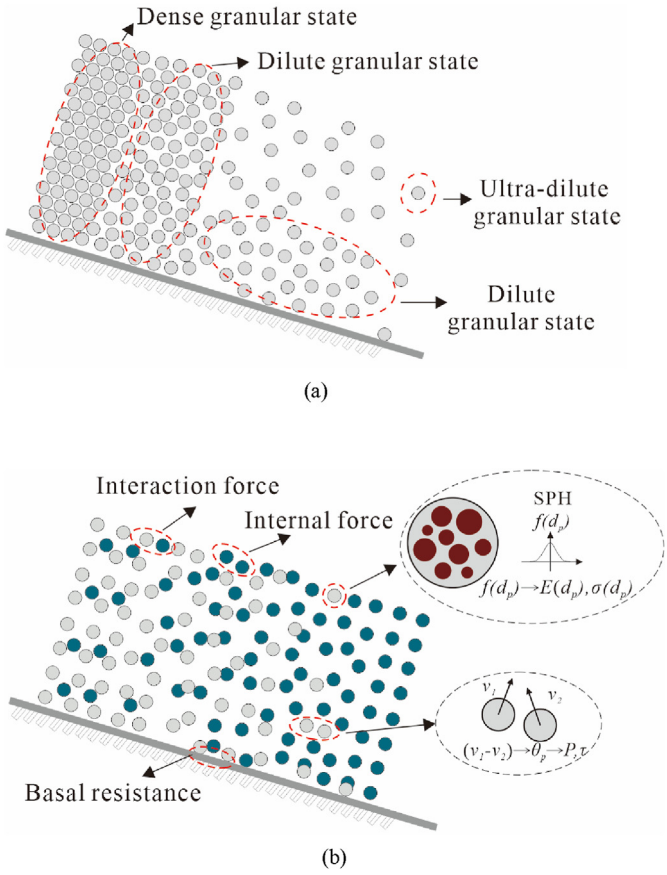

Fig. 30. Multiple-phase simulation principle of high-altitude and long-runout rockslide: (a) Sketch of the dense, dilute and ultra-dilute states in the motion of a cohesionless dry solid grains, with different state stress solutions applied to different constitutive models; and (b) Sketch of the action of internal forces, interphase forces and substrate resistance in the simulation of rockslide motion.

behaviors of granular flow and linking the behaviors to rockslide runout are likely to provide insights into the underlying rockslide mechanisms (Campbell, 1990; Zhou and Sun, 2013).

At the microscale, the flow regime of granular flow can be classified into dense regime, dilute regime and ultra-dilute regime (Fig. 12). As shown in Fig. 20, granular flows mainly consist of dilute (or ultra-dilute), saltating and dispersed grains with low solid concentration observed at both the leading and trailing edges. The grains at the middle are almost densely packed with high solid concentration. However, in the case of larger granular size (Fig. 20a), the dilute, saltating and dispersed grains are also observed on the surface of the flow at the middle. According to the flow characteristics in Fig. 20, grains in the leading and trailing edges are mainly influenced by inertia collision, and frictional contact dominates the granular interaction in the middle of the flow, whereas the increasing size tends to increase granular inertia as reflected by more disperse grains in Fig. 20a.

In the outcrops of rockslide deposit, inverse grading is very common, meaning that vertical directionally aligned grains decrease in size from the surface to the bottom (Cruden and Hungr, 1986; Zhang et al., 2016). In general, when granular flows with bidisperse or polydisperse granular structures downslope, the granular segregate develops an inversely graded granular size distribution, i.e. upward coarsening (Johnson et al., 2012; Sheng et al., 2021). As shown in Fig. 21, coarse grains are not only enriched in the surface layer, forming a special granular deposit sequence similar to the "Brazil Nut Effect" (Möbius et al., 2001), but the lobate heads are also dominated by coarse grains, behind which it is less well sorted and finer grains deposit between coarse-grain levees. The formation of such a deposit structure involves very complex granular dynamics. Coarse grains segregate to the flow surface layer, transport to the flow snout by differential shear, and then are shouldered aside by advancing fine grains (Johnson et al., 2012; Kokelaar et al., 2014). Therefore, the granular mixture continually forms a conduit boundary constrained by coarse-grained levees and fine-grained lining, and a central low-frictional shear layer by fine-grained channel, which reduces frictional energy losses and thus enhances the mobility of granular flow.

The rheological mechanical behavior of granular flow can be reflected in the shape of velocity profile (Lanzoni et al., 2017). The granular flow involved in the majority of grains in high-altitude and long-runout rockslide exhibits the characteristics of dense flow with the occurrence of differential shear within the grains (Zhang et al., 2016, 2020a, 2022). As shown in Fig. 22, the flow velocity of granular flow with different sizes decreases gradually from the leading edge to trailing edge along the flow direction, and shows a slip velocity. The decrease in granular size makes the velocity profile to change from nearly linear to concave, and enlarges the shear rate. Taking the finer grains with apparent shear rate as an example (Fig. 22b), the velocity enhances gradually from the bottom to the surface. In addition, with the continuous acceleration of granular flow, the basal normal stress decreases simultaneously (Fig. 23), which is inferred to increase agitation (lower solid concentration) closely associated with intensive shear in the lower part (Campbell, 1989). This implies a possible mechanism to extreme mobility of landslide as a decrease in basal normal stress indicates a decrease in resistance.

4.3.4. Dynamic behavior of erosion and entrainment process

When granular flow rapidly spreads over the complex terrain covered with loose substrate, the substrate will inevitably be eroded and then entrained into the flow, which dramatically enlarges the flow volume and changes the flow mobilization (Dufresne, 2012). This study investigates the dynamic behaviors of erosion and entrainment process of substrate imposed by the overlying flow (Fig. 24). Our experiments indicate that the process of erosion and entrainment of the granular flow takes place upon plough, basal shear, substrate active mobilization and continuous impact ahead of the flow.

As shown in Fig. 25, when the front of the flow encounters the proximal substrate, the substrate is eroded in a form of significant ploughing, accompanied by shear abrasion. Here, intensive compress-related shear at the beneath and ahead of the granular flow forces the substrate to be entrained and bulldozed to the front. In the distal (Fig. 26), the underlying substrate is subjected to shear-induced erosion imposed by the advancing flow, and then forms a differential shear erosion layer within a certain range below the substrate. The erosion layer is observed to be entrained grain by grain rather than mass, and the availability of entrainment depends on the momentum gained by substrate. In addition, after the erosion process of Fig. 26, a mobilized substrate package is developed with a thick of 5 cm (Fig. 27). The active mobilization of this package is sliding later by layer until the residual momentum of substrate fails to motivate. Furthermore, in the process of interaction between landslide and substrate, a deformation wave ahead of the flow under continuous impact-related erosion can improve erosion of substrate (Estep and Dufek, 2012; Zhang et al., 2020a). As shown in phase-1 and phase-2 in Fig. 28, the increments of the basal pore-fluid pressures ahead of the flow front are observed at two measuring points as a result of substrate compression,

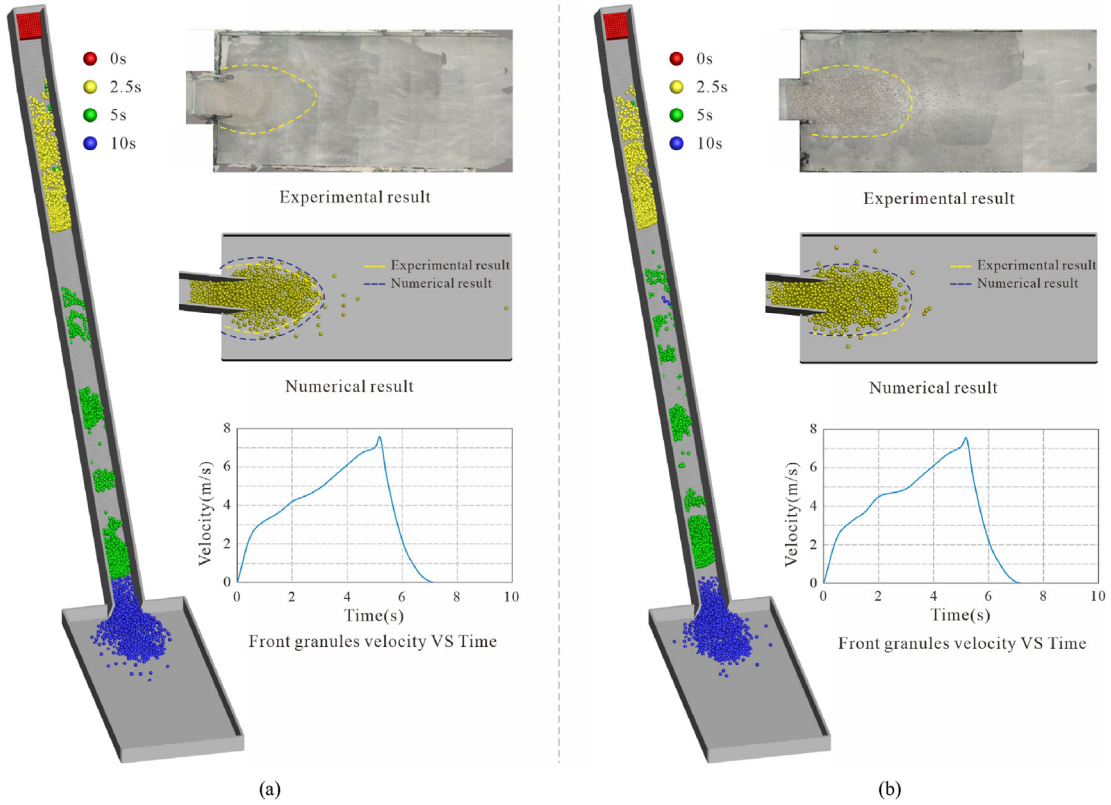

Fig. 31. Comparison between experimental results and numerical results of the flume experiment with cohesionless grains of size (a) 3 mm and (b) 24 mm.

mobilization, and transport, which can be used as a proxy to reflect the effect of impact-related erosion (Iverson et al., 2011). This effect is essentially inconsistent with phase-3 and phase-4 with respect to the increasing mechanisms of pore-fluid pressure (Yin et al., 2016).

4.4. Computational theory and numerical analysis of long-runout chain-style dynamic processes

4.4.1. LPF^{3D}

The high-altitude and long-runout rockslides move rapidly, while the runout/dynamic process is hard to capture in field. To quantitatively assess the impacting scope and disaster risk, numerical simulation has become one of the most efficient and visualized means to analyze the movement process and dynamics mechanism of landslides (McDougall and Hungr, 2004; Christen et al., 2010; Ouyang et al., 2013; Feng et al., 2014; Xu and Dong, 2021; Gao et al., 2022c). The Landslide Post-failure in Three Dimensions (LPF^{3D}) has established a new numerical simulation approach for solving the polymorphic transformation of moving mass among dense, dilute and ultra-dilute granular flow, and the multi-media coupling of fluid and solid grains (Fig. 29). This method does not require a meshing, and is more computationally efficient than the discrete element method. It can realize the high efficiency and high precision solution of complex dynamic problems of rockslides, debris avalanches and two-phase flow.

This method bridges the continuum algorithm and discrete medium algorithm, based on complex particle flow continuum theory model and smooth particle hydrodynamics method. From the perspective of particle dynamics, the smoothed particle hydrodynamics (SPH) method is used for discrete solution. Each individual particle carries not only the information such as mass, velocity, position and pressure of the particle phase, but also the particle size distribution shape, volume fraction and pseudo-temperature introduced by particle dynamics. The mass of SPH particles is equal to the total mass of particle swarm it represents, the density is the effective density of the particle swarm, the velocity is the mean velocity of the particle swarm, and the pseudo-temperature and pressure are the mean pseudo-temperature and mean pressure of the particle swarm. The actual number of particles can be calculated with a smaller number of particles by the volume fraction, and the volume fraction is also an important indicator to discriminate the dense, dilute and ultra-dilute states of particles. The internal force, boundary friction resistance and interphase force in the process of rockslide movement are fully considered (Fig. 30).

4.4.2. Numerical analysis of flume experiment

(1) Runout simulation of monodisperse granular flow

Based on the polymorphic transformation theory, two monodisperse granular flows with different particle sizes are simulated using LPF^{3D}. According to the flume experiment, the grains sizes of the slide body material are 3 mm and 24 mm in the numerical simulation, and the physical and mechanical parameters of the sliding body are consistent with those in the flume experiment. The values of volume fraction are 60% (dense and dilute states) and 2% (dilute and ultra-dilute states).

Fig. 31 shows the numerical simulation of the moving material with granular sizes of 3 mm and 24 mm LPF^{3D} can be efficiently realized using fewer computational particles to simulate massive grains. According to the analysis of the flume experiment results,

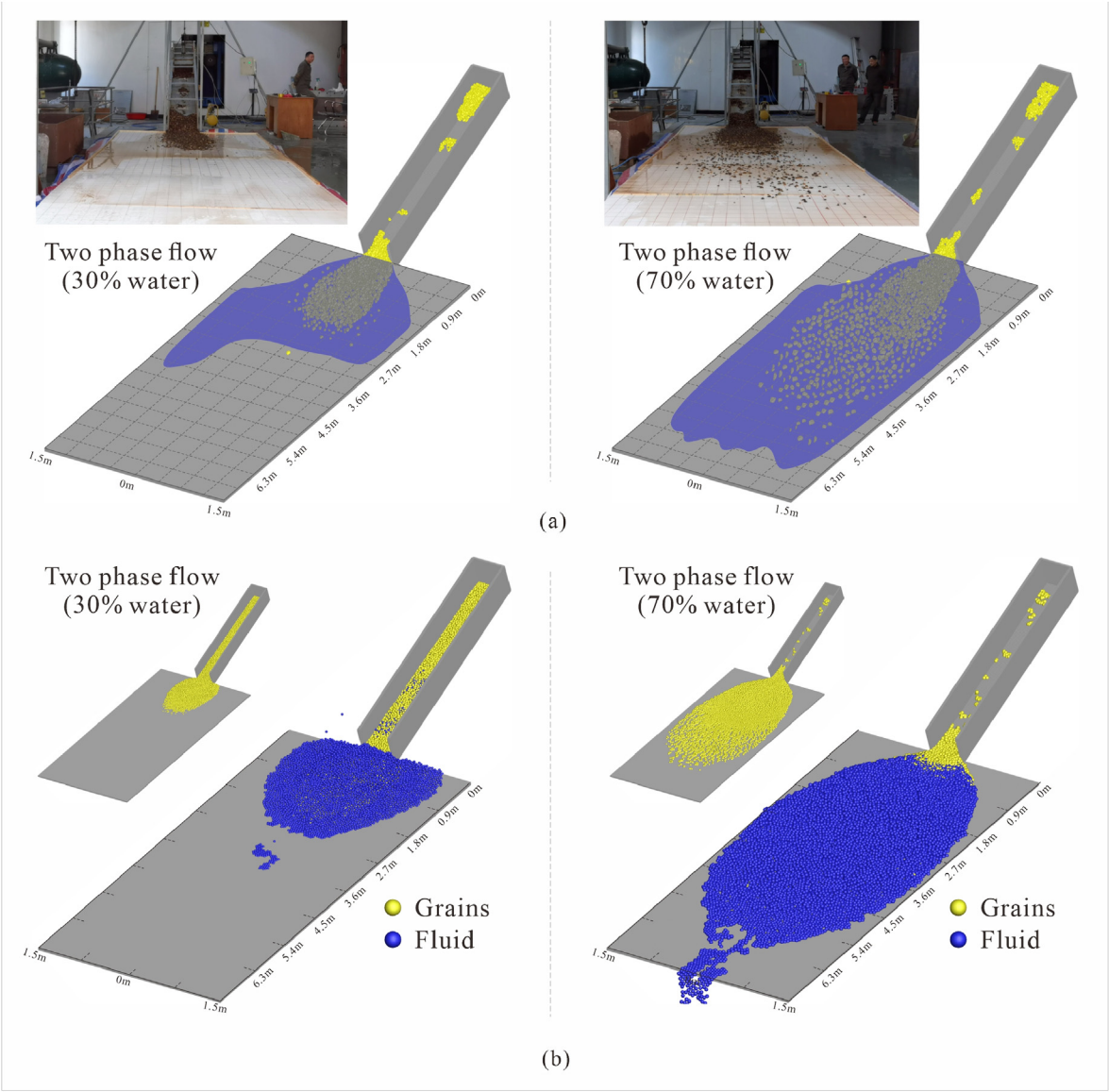

Fig. 32. Comparison between two-phase flow sliding results of flume experiment and LPF^{3D} numerical simulation in conditions i and ii. (a) The results of the flume experiment with 30% and 70% water by volume; and (b) The results of the LPF^{3D} numerical simulation with 30% and 70% water by volume.

the difference between the experimental and numerical results can be compared. By adjusting the parameters of the SPH algorithm using trial-and-error method, the motion processes and accumulation morphology are basically consistent, which provides a good verification and comparison for the actual landslide simulation and the parameter determination of the software algorithm. The total movement time of numerical simulation is 10 s, as displayed in Fig. 31. The numerical simulations of the maximum velocity, accumulation morphology and motion time are basically consistent with the experimental observations, indicating that the polymorphic transformation theory has a good applicability for the motion simulation of dry grains in the flume experiments, while the convergence and stability of the computational process are well captured (Fig. 31).

(2) Coupling simulation of solid grains-fluid

In addition to the equations of mixture theory (Bedford and Drumheller, 1983), the flume experiments provide data for studying the two-phase flow. The LPF^{3D} can simulate the mixed moving process of the two-phase flow. The main purpose of the experiment is to analyze the transformation of single-phase to two-phase flow. According to the test results, considering the influence of fluid drag force, the dynamic process of debris flow under four different conditions in the fluid-solid coupling flume experiment is simulated: (i) 30% water mixed with debris; (ii) 70% water mixed with debris; (iii) 30% slurry (water and clay mixture material with a viscosity coefficient is 0.018 Pa s) mixed with debris; and (iv) 70% slurry mixed with debris. The parameters are selected according to the field physico-mechanical parameters.

Fig. 32 shows the comparison between the simulation and experimental results in conditions (i) and (ii). It shows that for condition (i), most of the mixtures move and accumulate on the bottom plate, with a movement distance of about 2.2 m (Fig. 32a); for condition (ii), most of the mixtures move and accumulate on the bottom plate, with a movement distance of about 5.6 m (Fig. 32b). In the flume experiment, the pore water pressure was monitored.

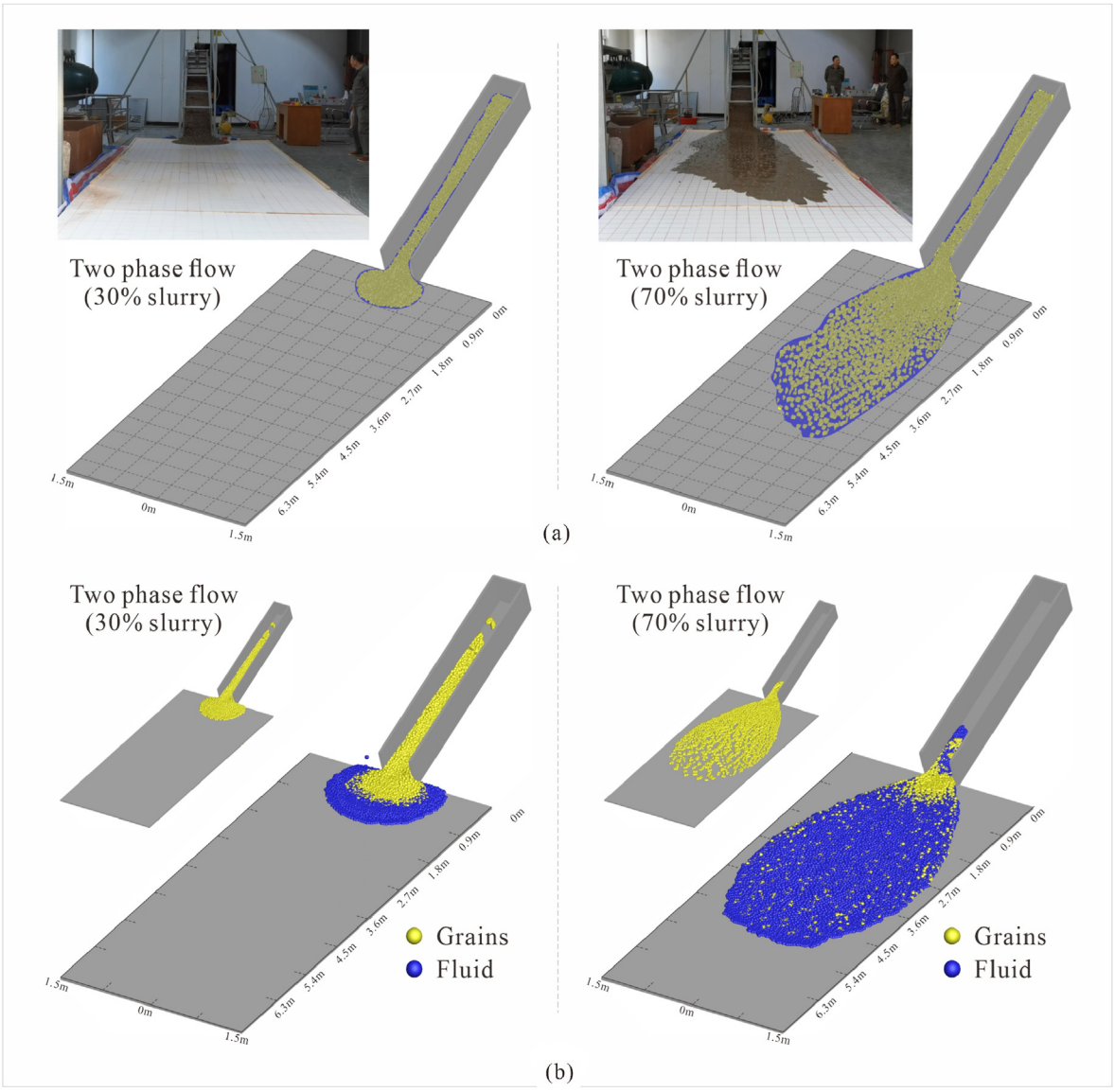

Fig. 33. Comparison between two-phase flow sliding results of flume experiment and LPF^{3D} numerical simulation in conditions (iii) and (iv): (a) The results of the flume experiment with 30% and 70% slurry by volume; and (b) The results of the LPF^{3D} numerical simulation with 30% and 70% slurry by volume.

When the fluid is under dilute state, the pore water pressure dissipates quickly with small pore pressure coefficient. As such cases, the separation of water and grain is not obvious, and the long-runout movement can be formed. This means that the fluid has a sound dragging effect on the solid grains. In the simulation, the influence of the encountering force is fully considered, and the simulation results match the test results very well.

Fig. 33 shows the comparison between the simulation and the experimental results in conditions (iii) and (iv). Under condition (iii), most the mixtures are in the state of movement, and finally stop and move at the slope toe. The grains are evenly distributed in the flume and at the slope toe, with a movement distance about 0.7 m (Fig. 33a). Under condition (iv), the state of the mixture is similar to that of condition (iii), but the movement distance is longer, and at the slope toe, with a movement distance about 5.4 m (Fig. 33b). In Fig. 32, the liquefaction effect of slurry is more obvious than that of pure water, and the pore pressure dissipates slowly, resulting in lower boundary friction resistance. The pore water pressure coefficient and the interphase force jointly affect the landslide movement, and the simulation results are also consistent with the actual results.

It also shows that the total motion time and distance of the simulation results are basically consistent with that of the flume experiment, and reflect a good applicability of the numerical calculation.

4.4.3. Numerical analysis of rockslide cases

Based on the theory of polymorphic transformation and multi-media coupling, the LPF^{3D} is used to simulate some typical landslides. The Jiweishan debris avalanche in Chongqing, and the Sanxicun rock avalanche in Sichuan Province, China are selected as the typical cases. The simulations are consistent with the actual deposit morphology (see Figs. 34 and 36), demonstrating the key influence of coupled interaction forces in the rockslide to debris flow transformation.

(1) Jiweishan debris avalanche

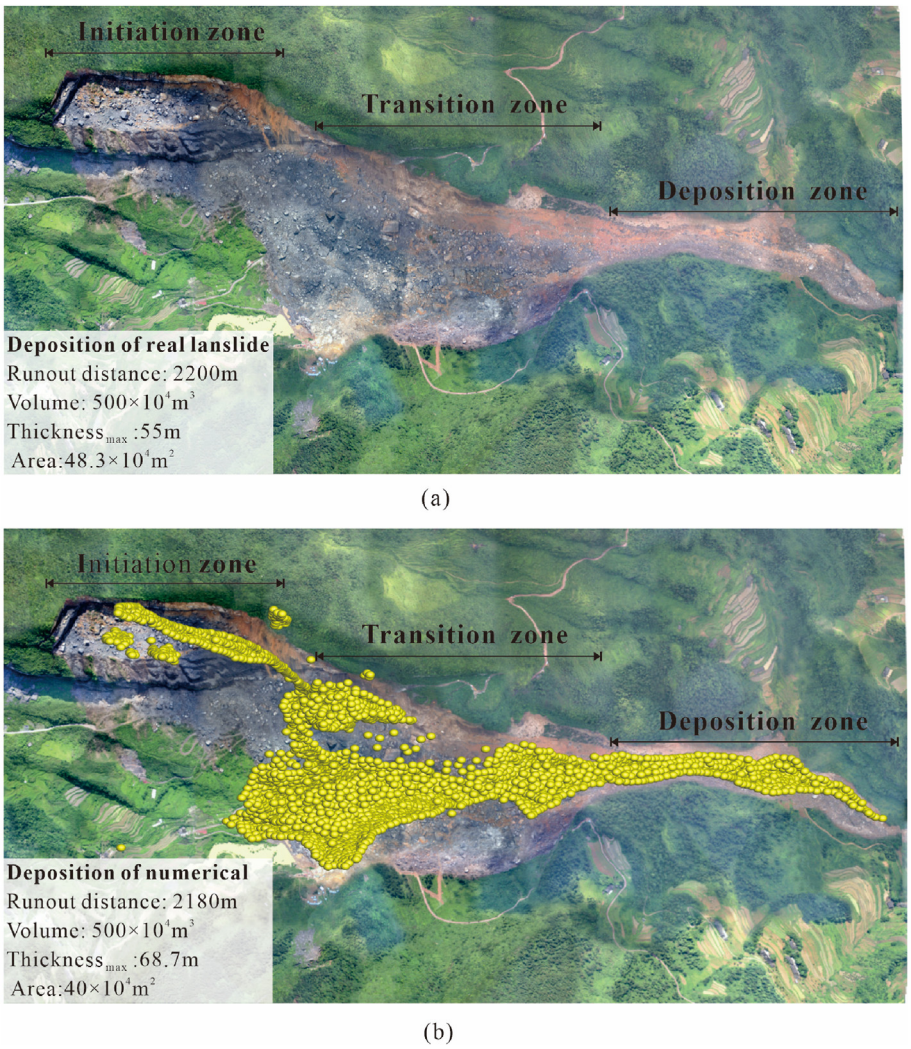

Fig. 34. Comparison between the actual rockslide accumulation results and numerical simulation results: (a) Remote sensing of debris avalanche accumulation; and (b) LPF^{3D} numerical simulation results.

On 5 June 2009, a landslide with value of about 500 × 10^4 m^3 sheared out from the initiation zone in the direction of apparent dip in Tiekuang town, Wulong County, Chongqing. This eventually formed an accumulation body with average thickness of over 30 m, a longitudinal length of approximately 2200 m and a total volume of approximately 700 × 10^4 m^3, resulting in 74 deaths and 8 injuries (Yin et al., 2011; Feng et al., 2016; Zhu et al., 2018). The rock mass of the Jiweishan debris avalanche is a single-phase dry granular flow, and reflects transformation of dense, dilute, and ultra-dilute granular flow. The actual parameters of main sliding body were used in the simulation (Zou et al., 2017; Gao et al., 2018; Zhang et al., 2018) and the critical values for the dense and dilute states were set at 60% and 2%, respectively.

The movement process of the Jiweishan debris avalanche is simulated using LPF^{3D}, and the red dashed line showed the actual rockslide accumulation. The average maximum velocity of the slide is approximately 40 m/s, and the maximum velocity of individual particles at the leading edge of the slide can reach 50.9 m/s. The movement process reflects the whole process of initiation sliding, potential kinetic energy transition, and debris accumulation (Fig. 35). The maximum distance of the rockslide movement is 2180 m, and the maximum accumulation thickness is 68.7 m below the shear outlet. The accumulated thickness decreases gradually from the back edge to the front edge, and the accumulation state is basically the same as the real rockslide, which is a good reproduction of the rockslide movement accumulation process (see Fig. 34).

(2) Sanxicun rockslide-debris flow

In July 2013, a rockslide occurred in Dujiangyan, Sichuan Province, China, leading to 166 deaths and destroying of 11 houses. The landslide movement distance was about 1200 m with a volume of 30 × 10^4 m^3 (Yin et al., 2016; Gao et al., 2017). The rockslide was destabilized and sheared out at a high altitude triggered by heavy rainfall. After the potential and kinetic energy conversion, the slide converged with the surface runoff, causing a large rockslide-debris flow. In the LPF^{3D} simulation, the fluid volume fraction and the solid grains volume fraction are summed to 100%. The initial volume fractions of the solid grains and fluid in the Sanxicun rockslide-debris flow are respectively set to 30% and 60% in the simulation.

In the LPF^{3D}, the dynamic process of Sanxicun rockslide-debris flow is revealed, and the red dotted line is the real rockslide deposit range. The maximum velocity at the front edge of the rockslide can reach 45 m/s, and the overall average maximum velocity of the moving mass is about 28 m/s. The maximum horizontal

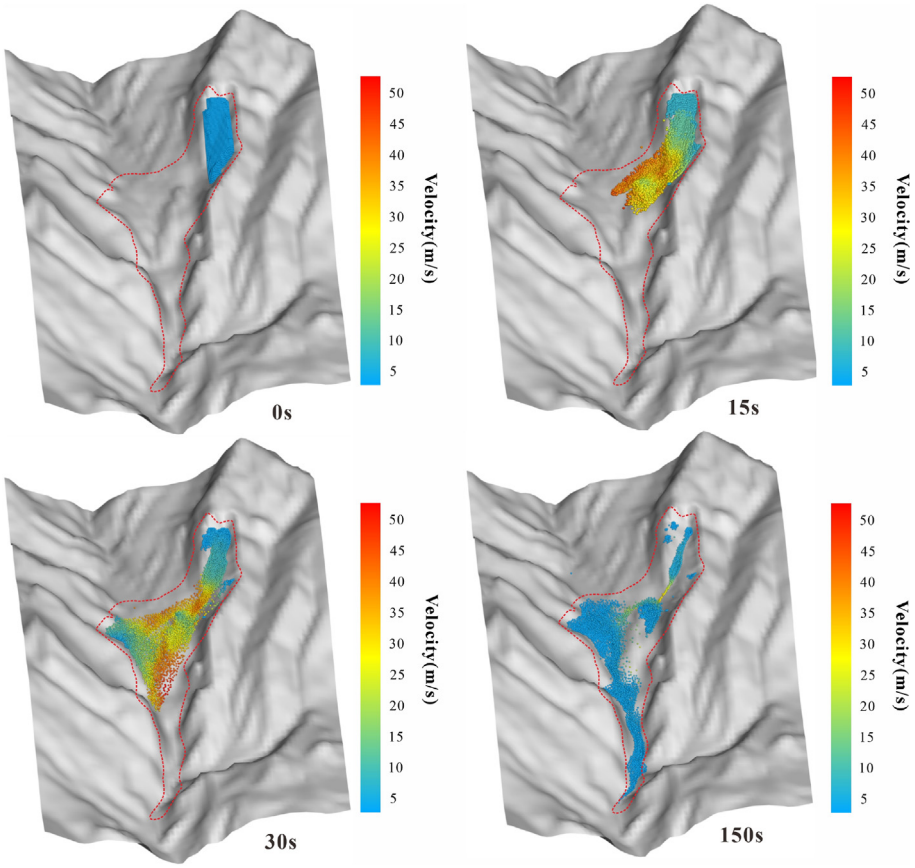

Fig. 35. The velocity distribution during the movement of the Jiweishan rockslide-debris avalanche.

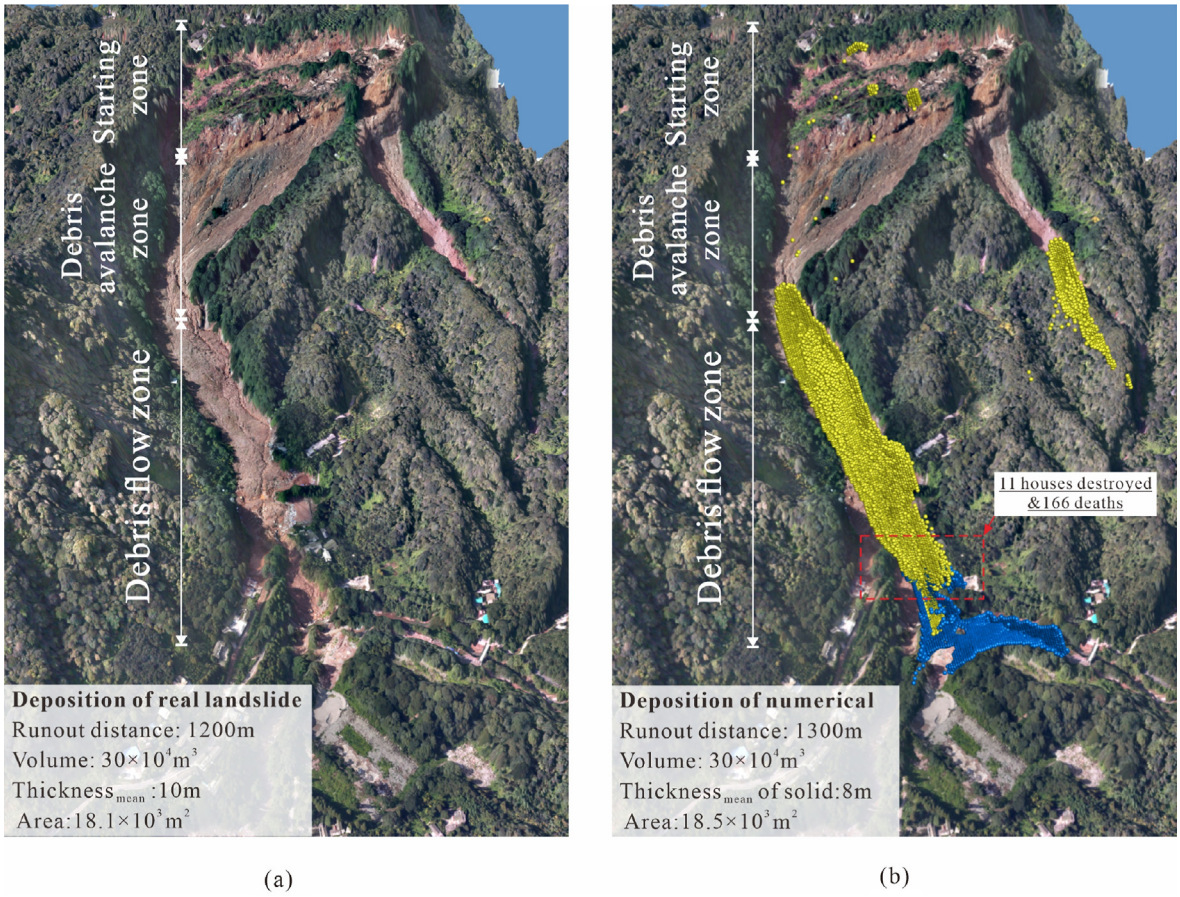

Fig. 36. Comparison between the actual rockslide accumulation results and numerical simulation results: (a) Remote sensing image of real landslide; and (b) LPF^{3D} numerical simulation results.

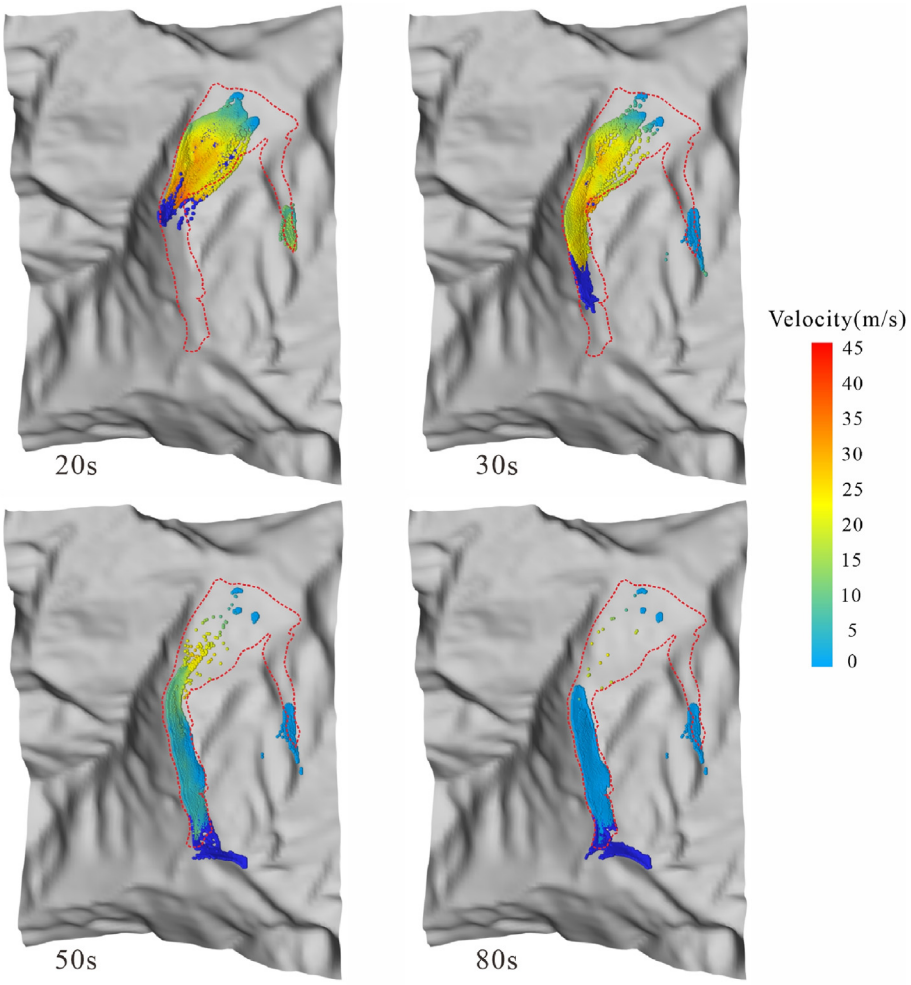

Fig. 37. Velocity distribution map of the Sanxicun rockslide-debris flow during movement process (Dark blue particles represent the fluid body).

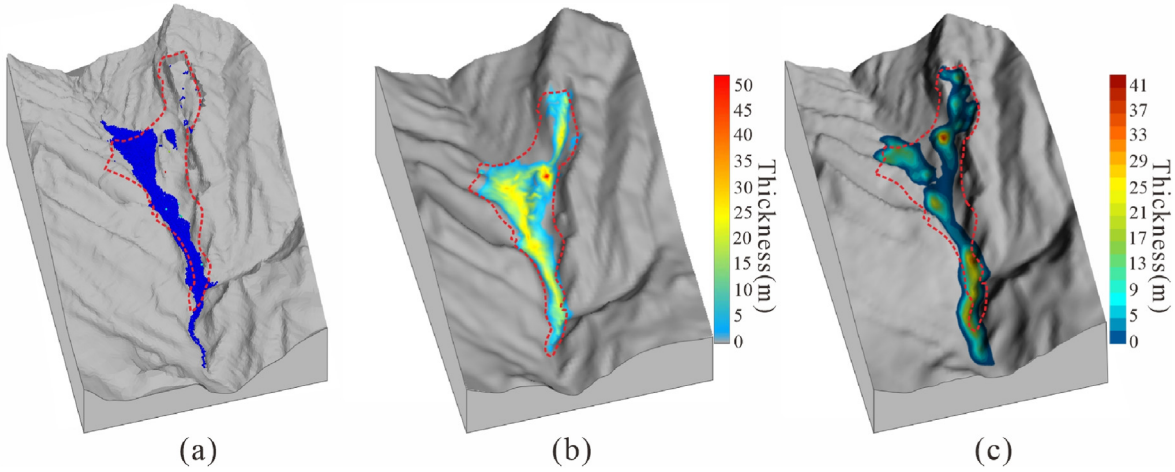

Fig. 38. The simulation results of the Jiweishan rockslide using different numerical models: (a) PFC^{3D} model; (b) LPF^{3D} model; and (c) DAN^{3D} model.

runout distance is 1300 m. The maximum deposit thickness is 11 m, and the overall average thickness of the solid phase is about 8 m (Fig. 37). The deposit feature is basically the same as the field rockslide (Fig. 36).

4.4.4. Comparison of different numerical analysis methods

In this study, the granular flow theory (particle flow code, PFC^{3D}) and the equivalent fluid theory (dynamic analysis of landslides, DAN^{3D}) are selected for the comparative analysis of the Jiweishan

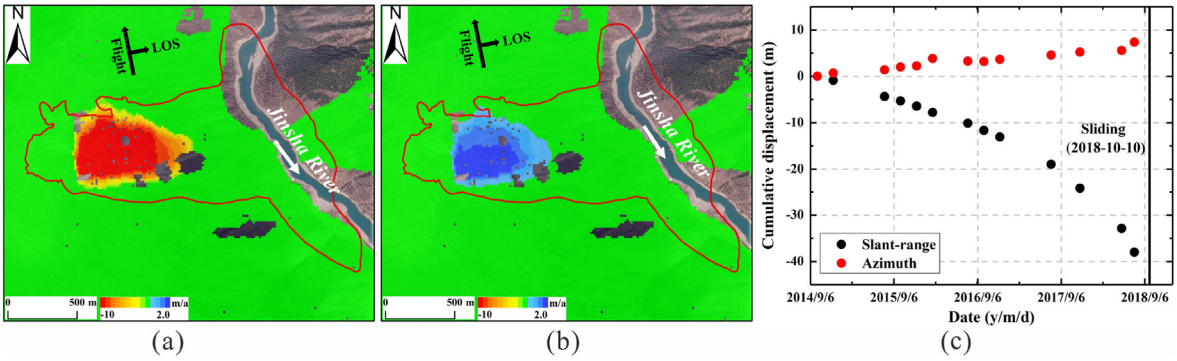

Fig. 39. The SAR displacement of the Baige rockslide (October 2014 to August 2018): (a) Slant-range; (b) Azimuth; and (c) Accumulative curve.

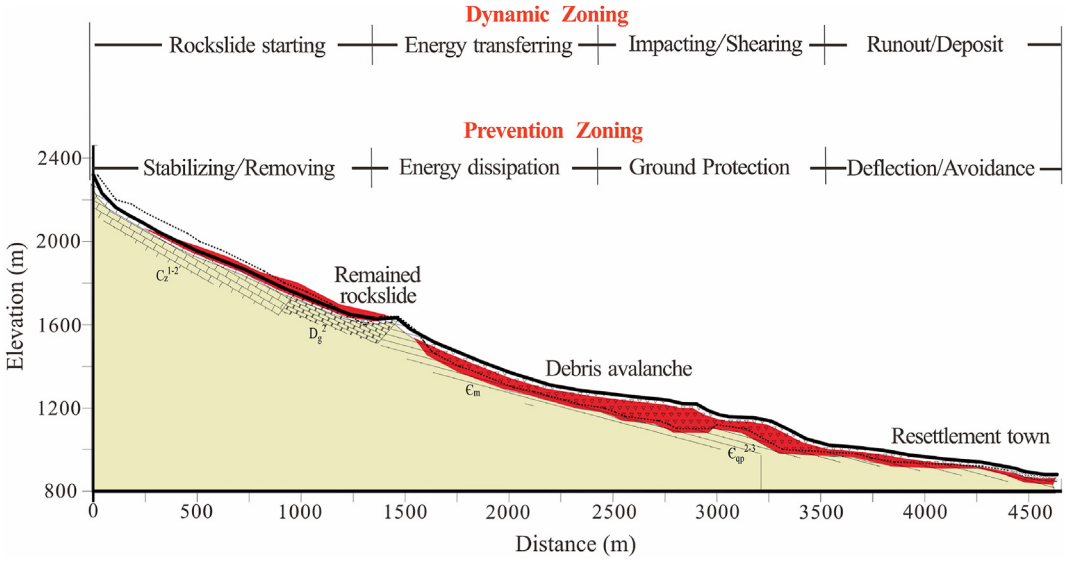

Fig. 40. Schematic of prevention mode of high-altitude and long-runout rockslides.

debris avalanche. Each of the three calculation methods has its own advantages. The physico-mechanical parameters of the limestone are used and the kinematic friction coefficient is all assigned with the same value. In the LPF^{3D}, the field physic-mechanical processes of rockslide during accumulation are considered, and the simulation results are most consistent with the field rockslide accumulation result (Fig. 38).

The dynamic process of rockslide is extremely complex, and using a single-state model and single-phase material is difficult to match the field rockslide movement. A single computational model can be used to simulate post-landslide damage, but it relies on empirical formulations and parameter adjustments by geologists. This numerical model is closer to the actual dynamic process of rockslide, reflecting the polymorphic transformation and the multi-media coupling process of the sliding main body. The LPF^{3D} method in this study can be a good solution to this type of rockslide, as the physico-mechanical parameters of the field rockslide have been used.

5. Risk mitigation and structural prevention measures

5.1. Strategy on structural and non-structural approaches

Structural and non-structural prevention and mitigation measures are needed for accurate identification of initiation zone, and prediction of released time, range of deposits, and secondary effects of long-runout rockslide. Interferometric synthetic aperture radar (InSAR), one of space-borne earth observation technologies, has become an effective means to dynamically recognize and monitor the landslides (Intrieri et al., 2018). The proposed SAR offset-tracking method has achieved good results in large-deformation monitoring of high-altitude and long-runout rockslides in extremely high mountain areas (Liu et al., 2020). We estimated the pre-event deformation of the Baige landslide from October 2014 to August 2018 using the improved SAR offset-tracking approach (Yin et al., 2021a, 2022). The results suggest that the Baige landslide had undergone remarkable deformation before failure, where the maximum deformation rates in the slant-range and azimuth directions of the rockslide reached −9.3 m/yr and 1.9 m/yr, respectively. The cumulative deformation in the slant-range and azimuth directions reached −60.2 m and 12.6 m, respectively from January 2007 to August 2018 (see Fig. 39).

The structural measures are usually adopted to hinder the initiation or propagation of the rockslide by stabilizing the unstable rockslide in the initiation zone or reduce sliding volume, or decelerate the debris avalanche. A series of structural preventions for the risk reduction is proposed on the basis of the diverse dynamic features of initiation, transition (energy transferring) and deposit zone of the long-runout rockslide (see Fig. 40).

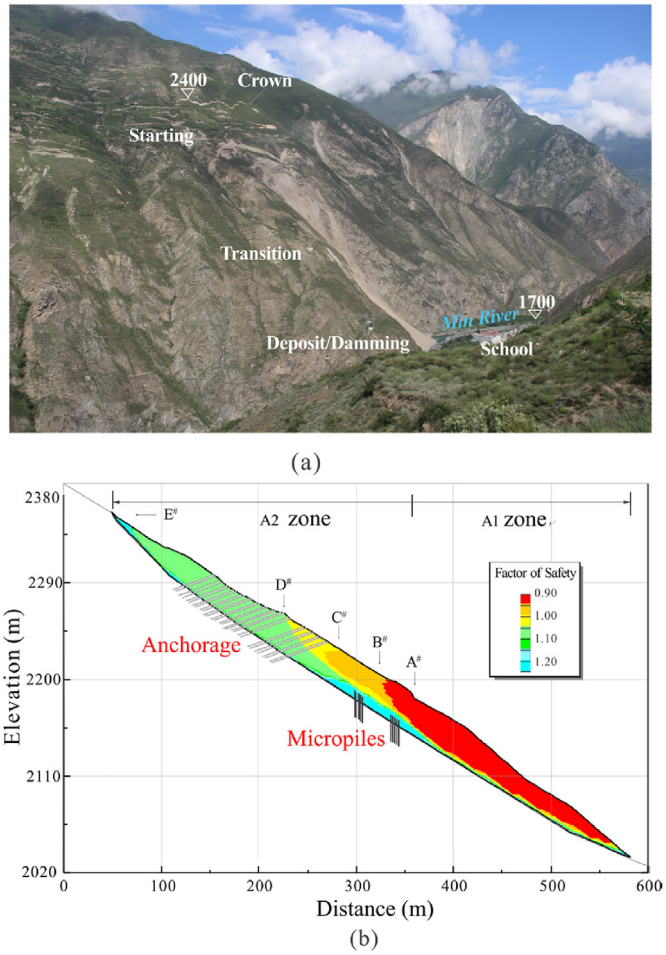

Fig. 41. The Tizicao rockslide and the prevention measures:(a) Overview and zoning; and (b) Structure layout.

5.2. Structural rockslide stabilization in the initiation zone

The elimination of chain disasters can be realized by reinforcing the initiation zone of the potential rockslide actively. The fast and light structures would be a good choice in terms of reinforcement. Located on the right bank of the Min River in Maoxian County, Sichuan Province, China, the Tizicao rockslide has an average longitudinal length of 540 m, an average width of about 560 m, and an average thickness of 45.1 m. The total landslide volume reaches 13.9×10^6 m^3. The height difference between the front and rear edges of the rockslide is about 650 m, and the slope varies from 40° to 80°. If this huge rockslide fails, it is likely to form a landslide dam on the Minjiang River, and further generate a secondary flooding. This could cause damage to the towns, roads and other infrastructure along the Min River (Fig. 41a).

A light structural system using reinforcement technologies, including micropiles and anchorages, was performed on the initiation zone of the Tizicao rockslide in accordance with the characteristics of deformation and stability analysis (Fig. 41b). Ninety-two pre-stressed anchor cables with a total length of 9147 m were applied by 2 × 6 rows in the upper part of the initiation zone. The diameter of drill hole was 128 mm, and the 12-beam anchor cables of prestressing pressure dispersion type were used with single length varying from 37 m to 66.5 m. In the middle part of the initiation zone, 4 rows of micropile groups were performed in an arch ring shape. 122 micropiles were set with a spacing of 2 m × 2 m. The length of a single pile was within 60.5–63.3 m, while a total length of 7548.4 m (Fig. 42).

The soil arch effect due to the micropile-soil interactions and the arc-shaped arrangements of the micropile groups have been revealed by 3D numerical simulation (Yan et al., 2011). The rockslide is assumed to be an elastoplastic material, and an isotropic elastic model was used for the micropile group. The micropile spacing and the spacing between the front and rear rows were both $S = 2$ m, and the micropile groups were arranged in the form of an arch (Wang et al., 2020b). Among them, the distance is 8.5S between the boundary position of the last row piles (arch foot) and the crown position of the first-row piles. The mechanical transmission law of the arc-shaped reinforcement effect has been formed (Martin and Chen, 2005) subsequently. The simulation results are as follows (Fig. 43):

(1) The normal stress on the −8.5S–2S profile in Y-direction is approximately 50 kPa. This value indicates that the rockslide is in a uniform stress state, and only the stress decreases at the boundary, which means the arc-shaped reinforcement effect is not obvious.
(2) At the profile of 0 (i.e. pile-group crown), the mechanical transmission of the arc-shaped reinforcement effect is significant, and the normal stress of the rockslide is only 9 kPa, indicating that stress of about 41 kPa (=50–9 kPa) is transmitted from the landslide to the pile group.
(3) At the profile of 2S, the normal stress of the landslide is 0 kPa, that is, the stress of the remained 9 kPa is transmitted to the pile group. At the profile of 4S–8.5S, the normal stress of the landslide is still 0 kPa, and the stress at the boundary also drops to 0 kPa gradually.

The arching effect of multi-row micropile groups is significant to effectively hinder the movement of the sliding body.

5.3. Dissipating structure on debris avalanche in the transition zone

It is extremely difficult to prevent and control the debris avalanche with high energy, and the effective engineering measures are still immature. Conventional prevention structure is mainly achieved by employing multi-stage check dams to control the sliding mass. This kind of structure often fails when the impact force of the sliding body is too large, and it would further increase the scale of the sliding body and aggravate the severity of the disaster.

This study proposes a mitigation principle focused on momentum reduction instead of blocking the sliding flow. As a result, the boundary layer roughening technology, such as barrier piles, is adopted to slow down the velocity of high-speed debris flow, and the combined structure of reinforced concrete pile and beam is used to realize the energy dissipation by extending the impact time. The simulation by ANSYS shows that the debris flow can form an obvious arch circle effect under the blocking of the pile-beam dam (Fig. 44). Along the axis direction of the pile beam dam, the impact pressure decreased significantly, that is, P0, P1, P2, and P3 decreasing in turn. Along the normal direction of the pile-beam dam, when the multi-sphere chain forms multi-row structure, the impact pressure is also significantly reduced. This energy-dissipating structure has achieved sound results in the prevention project of large and high-altitude debris flow in Zhouqu Country, and has been applied in other mountainous areas as well in Western China (Fig. 45).

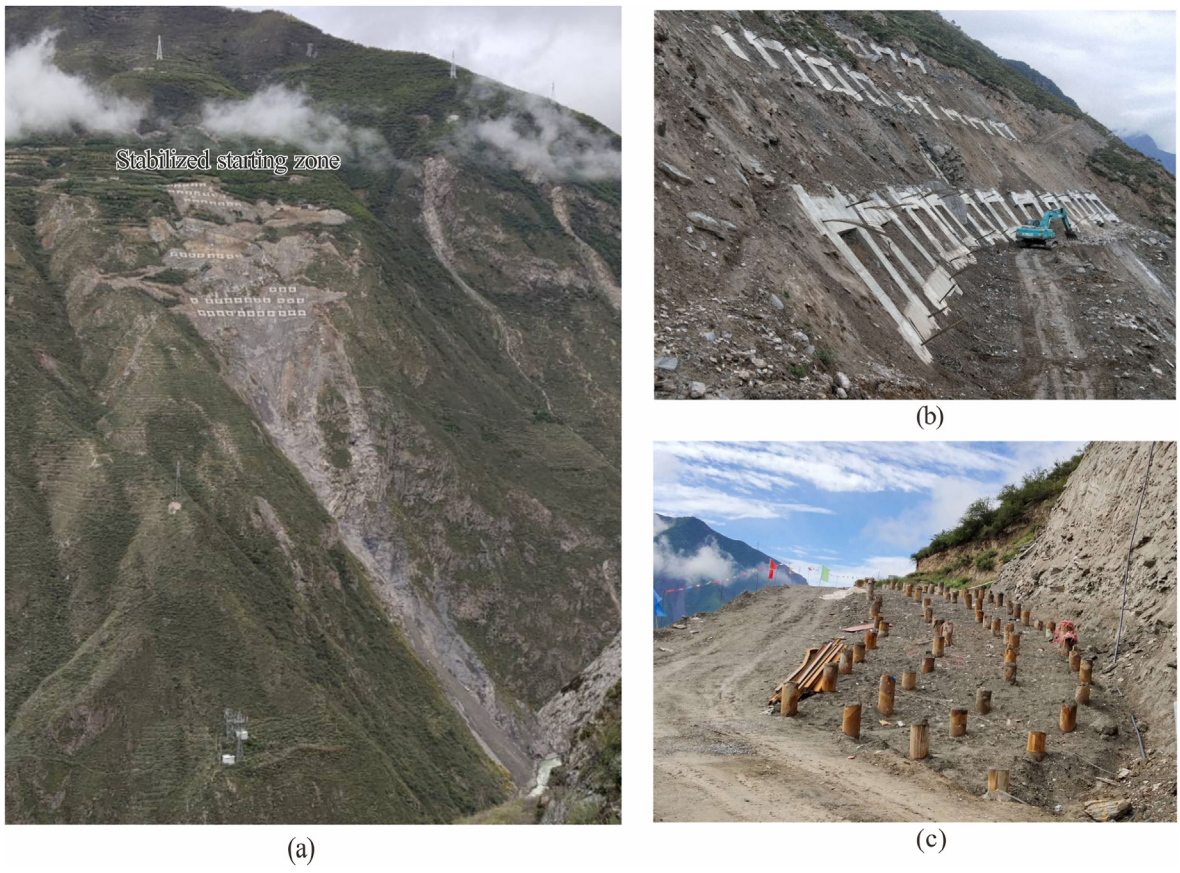

Fig. 42. Stabilization the initiation zone of the Tizicao rockslide: (a) Overview after stabilization; (b) Anchorage with Reinforced concrete lattice; and (c) Micropiles with arc layout.

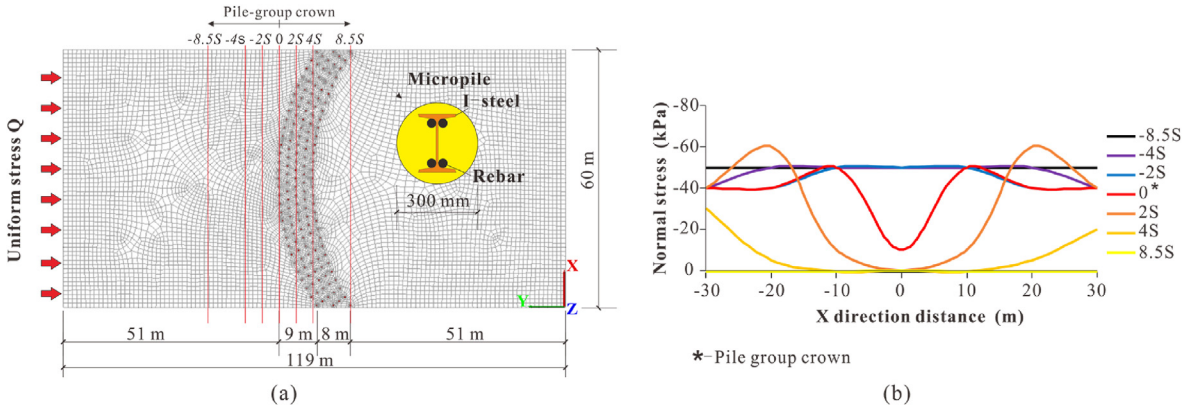

Fig. 43. Simulation results on the arching effect and the stress distribution curves of the micropile groups:(a) Numerical model of the arching effect of the micropile groups. The 2*S*, 4*S*, and 8.5*S* are selected to represent the sliding mass in front of the micropile group crown. the -2*S*, -4*S*, and −8.5*S* are selected to represent the sliding mass in the rear of the micropile group crown; and (b) Stress distributions.

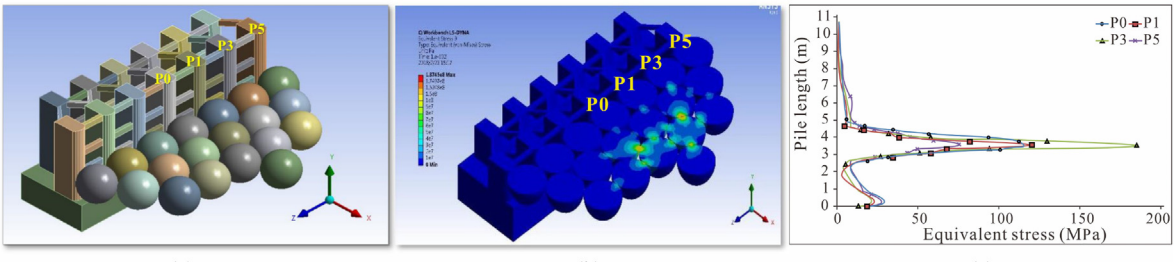

Fig. 44. Numerical simulation on the compositing structure of pile-beam and the arch effect to debris avalanche: (a) Numerical modeling of pile beam dam with four monitoring points (P0, P1, P3, P5); (b) Cloud mapping of arch effect; and (c) Curve of equivalent stress.

Fig. 45. Structural debris avalanche prevention in the transition zone: (a) Under construction; (b) Defense on debris avalanche; and (c) Arch effect to energy dissipation.

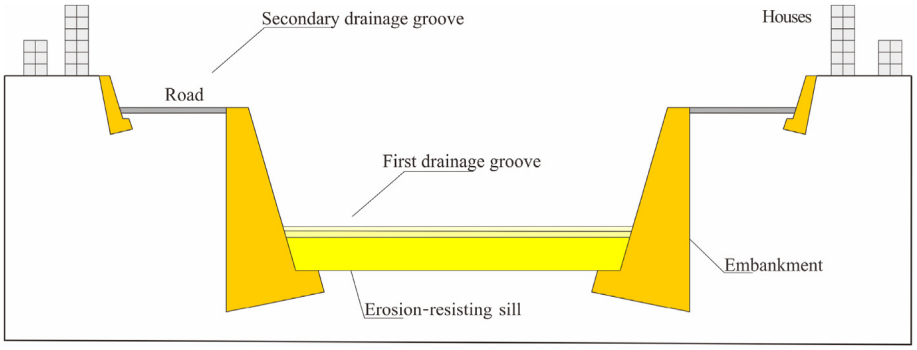

Fig. 46. Composite section drainage groove for debris flow.

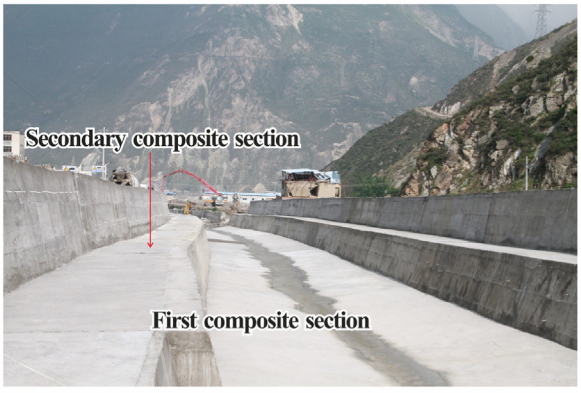

Fig. 47. Cases of composite drainage groove of structural debris flow prevention in runout zone: (a) Composite section drainage groove of debris flow in runout zone at Zhouqu Country; (b) Overview of debris flow prevention at Zhouqu Country; and (c) Composite-section drainage groove at Wenchuan.

5.4. Deflecting and drainage structure on debris flow in the runout/deposition zone

The control project of the super-large high-altitude debris flow in Zhouqu County, Gansu Province, China, has employed a pile-beam dam in the upper part of the transition zone, and a composite drainage system is used in the downstream in order to meet the requirements of the on-site reconstruction.

According to the design, the upper section can be used as public facilities such as municipal roads. Upon heavy rain, the lower section can be used as the channel of the debris flow; when extreme heavy rain happens, both the upper and lower sections could be used as the access of flood and avalanches. In this way, not only the disaster risk of cities along the drainage groove can be effectively reduced, but also the planned construction land can be increased (Figs. 46 and 47).

6. Conclusions

The high-altitude and long-runout rockslides are extremely easy to occur in the Qinghai-Tibet Plateau and its adjacent areas. This kind of complex geohazards usually presents a gigantic scale, large height difference accompanied with high potential energy to form a rapid and long-runout chain-style flow. Moreover, it would cause a secondary disaster chain in river basin and could destroy towns and major infrastructures.

(1) In this paper, the geological structures of high-altitude and long-runout rockslides in the Qinghai-Tibet Plateau and its adjacent areas are studied. The two types of sliding-prone geological structure models, i.e. the fault control type in orogenic belt and the fold control type in platform area, are established.
(2) The geomorphology controlling the high-altitude and long-runout dynamic process of rockslides is discussed. The large-scale experimental apparatus has been constructed to carry out a series of experiments for the chain-style dynamics of rockslide-debris avalanche-debris flow.
(3) A numerical simulation method for the long-runout rockslide-debris avalanche is developed, which verifies the results of large-scale physical experiments. Then, the dynamic characteristics of quasi-static-transition-inertia state transformation and solid-liquid coupling in rapid movement of rockslide-debris avalanche-debris flow are revealed.
(4) The risk mitigation strategy of the non-structure and structure for resilient energy dissipation is proposed for various zones. For the initiation zone, a light and fast stabilizing method of arc-layout micropile group for the high-altitude rockslide is developed. For the transition zone, the combined structure of reinforced concrete pile and beam with energy dissipation is developed to prevent debris avalanche. For the runout/deposition zone where severe disasters occur, the composite structure for deflecting and drainage to debris flow is suggested. These structural prevention and mitigation methods have been successfully applied to the high-altitude and long-runout rockslides or debris flows in Zhouqu, Maoxian of the Wenchuan earthquake zone, and other major geohazards in the Qinghai-Tibet Plateau and its adjacent area.

Declaration of competing interest

The authors declare that they have no known competing financial interests or personal relationships that could have appeared to influence the work reported in this paper.

Acknowledgements

This work was financially supported by National Natural Science Foundation of China (Grant Nos. U2244226, U2244227 and 42177172).

References

Abele, G., 1997. Rockslide movement supported by the mobilization of groundwater-saturated valley floor sediments. Z. Geomorphol. 41 (1), 1–20.
Alford, D., Schuster, R.L., 2000. Usoi Landslide Dam and Lake Sarez-An Assessment of Hazard and Risk in the Pamir Mountains, Tajikistan. United Nations, vol. 1. ISDR Prevention Series No., Geneva, p. 113.
Anderson, S.A., Sitar, N., 1995. Analysis of rainfall-induced debris flows. J. Geotech. Eng. 121 (7), 544–552.
Bagnold, R.A., 1954. Experiments on a gravity-free dispersion of large solid spheres in a Newtonian fluid under shear. Proc. R. Soc. London. A. Math. Phys. Sci. 225 (1160), 49–63.
Bartali, R., Sarocchi, D., Nahmad-Molinari, Y., 2015. Stick-slip motion and high speed ejecta in granular avalanches detected through a multisensors flume. Eng. Geol. 195, 248–257.
Bartelt, P., Buser, O., Platzer, K., 2006. Fluctuation-dissipation relations for granular snow avalanches. J. Glaciol. 52 (179), 631–643.
Bedford, A., Drumheller, D.S., 1983. Theories of immiscible and structured mixtures. Int. J. Eng. Sci. 21 (8), 863–960.
Bouchut, F., Fernández-Nieto, E.D., Mangeney, A., Lagrée, P.Y., 2008. On new erosion models of Savage-Hutter type for avalanches. Acta Mech. 199 (1), 181–208.
Bowman, E.T., Take, W.A., Rait, K.L., Hann, C., 2012. Physical models of rock avalanche spreading behavior with dynamic fragmentation. Can. Geotech. J. 49 (4), 460–476.
Broeckx, J., Rossi, M., Lijnen, K., Campforts, B., Vanmaercke, M., 2019. Landslide mobilization rates: a global analysis and model. Earth Sci. Rev. 201 (4), 102972.
Bruce, I., Cruden, D.M., 1977. The dynamics of the hope slide. Bull. Int. Assoc. Eng. Geol. 16, 94–98.
Bryant, S.K., Take, W.A., Bowman, E.T., 2015. Observations of grain-scale interactions and simulation of dry granular flows in a large-scale flume. Can. Geotech. J. 52, 638–655.
Cambiaghi, A., Schuster, R.L., 1989. Landslide damming and environmental protection—a case study from northern Italy. In: Proceedings of 2nd International Symposium on Environmental Geotechnology, Shanghai, China, vol. 1, pp. 381–385.
Campbell, C.S., 1989. Self-lubrication for long runout landslides. J. Geol. 97 (6), 653–665.
Campbell, C.S., 1990. Rapid granular flows. Annu. Rev. Fluid Mech. 22 (1), 57–90.
Campbell, C.S., Cleary, P.W., Hopkins, M., 1995. Large-scale landslide simulations: global deformation, velocities and basal friction. J. Geophys. Res. Solid Earth 100 (B5), 8267–8283.
Cencetti, C., Di Matteo, L., Romeo, S., 2017. Analysis of Costantino landslide dam evolution (Southern Italy) by means of satellite images, aerial photos, and climate data. Geosciences 7 (2), 30.
Christen, M., Kowalski, J., Bartelt, P., 2010. RAMMS: numerical simulation of dense snow avalanches in three-dimensional terrain. Cold Reg. Sci. Technol. 63 (1–2), 1–14.
Chowdhury, R.N., 1987. Aspects of the vajont slide. Eng. Geol. 24, 533–540.
Crosta, G.B., Frattini, P., Fusi, N., Sosio, R., 2011. Formation, Characterisation and Modeling of the Val Pola Rock-Avalanche Dam (Italy). Natural and Artificial Rockslide Dams. Springer, Berlin, Heidelberg, pp. 347–368.
Crosta, G.B., Agliardi, F., Rivolta, C., Alberti, S., Dei Cas, L., 2017. Long-term evolution and early warning strategies for complex rockslides by real-time monitoring. Landslides 14 (5), 1615–1632.
Cruden, D.M., Hungr, O., 1986. The debris of the Frank Slide and theories of rockslide-avalanche mobility. Can. J. Earth Sci. 23 (3), 425–432.
Cruden, D.M., Varnes, D.J., 1996. Landslide types and processes. In: Turner, A.K., Schuster, R.L. (Eds.), Landslides Investigation and Mitigation. Transportation research board, US National Research Council. Special Report 247, Washington, DC, pp. 36–75 (Chapter 3).
Cui, P., Jia, Y., Su, F.H., Ge, Y.G., Chen, X.Q., Zou, Q., 2017. Natural hazards in Tibetan Plateau and key issue for feature research. Bull. Chin. Acad. Sci. 32 (9), 985–992 (in Chinese).
Dai, F.C., Tu, X.B., Xu, C., Gong, Q.M., Yao, X., 2011. Rock avalanches triggered by oblique-thrusting during the 12 May 2008 Ms 8.0 Wenchuan earthquake, China. Geomorphology 132 (3–4), 300–318.
Davies, T.R., McSaveney, M.J., Hodgson, K.A., 1999. A fragmentation-spreading model for long runout rock avalanches. Can. Geotech. J. 36 (6), 1096–1110.
Davies, T.R., McSaveney, M.J., 2009. The role of rock fragmentation in the motion of large landslides. Eng. Geol. 109 (1–2), 67–79.
Davies, T.R., 1982. Spreading of rock avalanche debris by mechanical fluidization. Rock Mech. 15 (1), 9–24.
Delaney, K.B., Evans, S.G., 2014. The 1997 Mount Munday landslide (British Columbia) and the behaviour of rock avalanches on glacier surfaces. Landslides 11 (6), 1019–1036.

Delaney, K.B., Evans, S.G., 2017. The evolution (2010-2015) and engineering mitigation of a rockslide-dammed lake (Hunza River, Pakistan); Characterization by analytical remote sensing. Eng. Geol. 220, 65–75.
Deline, P., 2001. Recent Brenva rock avalanches (Valley of Aosta): new chapter in an old story. Geogr. Fis. Din. Quaternaria 5, 55–63.
Deline, P., 2009. Interactions between rock avalanches and glaciers in the Mont Blanc massif during late Holocene. Quat. Sci. Rev. 28 (11–12), 1070–1083.
Deng, J.H., Gao, Y.J., Yu, Z.Q., Xie, H.P., 2019. Analysis on the formation mechanism and process of Baige landslides damming the upper reach of Jinsha River, China. Adv. Eng. Sci. 51 (1), 9–16 (in Chinese).
Dufresne, A., 2012. Granular flow experiments on the interaction with stationary runout path materials and comparison to rock avalanche events. Earth Surf. Process. Landforms 37 (14), 1527–1541.
Dufresne, A., Wolken, G.J., Hibert, C., et al., 2019. The 2016 Lamplugh rock avalanche, Alaska: deposit structures and emplacement dynamics. Landslides 16, 2301–2319.
Dunning, S.A., Mitchell, W.A., Rosser, N.J., Petley, D.N., 2007. The Hattian Bala rock avalanche and associated landslides triggered by the Kashmir Earthquake of 8 October 2005. Eng. Geol. 93, 130–144.
Egashira, S., Honda, N., Itoh, T., 2001. Experimental study on the entrainment of bed material into debris flow. Phys. Chem. Earth Part C 26 (9), 645–650.
Ellen, S.D., Fleming, R.W., 1987. Mobilization of Debris FLows from Soil Slips, San Francisco Bay Region, California. Reviews in Engineering Geology. Geological Society of America, pp. 31–40.
Estep, J., Dufek, J., 2012. Substrate effects from force chain dynamics in dense granular flows. J. Geophys. Res. Earth Surf. 117, F01028.
Evans, S.G., DeGraff, J.V., 2002. Catastrophic Landslides: Effects, Occurrence, and Mechanisms. Geological Society of America, Boulder, CO, USA.
Evans, S.G., Guthrie, R.H., Roberts, N.J., Bishop, N.F., 2007. The disastrous 17 February 2006 rockslide-debris avalanche on Leyte Island, Philippines: a catastrophic landslide in tropical mountain terrain. Nat. Hazards Earth Syst. Sci. 7 (1), 89–101.
Evans, S.G., Roberts, N.J., Ischuk, A., Delaney, K.B., Morozova, G.S., Tutubalina, O., 2009. Landslides triggered by the 1949 Khait earthquake, Tajikistan, and associated loss of life[J]. Eng. Geol. 109 (3–4), 195–212.
Fan, X.M., Yunus, A.P., Yang, Y.H., et al., 2022. Imminent threat of rock-ice avalanches in high mountain Asia. Sci. Total Environ. 836, 155380.
Farin, M., Mangeney, A., Roche, O., 2014. Fundamental changes of granular flow dynamics, deposition, and erosion processes at high slope angles: insights from laboratory experiments. J. Geophys. Res. Earth Surf. 119 (3), 504–532.
Feng, C., Li, S.H., Liu, X.Y., Zhang, Y.N., 2014. A semi-spring and semi-edge combined contact model in CDEM and its application to analysis of Jiweishan landslide. J. Rock. Mech. Geotech. 6 (1), 26–35.
Feng, Z., Li, B., Cai, Q.P., Cao, J.W., 2016. Initiation mechanism of the Jiweishan landslide in Chongqing, south-western China. J. Environ. Eng. Geophys. 22 (4), 341–351.
Gao, Y., Yin, Y.P., Li, B., et al., 2017. Characteristics and numerical runout modeling of the heavy rainfall-induced catastrophic landslide-debris flow at Sanxicun, Dujiangyan, China, following the Wenchuan Ms 8.0 earthquake. Landslides 14 (4), 1361–1374.
Gao, Y., Yin, Y., Li, B., Feng, Z., He, K., 2018. Characteristics and numerical runout modeling analysis of the Jiweishan landslide, Chongqing, China. Environ. Eng. Geosci. 24 (4), 413–423.
Gao, Y., Li, B., Gao, H.Y., Chen, L.C., Wang, Y.F., 2020. Dynamic characteristics of high-elevation and long runout landslides in the Emeishan basalt area: a case study of the Shuicheng "7.23" landslide in Guizhou, China. Landslides 17, 1663–1677.
Gao, Y., Gao, H.Y., Li, B., Wei, T.Y., Li, Z., 2022a. Experimental preliminary analysis of the fluid drag effect in rapid and long runout flow-like landslides. Environ. Earth Sci. 81 (3), 1–13.
Gao, Y., Yin, Y.P., Li, B., Wei, T.Y., Li, Z., Gao, H.Y., 2022b. The role of fluid drag force in the dynamic process of two-phase flow-like landslides. Landslides 19, 1791–1805.
Gao, Y., Yin, Y.P., Li, Z., Li, B., Wu, W.L., Zhang, H., 2022c. Study on the dynamic disintegration effect of high position and long runout rock landslide. Chin. J. Rock Mech. Eng. 1–13 (in Chinese).
Guo, Z.L., Cui, G.F., 2013. Geomorphologic regionalization of China aimed at construction of nature reserve system. Acta Ecol. Sin. 33 (19), 6264–6276 (in Chinese).
Guthrie, R.H., Friele, P., Allstadt, K., et al., 2012. The 6 August 2010 Mount Meager rock slide-debris flow, Coast Mountains, British Columbia: characteristics, dynamics, and implications for hazard and risk assessment. Nat. Hazards Earth Syst. Sci. 12 (5), 1277–1294.
Hadley, J.B., 1978. Madison Canyon rockslide, Montana. U.S.A. Develop. Geotech. Eng. 14, 167–180.
Hardin, B.O., 1985. Crushing of soil particles. J.Geotech. Eng. 111 (10), 1177–1191.
Haug, Ø.T., Rosenau, M., Leever, K., Oncken, O., 2016. On the energy budgets of fragmenting rockfalls and rockslides: insights from experiments. J. Geophys. Res. Earth Surf. 121 (7), 1310–1327.
He, K., Yin, Y., Li, B., Chen, C., 2019. The mechanism of the bottom-crashing rockfall of a massive layered carbonate rock mass at Zengziyan, Chongqing, China. J. Earth Syst. Sci. 128 (4), 1–13.
Hearn, G.J., 1995. Landslide and erosion hazard mapping at Ok Tedi copper mine, Papua New Guinea. Q. J. Eng. Geol. Hydrogeol. 28 (1), 47–60.
Heim, A., 1932. Bergsturz und Menschenleben. Fretz and Wasmuth Verlag, Zurich, p. 218.
Hewitt, K., Clague, J.J., Orwin, J.F., 2008. Legacies of catastrophic rock slope failures in mountain landscapes. Earth Sci. Rev. 87 (1–2), 1–38.
Hsü, K.J., 1975. Catastrophic debris streams (sturzstroms) generated by rockfalls. Geol. Soc. Am. Bull. 86 (1), 129–140.
Hsü, K.J., Voight, B., 1978. Albert Heim: observations on landslides and relevance to modern interpretations. Nat. Pheno. 1, 70–93.
Huang, R.Q., 2009. Some catastrophic landslides since the twentieth century in the southwest of China. Landslides 6 (1), 69–81.
Huang, R.Q., Pei, X.J., Zhang, W.F., Li, S.G., Li, B.L., 2009. Further examination on characteristics and formatiom mechanism of Daguangbao landslide. J. Eng. Geol. 17 (6), 725–736 (in Chinese).
Hubbard, B., Heald, A., Reynolds, J.M., et al., 2005. Impact of a rock avalanche on a moraine-dammed proglacial lake: laguna Safuna Alta, Cordillera Blanca, Peru. Earth Surf. Process. Landforms 30 (10), 1251–1264.
Hungr, O., Evans, S.G., 2004. Entrainment of debris in rock avalanches: an analysis of a long run-out mechanism. Geol. Soc. Am. Bull. 116, 1240–1252.
Hungr, O., Leroueil, S., Picarelli, L., 2014. The Varnes classification of landslide types, an update. Landslides 11 (2), 167–194.
Hutchinson, J.N., Kojan, E., 1975. The Mayunmarca Landslide of 25th April 1974, Peru, Report Ser. No. 3124. RMO.RD/SCE, UNESCO, Paris.
Ibañez, J.P., Hatzor, Y.H., 2018. Rapid sliding and friction degradation: lessons from the catastrophic Vajont landslide. Eng. Geol. 244, 96–106.
International Union of Geological Sciences Working Group on Landslides, 1995. A suggested method for describing the rate of movement of a landslide. Bull. Int. Assoc. Eng. Geol. 52, 75–78.
Intrieri, E., Raspini, F., Fumagalli, A., et al., 2018. The Maoxian landslide as seen from space: detecting precursors of failure with Sentinel-1 data. Landslides 15 (1), 123–133.
Iverson, R.M., 1997. The physics of debris flows. Rev. Geophys. 35 (3), 245–296.
Iverson, R.M., Ouyang, C.J., 2015. Entrainment of bed material by Earth-surface mass flows: review and reformulation of depth-integrated theory. Rev. Geophys. 53 (1), 27–58.
Iverson, R.M., Logan, M., Denlinger, R.P., 2004. Granular avalanches across irregular three-dimensional terrain: 2. Experimental tests. J. Geophys. Res. 109, F01015.
Iverson, R.M., Reid, M.E., Logan, M., LaHusen, R.G., Godt, J.W., Griswold, J.P., 2011. Positive feedback and momentum growth during debris-flow entrainment of wet bed sediment. Nat. Geosci. 4 (2), 116–121.
Jaeger, H.M., Nagel, S.R., Behringer, R.P., 1996. Granular solids, liquids, and gases. J. Rev. Mod. Phys. 68 (4), 1259.
Johnson, C.G., Kokelaar, B.P., Iverson, R.M., Logan, M., LaHusen, R.G., Gray, M.N.T., 2012. Grain-size segregation and levee formation in geophysical mass flows. J. Geophys. Res. Earth Surf. 117, F01032.
Keefer, D.K., Wilson, R.C., Mark, R.K., 1987. Real-time landslide warning during heavy rainfall. Science 238 (4829), 921–925.
Khan, A.R., Richardson, J.F., 1987. The resistance to motion of a solid sphere in a fluid. Chem. Eng. Commun. 62 (1–6), 135–150.
King, J., Loveday, I., Schuster, R.L., 1989. The 1985 Bairaman River landslide dam and resulting debris flow, Papua New Guinea. Q. J. Eng. Geol. Hydrogeol. 22 (4), 257–270.
Knapp, S., Krautblatter, M., 2020. Conceptual framework of energy dissipation during disintegration in rock avalanches. Front. Environ. Sci. 8, 263.
Kokelaar, B.P., Graham, R.L., Gray, J., et al., 2014. Fine-grained linings of leveed channels facilitate runout of granular flows. Earth Planet Sci. Lett. 385, 172–180.
Kuo, Y.S., Tsai, Y.J., Chen, Y.S., Lun, C.J., Shieh, C.L., Itoh, T., 2013. Movement of deep-seated rainfall-induced landslide at hsiaolin village during typhoon morakot. Landslides 10 (2), 191–202.
Lanzoni, S., Gregoretti, C., Stancanelli, L.M., 2017. Coarse-grained debris flow dynamics on erodible beds. J. Geophys. Res. Earth Surf. 122 (3), 592–614.
Lee, C.H., Huang, Z., 2018. A two-phase flow model for submarine granular flows: with an application to collapse of deeply-submerged granular columns. Adv. Water Resour. 115, 286–300.
Li, B., Feng, Z., Wang, G.Z., Wang, W.P., 2016. Processes and behaviors of block topple avalanches resulting from carbonate slope failures due to underground mining. Environ. Earth Sci. 75 (8), 1–26.
Li, B., Gao, Y., Yin, Y.P., He, K., Wu, W.L., Zhang, H., 2022. Rainstorm-induced large-scale landslides in northeastern Chongqing, China, August 31 to September 2, 2014. Bull. Eng. Geol. Environ. 81 (7), 1–15.
Li, K., Wang, Y.F., Lin, Q.W., Cheng, Q.G., Wu, Y., 2021. Experiments on granular flow behavior and deposit characteristics: implications for rock avalanche kinematics. Landslides 18 (5), 1779–1799.
Liu, C.Z., Lü, J.T., Tong, L.Q., et al., 2019. Research on glacial/rock fall-landslide-debris flows in Sedongpu basin along Yarlung Zangbo River in Tibet. Chin. Geol. 46 (2), 219–234 (in Chinese).
Liu, G.R., 1988. Environmental geologic investigation of Xintan landslide. Environ. Geol. Water Sci. 12 (1), 11–13.
Liu, X.J., Zhao, C.Y., Zhang, Q., Lu, Z., Li, Z.H., 2020. Deformation of the Baige landslide, Tibet, China, revealed through the integration of cross-platform ALOS/PALSAR-1 and ALOS/PALSAR-2 SAR observations. Geophys. Res. Lett. 47 (3), 1–8.

Locat, P., Couture, R., Leroueil, S., Locat, J., Jaboyedoff, M., 2006. Fragmentation energy in rock avalanches. Can. Geotech. J. 43 (8), 830–851.
Luo, H.Y., Shen, P., Zhang, L.M., 2019. How does a cluster of buildings affect landslide mobility: a case study of the Shenzhen landslide. Landslides 16 (12), 2421–2431.
Mangeney, A., Roche, O., Hungr, O., Mangold, N., Faccanoni, G., Lucas, A., 2010. Erosion and mobility in granular collapse over sloping beds. J. Geophys. Res. Earth Surf. 115 (F3).
Manzella, I., Labiouse, V., 2013. Empirical and analytical analyses of laboratory granular flows to investigate rock avalanche propagation. Landslides 10, 23–36.
Martin, G.R., Chen, C.Y., 2005. Response of piles due to lateral slope movement. Comput. Struct. 83 (8–9), 588–598.
McDougall, S., Hungr, O., 2004. A model for the analysis of rapid landslide motion across three-dimensional terrain. Can. Geotech. J. 41 (6), 1084–1097.
McGovern, S., Brook, M.S., Cave, M., 2021. Geomorphology and triggering mechanism of a river-damming block slide: February 2018 Mangapoike landslide, New Zealand. Landslides 18 (3), 1087–1095.
McSaveney, M.J., 1978. Sherman glacier rock avalanche, Alaska, USA. Dev. Geotech. Eng. 14, 197–258.
McSaveney, M.J., Davies, T.R., Hodgson, K.A., 2000. A contrast in deposit style between large and small rock avalanches. In: Proceedings of the 8th International Symposium on Landslides. Cardiff, Wales, pp. 1052–1058.
McSaveney, M.J., 2002. Recent rockfalls and rock avalanches in mount Cook national park, New Zealand. Rev. Eng. Geol. 15, 35–70.
Melillo, M., Brunetti, M.T., Peruccacci, S., Gariano, S.L., Guzzetti, F., 2015. An algorithm for the objective reconstruction of rainfall events responsible for landslides. Landslides 12, 311–320.
Melo, V., Easton, G., Rebolledo, S., 2022. On the genesis of a massive Holocene rock avalanche deposit in the Yeso River catchment, Andes Cordillera of central Chile. Geomorphology 406, 108214.
Melosh, H.J., 1979. Acoustic fluidization: a new geologic process? J. Geophys. Res. Solid Earth 84 (B13), 7513–7520.
MiDi, G.D.V., 2004. On dense granular flows. Eur. Phys. J. E 14 (4), 341–365.
Möbius, M.E., Lauderdale, B.E., Nagel, S.R., Jaeger, H.M., 2001. Brazil-nut effect-size separation of granular particles. Nature 414, 270.
Noverraz, F., Bonnard, C., 1992. L'ecroulement rocheux de Randa, pres de Zermatt (Randa rockslide near Zermatt). Int. Symp. Landslides 1, 165–170 (in Trench).
Ouyang, C.J., He, S.M., Xu, Q., Luo, Y., Zhang, W.C., 2013. A MacCormack-TVD finite difference method to simulate the mass flow in mountainous terrain with variable computational domain. Comput. Geosci. 52, 1–10.
Pánek, T., 2019. Landslides and quaternary climate changes—the state of the art. Earth Sci. Rev. 196, 102871.
Pedersen, S.A.S., Larsen, L.M., Dahl-Jensen, T., et al., 2002. Tsunami-generating rock fall and landslide on the south coast of Nuussuaq, central West Greenland. Geol. Greenl. Sur. Bull. 191, 73–83.
Peng, J.B., Cui, P., Zhuang, J.Q., 2020. Challenges to engineering geology of Sichuan-Tibet railway. Chin. J. Rock Mech. Eng. 39 (12), 2377–2389 (in Chinese).
Plafker, G., Ericksen, G.E., 1978. Nevados huascaran avalanches, Peru. Dev. Geotech. Eng. 14, 277–314.
Pollet, N., Schneider, J.L.M., 2004. Dynamic disintegration processes accompanying transport of the Holocene Flims sturzstrom (Swiss Alps). Earth Planet Sci. Lett. 221 (1–4), 433–448.
Pollet, N., 2004. Significance of initiation zones and deposits in the analysis of high-speed rock movements: Alpine examples. Bull. Eng. Geol. Environ. 63 (4), 353–366.
Post, A., 1967. Effects of the March 1964 Alaska Earthquake on Glaciers. US Government Printing Office, USA.
Pouliquen, O., Chevoir, F., 2002. Dense flows of dry granular material. C.R. Phys. 3 (2), 163–175.
Pudasaini, S.P., 2012. A general two-phase debris flow model. J. Geophys. Res. Earth Surf. 117, F03010.
Pudasaini, S.P., Domnik, B., 2009. Energy considerations in accelerating rapid shear granular flows. Nonlinear Process Geophys. 16 (3), 399–407.
Pudasaini, S.P., Miller, S.A., 2013. The hypermobility of huge landslides and avalanches. Eng. Geol. 157, 124–132.
Roux, J.N., Combe, G., 2002. Quasistatic rheology and the origins of strain. C.R. Phys. 3 (2), 131–140.
Sanvitale, N., Bowman, E.T., 2017. Visualization of dominant stress-transfer mechanisms in experimental debris flows of different particle-size distribution. Can. Geotech. J. 54 (2), 258–269.
Sassa, K., Nagai, O., Solidum, R., Yamazaki, Y., Ohta, H., 2010. An integrated model simulating the initiation and motion of earthquake and rain induced rapid landslides and its application to the 2006 Leyte landslide. Landslides 7 (3), 219–236.
Schwarzkopf, L.M., Schmincke, H., Cronin, S.J., 2005. A conceptual model for block-and-ash flow basal avalanche transport and deposition, based on deposit architecture of 1998 and 1994 Merapi flows. J. Volcanol. Geoth. Res. 139 (1–2), 117–134.
Sheng, L.T., Hsiau, S.S., Hsu, N.W., 2021. Experimental study of the dynamic behavior and segregation of density-bidisperse granular sliding masses at the laboratory scale. Landslides 18 (6), 2095–2110.
Shugar, D.H., Jacquemart, M., Shean, D., et al., 2021. A massive rock and ice avalanche caused the 2021 disaster at Chamoli, Indian Himalaya. Science 373 (6552), 1–14.
Smith, D., Hungr, O., 1992. Failure behaviour of large rockslides. Report to the geological survey of Canada and BC hydro and power Authority. Thurber Engineering, Report, 16–11–6.
Stokes, G.G., 1851. On the Effect of the Internal Friction of Fluids on the Motion of Pendulums. Transactions of the Cambridge Philosophical Society.
Storm, A., Li, L.P., Lan, H.X., 2019. Rock avalanche mobility: optimal characterization and the effects of confinement. Landslides 16 (8), 1437–1452.
Straub, S., 1996. Self-organization in the rapid flow of granular material: evidence for a major flow mechanism. Geol. Rundsch. 85 (1), 85–91.
Straub, S., 1997. Predictability of long runout landslide motion: implications from granular flow mechanics. Geol. Rundsch. 86 (2), 415–425.
Tang, C., 1991. A study on large-scale catastrophic landslide at Touzai gully of Zhaotong. Yunnan Geogr. Environ. Res. 3 (2), 64–71 (in Chinese).
Takahashi, T., 1978. Mechanical characteristics of debris flow. J. Hydraul. Div. 104 (8), 1153–1169.
Takahashi, T., 2007. Debris Flow: Mechanics, Prediction and Countermeasures. Taylor & Francis, London, England.
Takarada, S., Ui, T., Yamamoto, Y., 1999. Depositional features and transportation mechanism of valley-filling Iwasegawa and Kaida debris avalanches, Japan. Bull. Volcanol. 60 (7), 508–522.
Tocher, D., Miller, D.J., 1958. Field observations on effects of Alaska earthquake of 10 July 1958. Science 129 (3346), 394–395.
Van Tien, P., Sassa, K., Takara, K., 2018. Formation process of two massive dams following rainfall-induced deep-seated rapid landslide failures in the Kii Peninsula of Japan. Landslides 15 (9), 1761–1778.
Varnes, D.J., 1978. Slope movement types and processes. In: Schuster, R.L., Krizek, R.J. (Eds.), Landslides, Analysis and Control, Special Report 176: Transportation Research Board. National Academy of Sciences, Washington, DC, USA, pp. 11–33.
Vessia, G., Parise, M., Brunetti, M.T., et al., 2014. Automated reconstruction of rainfall events responsible for shallow landslides. Nat. Hazards Earth Syst. Sci. 14 (9), 2399–2408.
Voight, B., 1978. Lower gros Ventre slide, Wyoming. U.S.A. Dev. Geotech. Eng. 14, 113–162.
Wang, F.W., Sun, P., Highland, L., Cheng, Q.G., 2014a. Key factors influencing the mechanism of rapid and long runout landslides triggered by the 2008 Wenchuan earthquake, China. Geoenviron. Dis. 1 (1), 1–16.
Wang, G.H., Huang, R.Q., Lourenço, S.D.N., Kamai, T., 2014b. A large landslide triggered by the 2008 Wenchuan (M8.0) earthquake in Donghekou area: phenomena and mechanisms. Eng. Geol. 182, 148–157.
Wang, W.N., Chigira, M., Furuya, T., 2003. Geological and geomorphological precursors of the Chiu-fen-erh-Shan landslide triggered by the Chi-Chi earthquake in central Taiwan. Eng. Geol. 69 (1–2), 1–13.
Wang, W.P., Yin, Y.P., Li, D.H., Meng, M.H., Luo, G., Zhang, Z.H., 2020a. Numerical simulation study of the load sharing of an arched micropile group in the Tizicao high-position landslide, China. IOP Conf. Ser. Earth Environ. Sci. 570 (6), 062001.
Wang, W.P., Yin, Y.P., Zhu, S.N., Wang, L.C., Zhang, N., Zhao, R.X., 2020b. Investigation and numerical modeling of the overloading-induced catastrophic rockslide avalanche in Baige, Tibet, China. Bull. Eng. Geol. Environ. 79 (4), 1765–1779.
Xu, Q., Zheng, G., Li, W.L., et al., 2018. Study on successive landslide damming events of Jinsha River in Baige village on Octorber 11 and november 3, 2018. J. Eng. Geol. 26 (6), 1534–1551 (in Chinese).
Xu, W.J., Dong, X.Y., 2021. Simulation and verification of landslide tsunamis using a 3D SPH-DEM coupling method. Comput. Geosci. 129, 103803.
Xu, Z.M., Huang, R.Q., Tang, Z.G., 2007. Engineering geological characteristics of the Touzhai Landslide and its occurrence mechanisms. Geol. Rev. 53 (5), 727–728 (in Chinese).
Yan, J.K., Yin, Y.P., Men, Y.M., et al., 2011. Model test study of landslide reinforcement with micropile groups. China Civ. Eng. J. 44 (4), 120–128 (in Chinese).
Yang, H.Q., Xing, S.G., Wang, Q., Li, Z., 2018. Model test on the entrainment phenomenon and energy conversion mechanism of flow-like landslides. Eng. Geol. 239, 119–125.
Yang, M.D., Yang, Y.F., Hsu, S.C., 2004. Application of remotely sensed data to the assessment of terrain factors affecting the Tsao-Ling landslide. Can. J. Rem. Sens. 30 (4), 593–603.
Yin, Y.P., 2000. Study on a rapid and long runout rockslide at Yigong, Bomi, Tibet. Hydrogeol. Eng. Geol. (4), 8–11 (in Chinese).
Yin, Y.P., Wang, F.W., Sun, P., 2009. Landslide hazards triggered by the 2008 Wenchuan earthquake, Sichuan, China. Landslides 6 (2), 139–152.
Yin, Y.P., Sun, P., Zhang, M., Li, B., 2011. Mechanism on apparent dip sliding of oblique inclined bedding rockslide at Jiweishan, Chongqing, China. Landslides 8 (1), 49–65.
Yin, Y.P., Peng, X.M., 2007. Failure mechanism on qianjiangping landslide in the three gorges reservoir region. Hydrogeol. Eng. Geol. 3, 51–54 (in Chinese).
Yin, Y.P., Xing, A.G., 2012. Aerodynamic modeling of the Yigong gigantic rock slide-debris avalanche, Tibet, China. Bull. Eng. Geol. Environ. 71 (1), 149–160.
Yin, Y.P., Cheng, Y.L., Liang, J.T., Wang, W.P., 2016. Heavy-rainfall-induced catastrophic rockslide-debris flow at Sanxicun, dujiangyan, after the wenchuan ms 8.0 earthquake. Landslides 13, 9–23.
Yin, Y.P., Xing, A.G., Wang, G.H., Feng, Z., Li, B., Jiang, Y., 2017a. Experimental and numerical investigations of a catastrophic long runout landslide in Zhenxiong, Yunnan, southwestern China. Landslides 14 (2), 649–659.
Yin, Y.P., Wang, W.P., Zhang, N., Yan, J.K., Wei, Y.J., Yang, L.W., 2017b. Long runout geological disaster initiated by the ridge-top rockslide in a strong earthquake

area: a case study of the Xinmo landslide in Maoxian County, Sichuan Province. Chin. Geol. 44 (5), 827–841 (in Chinese).
Yin, Y.P., Wang, W.P., 2020. A dynamic erosion plowing model of long Run-out landslides initialized at high location. Chin. J. Rock Mech. Eng. 39 (8), 1513–1521 (in Chinese).
Yin, Y.P., Huang, B.l., Zhang, Q., Yan, G.Q., Dai, Z.W., 2020. Research on recently occurred reservoir-induced Kamenziwan rockslide in three gorges reservoir, China. Landslides 17 (2), 1–15.
Yin, Y.P., Zhu, S.N., Li, B., 2021a. Long Run-Out Geological Hazards at High Location on the Qinghai-Tibet Plateau. Science Press, Beijing, China (in Chinese).
Yin, Y.P., Li, B., Zhang, T.T., et al., 2021b. The February 7 of 2021 glacier-rock and ice avalanche and the outburst flooding disaster chain in Chamoli, India. Chin. J. Geol. Hazard Control 32 (3), 1–8 (in Chinese).
Yin, Y.P., Liu, X.J., Zhao, C.Y., et al., 2022. Multi-dimensional and long-term time series monitoring and early warning of landslide hazard with improved cross-platform SAR offset tracking method. Sci. China Technol. Sci. 65 (8), 1674–7321.
Yue, Z.Q., 2013. Cause and mechanism of highly compressed and dense methane gas mass for Wenchuan Earthquake and associated rock-avalanches and surface co-seismic ruptures. Earth Sci. Front. 20 (6), 15–20.
Zhang, M., Yin, Y.P., McSaveney, M., 2016. Dynamics of the 2008 earthquake-triggered Wenjiagou Creek rock avalanche, qingping, Sichuan, China. Eng. Geol. 200, 75–87.
Zhang, M., McSaveney, M., Shao, H., Zhang, C.Y., 2018. The 2009 Jiweishan rock avalanche, Wulong, China: precursor conditions and factors leading to failure. Eng. Geol. 233, 225–230.
Zhang, S.L., Yin, Y.P., Hu, X.W., Wang, W.P., Wang, L.Q., 2020a. Dynamics and emplacement mechanisms of the successive Baige landslides on the upper reaches of the Jinsha River, China. Eng. Geol. 278, 105819.
Zhang, S.L., Yin, Y.P., Hu, X.W., Wang, W.P., Zhu, S.N., Zhang, N., Cao, S.H., 2020b. Initiation mechanism of the Baige landslide on the upper reaches of the Jinsha River, China. Landslides 17 (12), 2865–2877.
Zhang, T.T., Yin, Y.P., Li, B., et al., 2022. Characteristics and dynamic analysis of the February 2021 long runout disaster chain triggered by massive rock and ice avalanche at Chamoli, Indian Himalaya. J. Rock Mech. Geotech. Eng. https://doi.org/10.1016/j.jrmge.2022.04.003.
Zhao, T., Crosta, G.B., Dattola, G., Utili, S., 2018. Dynamic fragmentation of jointed rock blocks during rockslide-avalanches: insights from discrete element analyses. J. Geophys. Res. Solid Earth 123 (4), 3250–3269.
Zhou, G.G.D., Sun, Q.C., 2013. Three-dimensional numerical study on flow regimes of dry granular flows by DEM. Powder Technol. 239, 115–127.
Zhu, S.N., Yin, Y.P., Li, B., 2018. Evolution characteristics of weak intercalation in massive layered rockslides-A case study of Jiweishan rockslide in Wulong, Chongqing. J. Eng. Geol. 26 (6), 1638–1647 (in Chinese).
Zou, Z.X., Tang, H.M., Xiong, C.R., Su, A.J., Robert, E.C., 2017. Kinetic characteristics of debris flows as exemplified by field investigations and discrete element simulation of the catastrophic Jiweishan rockslide, China. Geomorphology 295, 1–15.

Prof. Yueping Yin received his PhD degree at the China Academy of Geosciences in 1990. He is the Chief Geologist of the China Institute of Geo-Environment Monitoring directly under China Geological Survey, also serves as a member of the Expert Steering Committee of the China National Commission for Disaster Reduction. He had been elected as the President of International Consortium on Landslides under UNESCO and ISDR from 2014 to 2017, also is an associate editor of *Landslides*. Prof. Yin has conducted the researches on geological hazards and prevention since 1985. His research interests cover landslide prevention for failure mechanism and dynamics. He is now hosting a project on the mechanism and risk mitigation on landslides in Qinghai-Tibet Plateau due to earthquake. He has published more than 200 academic papers and is listed as one Highly Cited Chinese Researchers by Elsevier for years that his researches involved in Geo-risk mitigation at City and Mega Reservoir, etc.